

# U. S. Army Communications- Electronics Command

## Night Vision & Electronic Sensors Directorate

**Title:** FERROELECTRIC MATERIALS FOR APPLICATIONS IN  
SENSOR PROTECTION

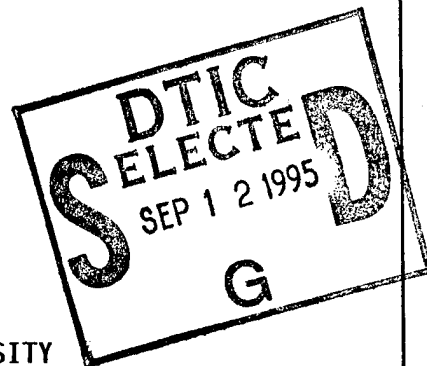
**Author(s):** AMAR S. BHALLA  
L. ERIC CROSS

**Address:** MATERIALS RESEARCH LABORATORY  
THE PENNSYLVANIA STATE UNIVERSITY  
UNIVERSITY PARK, PA 16802

**Type of Report (Final, Interim, etc.):**

FINAL REPORT

**Date:** SEPTEMBER 16, 1991 - OCTOBER 31, 1994



### Contract Number

DAAB07-91-C-K764

### Report Number

NV-95-C02

#### DISTRIBUTION STATEMENT A

Approved for public release;  
Distribution Unlimited



Fort Belvoir, Virginia 22060-5806

19950911 046

DTIC QUALITY INSPECTED 5

# U. S. Army Communications- Electronics Command

## Night Vision & Electronic Sensors Directorate

**Title:** FERROELECTRIC MATERIALS FOR APPLICATIONS IN  
SENSOR PROTECTION

**Author(s):** AMAR S. BHALLA  
L. ERIC CROSS

**Address:** MATERIALS RESEARCH LABORATORY  
THE PENNSYLVANIA STATE UNIVERSITY  
UNIVERSITY PARK, PA 16802

**Type of Report (Final, Interim, etc.):**

FINAL REPORT

**Date:** SEPTEMBER 16, 1991 - OCTOBER 31, 1994

### Contract Number

DAAB07-91-C-K764

### Report Number

NV-95-C02



#### DISTRIBUTION STATEMENT A

Approved for public release;  
Distribution Unlimited

Fort Belvoir, Virginia 22060-5806

## REPORT DOCUMENTATION PAGE

Form Approved  
OMB No. 0704-0188

1a. REPORT SECURITY CLASSIFICATION Unclassified			1b. RESTRICTIVE MARKINGS NONE		
2a. SECURITY CLASSIFICATION AUTHORITY N/A			3. DISTRIBUTION / AVAILABILITY OF REPORT APPROVED FOR PUBLIC RELEASE DISTRIBUTION UNLIMITED		
2b. DECLASSIFICATION / DOWNGRADING SCHEDULE N/A					
4. PERFORMING ORGANIZATION REPORT NUMBER(S)			5. MONITORING ORGANIZATION REPORT NUMBER(S) NV-95-C02		
6a. NAME OF PERFORMING ORGANIZATION The Pennsylvania State University		6b. OFFICE SYMBOL (If applicable)	7a. NAME OF MONITORING ORGANIZATION US ARMY CECOM NVESD		
6c. ADDRESS (City, State, and ZIP Code) University Park, PA 16802			7b. ADDRESS (City, State, and ZIP Code) AMSEL-RD-NU-LPD 10221 Burbeck Road, Suite 430 Ft. Belvoir, VA 22060-5806		
8a. NAME OF FUNDING / SPONSORING ORGANIZATION ARPA		8b. OFFICE SYMBOL (If applicable)	9. PROCUREMENT INSTRUMENT IDENTIFICATION NUMBER DAAB07-91-C-K764		
8c. ADDRESS (City, State, and ZIP Code) 3701 N. Fairfax Dr. Arlington, VA 22203-1714			10. SOURCE OF FUNDING NUMBERS		
			PROGRAM ELEMENT NO.	PROJECT NO.	TASK NO.
11. TITLE (Include Security Classification) FERROELECTRIC MATERIALS FOR APPLICATIONS IN SENSOR PROTECTION					
12. PERSONAL AUTHOR(S) AMAR S. BHALLA, L. ERIC CROSS					
13a. TYPE OF REPORT FINAL REPORT		13b. TIME COVERED FROM 9/16/91 TO 10/31/94		14. DATE OF REPORT (Year, Month, Day) 95/08/07	
15. PAGE COUNT					
16. SUPPLEMENTARY NOTATION					
17. COSATI CODES			18. SUBJECT TERMS (Continue on reverse if necessary and identify by block number)		
FIELD	GROUP	SUB-GROUP			
19. ABSTRACT (Continue on reverse if necessary and identify by block number) The focus of this program has been upon producing and characterizing new functional materials whose properties can be fine-tuned to provide eye/sensor protection against laser threats and to suit a range of optoelectronic device applications. Material systems that maximize orientational anisotropy (for use in scattering mode systems) and systems that minimize orientational anisotropy (for use in high field modulators and field induced photo-refractive applications) were both approached. Relaxor ferroelectric tungsten bronze single crystals (Sr,Ba)Nb <sub>2</sub> O <sub>6</sub> and (Pb,Ba)Nb <sub>2</sub> O <sub>6</sub> solid solution families and relaxor ferroelectric perovskite (1-x)Pb(Mg <sub>1/3</sub> Nb <sub>2/3</sub> )O <sub>3</sub> -xPbTiO <sub>3</sub> (PMN-PT) families, were studied extensively. The unique capabilities of a laser heated pedestal growth (LHPG) system were utilized for growth of new materials in single crystal fiber form that produces crystals of long interaction length for optical wave in the crystal and high crystal perfection with maximized properties along chosen directions. Hot uniaxial pressing, hot forging, or appropriate solid state reaction processing methods were used to produce transparent polycrystalline ceramics to provide low scattering high anisotropy ceramics or high scattering high anisotropy ceramics. This final report summarizes significant results produced from this program through combination of experimental and crystal chemistry approaches in this field, delineates conclusions drawn from the research, and provides recommendations for future research.					
20. DISTRIBUTION / AVAILABILITY OF ABSTRACT <input checked="" type="checkbox"/> UNCLASSIFIED/UNLIMITED <input type="checkbox"/> SAME AS RPT. <input type="checkbox"/> DTIC USERS			21. ABSTRACT SECURITY CLASSIFICATION		
22a. NAME OF RESPONSIBLE INDIVIDUAL BYONG H. AHN			22b. TELEPHONE (Include Area Code) (703) 704-2031		22c. OFFICE SYMBOL AMSEL-RD-NV-LPD

# FINAL TECHNICAL REPORT

## FERROELECTRIC MATERIALS FOR APPLICATIONS IN SENSOR PROTECTION

September 16, 1991, to October 31, 1994

### Night Vision and Electronic Sensors Directorate

NV-95-CO2

#### ARPA PROJECT

Order No. DAAB07-91-C-K764

Amar S. Bhalla

L. Eric Cross

Accession For	
NTIS	CRA&I <input checked="checked" type="checkbox"/>
DTIC	TAB <input type="checkbox"/>
Unannounced <input type="checkbox"/>	
Justification _____	
By _____	
Distribution /	
Availability Codes	
Dist	Avail and/or Special
A-1	

**Materials Research Laboratory**  
**The Pennsylvania State University**  
**University Park, PA 16802**

## EXECUTIVE SUMMARY

This document is a final technical report of a research program entitled "Ferroelectric Materials for Applications in Sensor Protection." This ARPA program was funded through the Center for Night Vision Labs and Electrooptics under grant No.: DAAB07-91-C-K764. The grant was for the period September 16, 1991, through October 31, 1994.

The focus of this program has been upon producing and characterizing new functional materials whose properties can be fine-tuned to provide eye/sensor protection against laser threats and to suit a range of optoelectronic device applications.

Material systems that maximize orientational anisotropy (for use in scattering mode systems) and systems that minimize orientational anisotropy (for use in high field modulators and field induced photo-refractive applications) were both approached. Relaxor ferroelectric tungsten bronze single crystals  $(\text{Sr,Ba})\text{Nb}_2\text{O}_6$  and  $(\text{Pb,Ba})\text{Nb}_2\text{O}_6$  solid solution families and relaxor ferroelectric perovskite  $(1-x)\text{Pb}(\text{Mg}_{1/3}\text{Nb}_{2/3})\text{O}_3$ - $x\text{PbTiO}_3$  (PMN-PT) families, were studied extensively.

The unique capabilities of a laser heated pedestal growth (LHPG) system were utilized for growth of new materials in single crystal fiber form that produces crystals of long interaction length for optical wave in the crystal and high crystal perfection with maximized properties along chosen directions. Hot uniaxial pressing, hot forging, or appropriate solid state reaction processing methods were used to produce transparent polycrystalline ceramics to provide low scattering high anisotropy ceramics or high scattering high anisotropy ceramics.

Transparent PMN-PT electrooptic ceramics were fabricated with good optical transmission, large electrooptic coefficients, and display the optical features characteristic of relaxor ferroelectrics.

Optical transmission of the fabricated ceramics indicates that the range of transparency extends from about  $0.38\text{ }\mu\text{m}$  increasing to near  $6\text{ }\mu\text{m}$  with gradually decreasing

transmission further into the infrared to become totally absorbing at 10  $\mu\text{m}$ . The transmission values approaching those of PLZT ceramics in the case of high purity prepared samples with low PT content. The results indicated that the morphotropic phase boundary rhombohedral compositions are more difficult to be optically transparent. For the 632.8 nm wavelength used for many optical measurements, the transmission values for PMN-PT ceramics can achieve 60% transmission without antireflection coatings.

It has been shown that PMN-PT ferroelectric may be well suited to serve as EO polarization modulators and optical switching applications because of many desirable qualities.

SBN single crystals approximately 400-600  $\mu\text{m}$  in diameter and 30-40 mm in length, of compositions extending across the solid solution range,  $0.25 < x < 0.75$ , were grown by laser heated pedestal growth (LHPG) technique. High quality single crystal fibers with compositional homogeneity and relatively dislocation-free were produced at growth rates up to 40 mm/h.

The optical properties (transverse effective electrooptic,  $r_e$ , halfwave voltage,  $V_\pi$ , and temperature dependence of the birefringence,  $\Delta n_o(T)$ , etc.) of SBN single crystals grown by the LHPG technique were investigated and compared to crystals grown by the Czochralski technique.

Additional study on the low temperature dielectric dispersion behavior revealed further the correlation of the deformed oxygen octahedral structure characteristic in tungsten bronze family and their dielectric and electrooptic properties.

Feasibility of potential application of photorefractive fibers in optical memory, interconnection, and other applications was demonstrated through this project.

This final report summarizes significant results produced from this program through combination of our experimental and crystal chemistry approaches in this field.

## TABLE OF CONTENTS

ABSTRACT .....	ii
LIST OF TABLES .....	v
LIST OF FIGURES .....	v
LIST OF APPENDICES .....	v
1. INTRODUCTION .....	1
2. TOPICS OF STUDY .....	5
3. MATERIAL CONSIDERATIONS FOR SENSOR PROTECTION .....	5
3.1 SINGLE CRYSTALS OF HIGH PHOTOREFRACTIVE EFFECTS.....	6
3.2 FIELD INDUCED PHOTOREFRACTIVE EFFECTS.....	7
3.3 DOPANTS.....	10
4. TRANSPARENT CERAMICS.....	10
4.1 BACKGROUND.....	10
4.2 PREPARATION OF TRANSPARENT CERAMICS.....	12
4.3 OPTICAL TRANSPARENCY .....	12
4.4 REFRACTIVE INDICES AND DISPERSION .....	14
4.5 ELECTROOPTIC PROPERTIES.....	15
4.6 PHOTOREFRACTIVE EFFECT .....	15
4.7 SWITCHING SPEED.....	15
4.8 SUMMARY .....	17
5. SINGLE CRYSTAL FIBERS GROWN BY LHPG .....	20
5.1 SBN FAMILY SINGLE CRYSTAL GROWTH.....	21
5.2 SBN FAMILY OPTICAL AND ELECTROOPTIC PROPERTIES.....	22
6. EO PROPERTIES OF SINGLE CRYSTALS AS FUNCTION OF TEMPERATURE .....	23
6.1 DETERMINATION OF ELECTROOPTIC COEFFICIENTS $r_{13}$ AND $r_{33}$ .....	24
6.2 EXPERIMENTAL PROCEDURE.....	25
6.2.1 Modified Mach-Zehnder Interferometer Method .....	25
6.3 MAJOR RESULTS AND DISCUSSION .....	27
7. POSSIBLE FUTURE DIRECTIONS .....	29
8. REFERENCES .....	31
9. PUBLICATIONS.....	32
10. PRESENTATIONS .....	32
11. PARTICIPANTS .....	33
12. APPENDICES.....	34

## LIST OF TABLES

Table I.	Electrooptical Property of Materials: A Survey	8
Table II.	Electrooptic and Polarization Optic Coefficients of Pb Perovskite Compositions	16
Table III.	Ferroelectric and EO Properties of Selected Crystals (at 633nm and ~25°C)	29

## LIST OF FIGURES

Figure 1.	Transverse Electrooptic Switching Response for 0.93P(La)MN-0.07PT for various applied pulse widths at 632.8 nm and field of 1.5 kV/cm at T=24°C.	18
Figure 2.	Transverse Electrooptic Switching Response for 0.90PMN-0.10PT with Applied Square Wave Voltage Pulse of 2kV/cm for Widths of a)60 $\mu$ sec and b) 120 $\mu$ sec at T=24°C and 632.8 nm.	19
Figure 3.	Schematic Configuration of the Modified Mach-Zehnder Interferometer.	26

## LIST OF APPENDICES

Appendix 1.	D. A. McHenry, J.R. Giniewicz, T.R. Shrout, S.J. Jang, and A.S. Bhalla, "Electrical and Optical Properties of Relaxor Ferroelectrics," <i>Ferroelectrics</i> , <b>102</b> , 161 (1990).
Appendix 2.	J.K. Yamamoto, D. A. McHenry, and A.S. Bhalla, "Strontium Barium Niobate Single Crystal Fibers: Optical and Electro-optic Properties," <i>J.Appl. Phys.</i> <b>70</b> , 3215-3222 (1991).
Appendix 3.	J.K. Yamamoto, S.A. Markgraf, and A.S. Bhalla, " $\text{Sr}_x\text{Ba}_{1-x}\text{Nb}_2\text{O}_6$ Single Crystal Fibers: Dependence of Crystal Quality on Growth Parameters," <i>J. Cryst. Growth.</i> <b>123</b> , 423-435 (1992).
Appendix 4.	D.A. McHenry, "Optical and Electrooptical Properties of Lead Magnesium Niobate-Lead Titanate," Ph.D. Thesis, Penn State University (1992).
Appendix 5.	F.T.S. Yu, S. Yin, F. Zhao, H. Zhou, and A.S. Bhalla, "Wavelength Multiplexing Fiber Holographic Construction Using a Ce and Fe Doped PR

Fiber with a Tunable Visible Light Laser Diode," *IEEE Photonics Tech. Letters*, **5**, 1230-1233 (1993).

Appendix 6. J. M. Pova, Ruyan Guo and A.S. Bhalla, "Linear Electrooptic Coefficients Measured Utilizing Modified Mach-Zehnder Interferometer Technique," *Proceedings of Thirty-Eighth Brazilian Congress of Ceramics*, Blumenau, Brazil (June 18-21, 1994).

Appendix 7. Francis T.S. Yu, Shizhuo Yin, Jianzhong Zhang, and Ruyan Guo, "Application of Fiber Speckle Hologram to Fiber Sensing," *Applied Optics*, **33**(22) 5202-3 (1994).

Appendix 8. J.M. Pova, R. Guo, and A.S. Bhalla, "Low Temperature Dielectric Relaxation Phenomena in Relaxor Ferroelectric Strontium Barium Niobate," *Ferroelectrics* **158**, 283-288 (1994).

## 1. INTRODUCTION

This document is a final technical report of a research program entitled "Ferroelectric Materials for Applications in Sensor Protection." This ARPA program was funded through the Center for Night Vision Labs and Electrooptics under grant No.: DAAB07-91-C-K764. The grant was for the period September 16, 1991, through October 31, 1994.

The focus of this program has been upon producing and characterizing new functional materials whose properties can be fine-tuned to suit a range of optoelectronic device applications.

Materials issues on the selection considerations for optoelectronic applications are addressed from both crystal chemistry point of view and based on broad range literature surveys. Systems which maximize orientational anisotropy (for use in scattering mode systems) and systems which minimize orientational anisotropy (for use in high field modulators and field induced photo-refractive applications) were both approached. Important representative materials studied include the followings:

Relaxor ferroelectric tungsten bronze single crystals  $(\text{Sr,Ba})\text{Nb}_2\text{O}_6$  and  $(\text{Pb,Ba})\text{Nb}_2\text{O}_6$  solid solution families;

Relaxor ferroelectric perovskite  $\text{Pb}(\text{Mg}_{1/3}\text{Nb}_{2/3})\text{O}_3$  (PMN), and  $(1-x)\text{Pb}(\text{Mg}_{1/3}\text{Nb}_{2/3})\text{O}_3-x\text{PbTiO}_3$  (PMN-PT) families.

Major techniques in two different areas were used to produce the materials in this study:

(1) Unique capabilities of a laser heated pedestal growth (LHPG) system were utilized for growth of new materials in single crystal fiber form that produces crystals of long interaction length for optical wave in the crystal and high crystal perfection with maximized properties along chosen directions;

(2) Hot pressed, hot forged, or appropriate solid state reaction processing methods were used to produce transparent polycrystalline ceramics to provide

low scattering high anisotropy ceramics or high scattering high anisotropy ceramics.

To extend the family of high quality optically transparent ceramics, we studied lead based perovskites ferroelectric relaxor family. Due to the less predictable weak field electrooptic responses, our efforts were geared primarily on the high field properties, the degree of induced anisotropy (grain-to-grain) and thus the scattering, both depends markedly on the available families of domain states which can be metastably induced by the field. These high field properties are of most use in electrooptic and field induced photorefractive applications, and that are most tractable to compositional controls.

Polycrystalline specimens that are transparent enough for optical and electrooptical property measurements, have desirable characteristics including uniform grain growth, high density, and the elimination or reduction of second phases, are requirements not easily achievable by conventional sintering methods. The specimens used in this project were prepared by means of hot-uniaxial pressing with additions of excess volatile species to aid in densification and to promote transparency.

A comprehensive understanding of the optical behavior of PMN-PT was carried out during this project. Optical, electrooptical and related properties were studied to characterize and ascertain the usefulness of PMN-PT compositions for various electrooptic device applications. The motivation for selecting the particular PMN-PT system for examination is discussed in Section 3. The optical properties, thermooptic properties, and electrooptic properties, including the electrooptic switching response speed studies, are briefed in the following Section 4.

Optical and electrooptical properties of PMN-PT solid solution system in the visible region, transmission as a function of wavelength, refractive indices as a function of temperature and wavelength, and quadratic electrooptic coefficient data are reported in Appendix 1. More complete treatment of PMN-PT optical and electrooptic properties is the content of Appendix 4 (abstract of a Ph.D. thesis).

The interest in the optical properties of ferroelectric tungsten bronze family had been brought upon by the large electrooptic coefficients and low halfwave voltages, compared to that of perovskites. The linear electrooptic coefficients increase with increasing strontium concentration, in SBN solid solutions. The refractive indices,  $n_o$  and  $n_e$ , have been measured by the minimum deviation methods as a function of wavelength and temperature. The extraordinary index,  $n_e$ , was sensitive to both temperature and composition, in agreement with electrooptic results. The electrooptic coefficient,  $r_{33}$ , in a tetragonal tungsten bronze crystal is an order of magnitude larger than the transverse coefficient,  $r_{42}$ , indicating that the polar direction is the most susceptible to structural and electronic changes. Correspondingly, the transverse EO coefficient,  $r_{42}$  or  $r_{51}$ , in a tungsten bronze ferroelectric crystal of orthorhombic symmetry, is much larger than the longitudinal ones,  $r_{33}$  and  $r_{13}$ , on account of the large transverse dielectric constant and longitudinal structural susceptibility along the polar direction.

SBN single crystals approximately 400-600  $\mu\text{m}$  in diameter and 30-40 mm in length, of compositions extending across the solid solution range,  $0.25 < x < 0.75$ , were grown by laser heated pedestal growth technique. Crystal quality was evaluated through the observation of dislocation patterns produced in an acid-etch technique, and the compositional homogeneity was monitored by the change in the ferroelectric transition temperature as a function of growth rate and position along the fiber. High quality single crystal fibers were produced at growth rates up to 40 mm/h. The single crystals were compositionally homogeneous and relatively dislocation-free. The detailed account for the growth studies is provided in Appendix 3.

The optical properties of SBN single crystals grown by the LHPG technique were investigated and compared to crystals grown by the Czochralski technique. The room temperature transverse effective electrooptic,  $r_e$ , halfwave voltage,  $V_\pi$ , and temperature dependence of the birefringence,  $\Delta n_o(T)$ , were determined for SBN61 single crystal fibers produced by the laser heated pedestal growth technique. The effect of cerium doping, 0.034 atm %, had on the measured properties was also reported. Concurrent measurements on a Czochralski grown SBN61 single crystal enabled comparison of

the single crystal fibers to bulk-grown single crystal. Property studies of the single crystal fiber SBN61 are presented in Appendix 2.

Low temperature dielectric relaxation phenomena in SBN was studied to understand the relaxor behavior of the tungsten bronze ferroelectric oxide family and to gain the understandings of the origin of the extraordinarily large electrooptic coefficient often found in the tungsten bronze families. Earlier studies<sup>1</sup> showed that the dielectric and pyroelectric properties of SBN family are sensitive to the degree of cation ordering within the oxygen octahedra framework, induced by quenching and annealing treatments. The detailed study on the low temperature dielectric dispersion behavior revealed further the correlation of the deformed oxygen octahedral structure characteristic in tungsten bronze family and their dielectric properties. This work is described in Appendix 8.

Temperature dependence of the electrooptic coefficients is one of the major concern for practical device applications. The determination of the individual  $r_{33}$  and  $r_{13}$ , as function of temperature, is also important in designing the working modes of the devices. Traditional electrooptic measurements (EO Sernamont measurement scheme) for determining halfwave voltage, can not separate the  $r_{13}$  and  $r_{33}$ , therefore can not access the individual effect of refractive indices as function of applied field. In this project, a modified Mach-Zehnder interferometer measurement system was assembled to measure the  $r_{13}$ , and  $r_{33}$ , and their temperature dependence. This interferometric technique not only exposes sample to a minimum driven electric field ( $V_{app} \ll V_{\pi}$ ), but also provides very high sensitivity. Measurement procedure and measurement results of the SBN and PBN samples are discussed in Section 5 (also in Appendix 6).

Through collaboration with Prof. Francis T.S. Yu and his group at Electrical Engineering, Penn State, a sensitive fiber-speckle field sensor using a Ce/Fe doped  $\text{LiNbO}_3$  photorefractive fiber (grown by the LHPG technique) hologram was demonstrated. The sensitivity of this photorefractive fiber specklegram sensor can be of the order of  $0.05 \mu\text{m}$ . The demonstration system suggested the potential widespread use of practical fiber-sensing applications. This work is described in Appendix 7. A

wavelength-multiplexed reflection-type photorefractive fiber hologram using a tunable visible-light laser diode was also shown to offer a higher and more uniform wavelength selectivity than that of the transmission-type. This work further showed feasibility of potential application of photorefractive fibers in optical memory, interconnection, and other applications (Appendix 5).

## **2. TOPICS OF STUDY**

The main tasks to be accomplished on this contract fall into two major areas of research:

- (1) Using ferroelectric crystalline systems whose properties have already been fine tuned for electrooptic and photorefractive laser protection application to grow suitably oriented high quality single crystal fibers which will duplicate the desirable behavior but permit devices with much longer interaction length. The approach uses the laser heated pedestal growth method for generating fibers using appropriate choice of seed crystal and growth conditions to control orientation and crystal quality.
- (2) To use uniaxial hot pressing (HUP) and appropriate powder preparation techniques to produce transparent polycrystalline ceramics of quality suitable for electrooptic and photo refractive applications.

The focus of this program has been upon producing and characterizing new functional materials whose properties can be fine-tuned to suit a range of optoelectronic device applications.

## **3. MATERIAL CONSIDERATIONS FOR SENSOR PROTECTION**

In principle, any electrooptic material in which light can produce free charge carriers may be photorefractive. In practice, only the materials which have large electrooptic coefficients lead to the large nonlinear effects, large charge carrier mobilities and moderate dielectric constants that guide to the good sensitivity. A figure-of-merit for photorefractive material is often defined as

$$Q = \frac{n^3 r}{\epsilon}$$

where  $n$  is the index of optical refraction,  $r$  the relevant electrooptic coefficient, and  $\epsilon$  the dielectric constant.

Depending on the different applications and mode of operation, photorefractive sensitivity that is defined as the index change per absorbed energy per unit volume:

$$S = \frac{\Delta n}{\alpha I_0 t}$$

where  $\alpha$  is photorefractive absorption coefficient,  $I_0$  the intensity of light, and  $t$  the minimum time needed for the formation of an index grating, is also another useful figure-of-merit.

A literature survey on various ferroelectric materials and their electrooptic properties reported is summarized in Table I. As can be seen, high electrooptic coefficients are often found in ferroelectric lead-containing oxide perovskites and in crystals of ferroelectric tungsten bronze oxide families.

### 3.1 SINGLE CRYSTALS OF HIGH PHOTOREFRACTIVE EFFECTS

For high longitudinal photorefractive effects several crystal systems are of interest. In the perovskite family  $\text{BaTiO}_3$  grown in the cubic form, then polarized into the stable single domain tetragonal form, offers exceedingly high values of  $r_{51}$ .  $\text{BaTiO}_3$  therefore works more effectively in the longitudinal mode. However,  $\text{BaTiO}_3$  has a tetragonal-orthorhombic phase transition at near  $10^\circ\text{C}$  hence a severer dielectric constant and electrooptic coefficient change with temperature.

In the tungsten bronze family, joint work between PSU and Rockwell has defined two composition systems of interest. In PBN crystals on the tetragonal side but close to the morphotropic phase boundary composition have exceptionally high  $r_{51}$ . Compositions in the strontium barium niobate family have been explored and shown to offer high  $r_{33}$ , and high  $r_{51}$ , with cerium doping, so a transverse electrooptic effect can also be utilized. Single crystals of relaxor characteristics have diffuse phase transition with strong

dielectric relaxation near  $T_c$ , that provides an additional advantage of having high dielectric constant over wide temperature range.

### 3.2 FIELD INDUCED PHOTOREFRACTIVE EFFECTS

Earlier work has been almost exclusively on the PLZT family of ceramics. Excellent transparency has been achieved; however the compositions suffer from an intrinsically high concentration of defect centers associated with the replacement of three divalent lead atoms with two trivalent lanthanum atoms on the sites of the  $ABO_3$  structure.

Most of the systems that are of interest optically (for this project) are ferroelectric relaxors of lead based perovskites. The composition as a relaxor ferroelectric can be switched from pseudocubic (isotropic) to a quadratic electrooptically induced birefringent state. Extinction and speed are of concern as are limited by the secondary elastooptic effects but are adequate for the nuclear application.

#### (1) Grain oriented mode systems: Low Scattering High Anisotropy Ceramics

Design of lead based compositions, particularly the ferroelectric relaxor family compositions close to the morphotropic phase boundaries, in which large values of optical anisotropy can be induced at low fields without penal grain boundary scatter. This system is most valuable for photorefractive induced photorefractive, electrooptic modulator, and birefringence switching applications.

#### (2) High Field Modulators: High Scattering High Anisotropy Ceramics

Design of compositions with essentially completely converse properties in which induced anisotropic properties of the grains will give rise to maximum scattering. This system is used in scattering mode switches which have the strong advantage of not requiring polarized light and where switching speeds have already been demonstrated in the nanosecond regime. This type high anisotropy materials are mostly useful for field induced scattering mode shutters.

Table I. Electrooptical Property of Materials: A Survey\*

Materials	$r_{13}(\text{pm/V})$	$r_{33}(\text{pm/V})$	$r_c(\text{pm/V})$	$r_{51}(\text{pm/V})$	sym.	$T_c$ (°C)	Ref.
$\text{Ba}_2\text{Na}_{1-x}\text{K}_x\text{Nb}_5\text{O}_{15}$ $x=0\sim 0.9$			31~50 40~52				
$\text{Ba}_{2.6}\text{Na}_{2.7}\text{Y}_{0.7}\text{Nb}_{10}\text{O}_{30}$			730/n <sup>3</sup>				
$\text{Ba}_3\text{Nb}_4\text{TiO}_{15}$	42	117	370		4mm		(2)
$\text{BaTiO}_3$	19.5	80		1600		128°C	(1)
$\text{BaTiO}_3$	8~24	28~80	19~106	1280	4mm		(2)
$\text{BaTiO}_3$	8	28	108 <sup>T</sup> /23 <sup>S</sup>	1640 <sup>T</sup> /820 <sup>S</sup>		25°C	
$\text{Bi}_2\text{WO}_6$	+15/+13	+19			mm2		(2)
m-C <sub>6</sub> H <sub>4</sub> (NO <sub>2</sub> )NH <sub>2</sub>		7.69/1.01	8.67		mm2		(2)
$\text{Cd}[\text{Hg}(\text{SCN})_4]$	5.3				4-bar		(2)
$\text{CdGa}_2\text{S}_4$	0.37				4-bar		(2)
$\text{CdS}$	1.1	2.4	4~6.5		6mm		(2)
$\text{CdSe}$	1.8	4.3			6mm	633°C	(2)
$\text{Fe}_3\text{B}_7\text{O}_{13}\text{I}$	8~15/3~6	10~18			mm2		(2)
$\text{K}_3\text{Li}_2\text{Nb}_5\text{O}_{15}$	8.9	78			4mm		(2)
$\text{K}_3\text{Li}_2\text{Nb}_5\text{O}_{15}$	105/n <sup>3</sup>	790/n <sup>3</sup>					
$\text{KNbO}_3$	4.5~28/ 8~+1.3	+22~64			mm2		(2)
$\text{KNbO}_3$		67		380			(1)
$\text{KNbO}_3$	$r_a=65$ $r_b=30$	$r_c=26$			mm2		(2)
$\text{KNbO}_3$	+28	+64		105		418°C	
0.48 $\text{KNbO}_3$ -0.52 $\text{KTaO}_3$		2.8~14 (20~80°C)					
$\text{K}(\text{Nb}_{0.38}\text{Ta}_{0.62})\text{O}_3$	-100	1400			4mm	28°C	(2)
$\text{KPb}_2\text{Nb}_5\text{O}_{15}$	$r_a=53$		71		mm2		(2)
$\text{KPb}_2\text{Nb}_5\text{O}_{15}$	$r_b=53\sim 71$						
$(\text{K}_{1/2}\text{Pb}_{2/3})(\text{Zn}_{2/9}\text{Nb}_{7/9})\text{O}_3$							

$$* r_a = r_{33} - (n_z/n_y)^3 r_{23}, r_b = r_{33} - (n_x/n_z)^3 r_{13}, r_c = r_{13} - (n_z/n_y)^3 r_{23}$$

(1) Landolt Börnstein: Piezoelectric, Electrooptic and Elastooptic Index.

(2) Landolt Börnstein, New Series, Vol. III/16

(Cont.) Table I. Electrooptical Property of Materials: A Survey

Materials	$r_{13}(\text{pm/V})$	$r_{33}(\text{pm/V})$	$r_c(\text{pm/V})$	$r_{51}(\text{pm/V})$	sym.	$T_c$ (°C)	Ref.
Li(COOH)H <sub>2</sub> O	-1.0/+3.2	-2.6			mm2		(2)
LiIO <sub>3</sub>	+4.1~6.4	+6.4~4.2		+3.3	6		(2)
LiNbO <sub>3</sub>	+8.6~10.9	+30.8~32.2	+16~28		3m		(2)
LiNbO <sub>3</sub>	6.5~10.9	28~34	18	32			
LiTaO <sub>3</sub>	7~7.5	~1(±0.2)		22	3m		(2)
LiTaO <sub>3</sub>	4.5~8.4	27~30.5	22	20			
NaBa <sub>2</sub> Nb <sub>5</sub> O <sub>15</sub>	15	48	90				
NaBa <sub>2</sub> Nb <sub>5</sub> O <sub>15</sub>	6.1~15/8~13	24.3~48			mm2		(2)
NaBa <sub>2</sub> Nb <sub>5</sub> O <sub>15</sub>	$r_a=36.5$ $r_b=33.8$				mm2		(2)
Na <sub>1.35</sub> Ba <sub>2.65</sub> (Nb <sub>4.35</sub> Ti <sub>0.65</sub> )O <sub>15</sub>	26	92	5	68	4mm		(2)
Pb <sub>3</sub> MgNb <sub>2</sub> O <sub>9</sub>	$r_{33}-r_{31}=$ 0.75~1.15						
Pb <sub>3</sub> MgNb <sub>2</sub> O <sub>9</sub>	8.2	167	12~140		4mm		(2)
Pb <sub>3</sub> MgNb <sub>2</sub> O <sub>9</sub>	69/3.8				mm2		(2)
0.7 Pb <sub>3</sub> MgNb <sub>2</sub> O <sub>9</sub> -0.3PbTiO <sub>3</sub>			~400 (RT)			150 °C	
Pb(Mg <sub>1/3</sub> Ta <sub>2/3</sub> )O <sub>3</sub>	$r_{33}-r_{31}<5$						
Pb <sub>5</sub> Ge <sub>3</sub> O <sub>11</sub>	10.5~12.6	15.2~16.0	5.3	6	(296~320°C)	177 °C	(2)
PbTa <sub>2</sub> O <sub>6</sub>	small/small	7600			mm2		(2)
PbTiO <sub>3</sub>	13.8	5.9			4mm		(2)
SBN46	+35	+180			4mm		(2)
SBN60	47	470~235		42		78 °C	(1)
SBN75	67	1400-1340		42	4mm	56 °C	(1)
SBN75	66	1340		4200			
BSKNN-1		150		>200		209 °C	(1)
BSKNN-2		170		350		175 °C	(1)
BSKNN-3		200		400		180 °C	(1)
SbSI		8500			mm2	20 °C	(2)
Sr <sub>2</sub> KNb <sub>5</sub> O <sub>15</sub>			1~14 (20~160°C)				
Tourmaline	1.7	0.3			3m		(2)
ZnO	(-)1.4	2.6			6mm	633 °C	(2)
α-ZnS	(+)0.92	(-)1.85			6mm	633 °C	(2)

### 3.3 DOPANTS

The addition of dopants to the electrooptic materials served to enhance some of the optical properties. Cerium and lanthanum have been added to the congruent composition. Although cerium doping shifts the absorption edge from 0.37 to 0.50  $\mu\text{m}$ , the photorefractive sensitivity increased and the beam fanning response time decreased from the undoped composition. Lanthanum doping has been found to increase the transverse  $r_c$  coefficient and reduce the halfwave voltage of SBN50 single crystals.

## 4. TRANSPARENT CERAMICS

The objectives of our study of the PMN-PT were:

- (1) To demonstrate that as in the lead lanthanum zirconate titanate system (PLZT), PMN-PT ceramics could be processed to high optical transparency;
- (2) That the versatility of the control of the freezing temperature in the PMN-PT system by chemical manipulation would provide shutter materials with higher speed and lower halfwave voltage;
- (3) That the B-site ordering mechanism which leads to the diffuse phase transition in PMN-PT would permit optical transparency in a fully stoichiometric composition, avoiding the difficulties that plague the potential use of PLZT which by this very nature must have a high concentration of A-site vacancies in the  $\text{ABO}_3$  perovskite structure.

### 4.1 BACKGROUND

The first demonstration of transparent ceramics with useful electrooptic properties was by G. Haertling and C. Land in the lead lanthanum zirconate titanate (PLZT) family of composition.<sup>2</sup> Though it was not appreciated at the time the ability to generate highly transparent bodies dependent upon the relaxor ferroelectric characters of the PLZTs at compositions near the morphotropic phase boundary ( $x=65:35$ ). The structure of nanopolar regions in the 9:65:35 composition leaves the ceramic grain with effective

macroscopic cubic symmetry and avoids the usual grain boundary scattering in asymmetric crystal structures, but permits enhanced polarizability and consequent large electrooptic effects over a wide temperature and frequency range. The 9 mole%  $\text{La}_2\text{O}_3$  additive however coming with a necessary high concentration of lead vacancies in the A-site of the  $\text{ABO}_3$ , necessary to break up the normal polar domain structure but resulting in undesirable "side effect."

A most obvious consequence of the high defect concentration is evidenced in the weak field dielectric response where re-adjustment of the defects to the micro-polar internal structure leads to a freezing out of the mobility of the large regions and a consequent loss of low frequency polarizability.<sup>3</sup>

In optical response, the effect is manifested as an accumulation under DC bias of a slow component in the induced birefringence which lowers the high intrinsic extinction ratio. A second consequence is evidenced in the studies of the photorefractive effects in PLZTs.<sup>4</sup> The very high concentration of intrinsic defects makes it impossible to modify and control the response by the normal aliovalent doping schemes.

In the PMN-PT system there is the possibility to eliminate the defect structure. For the systems containing  $\text{Pb}(\text{Mg}_{1/3}\text{Nb}_{2/3})\text{O}_3$ , the break up of the normal ferroelectric domain structure is affected by a specially limited ordering of the Mg:Nb cations on the B-site in the lattice. Because of the large size difference Mg:Nb tend to order 1:1 on a NaCl type super-lattice, however such ordering must lead to very high local charge unbalance and high internal fields which limit the ordering. It is the self generating: self limiting nano-scale (3-5 nm) ordering which breaks up the conventional ferroelectricity but can be produced in a macroscopically fully stoichiometric structure that makes the PMN-PT system uniquely interesting. Earlier studies in MRL<sup>5</sup> have shown that any stabilization of the slower component of the polarizability in PMN can be eliminated by careful processing leading to compositions which are completely free from aging.

## 4.2 PREPARATION OF TRANSPARENT CERAMICS

The PMN-PT ceramics used in this work were prepared by the columbite precursor method<sup>6</sup> in order to avoid the deleterious effects of pyrochlore phase formation. The columbite phase,  $\text{MgNb}_2\text{O}_6$ , was formed initially from powders of the two refractory B-site oxides,  $\text{MgO}$  and  $\text{Nb}_2\text{O}_5$ , in stoichiometric ratio,



and subsequently calcined. The columbite powder then was mixed with appropriate amounts of  $\text{PbO}$ ,  $\text{TiO}_2$ , and  $\text{La}_2\text{O}_3$  to form the pure perovskite structure. Subsequent sintering was typically performed at  $1100^\circ\text{C}$  or  $1200^\circ\text{C}$  for 4-6 hours.

The ceramics were then hot pressed to near theoretical density ( $>99.6\%$ ) and x-ray powder diffraction revealed a single phase perovskite structure for all the compositions ( $x\text{PMN}-[1-x]\text{PT}$ ,  $x=0.93, 0.90, 0.80, 0.70$ , and  $0.60$ ).

Excess  $\text{PbO}$  (2 wt.%) was added to several compositions in order to compensate for losses in processing. Excess  $\text{PbO}$  and higher pressing temperatures correspond with enhanced grain growth. No variation in average grain size as determined by scanning electron microscope examination was observed as a function of position. It has been suggested<sup>7</sup> that scatter mode applications require larger grain size for memory or non-memory compositions, and electric controlled birefringence requires small grain sizes for memory compositions and large grain sizes for non-memory ones. The microstructures of the PMN-PT ceramics prepared were found to be uniform with well formed equiaxed grains with controllable sizes in the range  $2\text{-}10\text{ }\mu\text{m}$ .

## 4.3 OPTICAL TRANSPARENCY

The optical transmission was measured on thin plane-parallel cut and polished disks of hot pressed electrooptic ceramic samples of near theoretical density. No anti-reflection coatings were applied. Calibrated spectrophotometers investigated the transmission of the samples for normal incidence of light in the near ultraviolet (UV), visible and infrared spectral regions at room temperature.

The PMN-PT ceramics exhibit good optical transparency. The percentage of transmitted light begins to rise abruptly at just below 380 nm and then increases only gradually with wavelength above 450 nm. The optical transparency is greatly decreased in the higher  $\text{PbTiO}_3$  rich compositions ( $x=0.70$  and  $0.60$ ).

Optical transmission measurements demonstrated that PMN-PT ceramics can be prepared with useful levels of transparency for electrooptic ceramic applications using the hot pressing preparation methods. Transmission approaching 60% for optically transparent ceramics of PMN-PT can be made either by hot uniaxial pressing or hot isostatic pressing to near theoretical density. High optical transmission values in PMN-PT are achievable only through the use of high purity powders as starting materials and even then the fabrication of high  $\text{PbTiO}_3$  content ceramics can be difficult due to the incorporation of point defects and the formation of light scattering centers such as macro ferroelectric domains.

Electrooptic ceramics which are relaxor compositions having macroscopically cubic symmetry for the grains are more transparent than compositions which are tetragonal ( $x>0.33$ ) and it is especially difficult to achieve high transparency for rhombohedral compositions ( $0.20<x<0.35$ ). The most transparent compositions are the pseudocubic relaxor compositions ( $x<0.10$ ) and the scattering of light in the increasingly more uniaxial compositions leads to reduced transmission. The compositional range of the relaxor portion of the phase diagram with pseudocubic symmetry and associated transmission properties are much larger in PMN-PT (0-20%) than in PLZT which has only a limited relaxor composition range.

The optical bandgap of about 3.35 eV is comparable to other Pb oxygen octahedra materials and the transmission window opening at 380 nm allows P(La)MN:PT to be used for visible and IR applications.

Very few electrooptic materials for optical devices have sufficient transparency into the important IR wavelength regimes. Pb perovskite ceramics have been investigated as materials which meets the needs of such applications. Disadvantages of other presently used IR modulators such as GaAs single crystals are that they have

intrinsically lower electrooptic coefficients and cannot be optically aligned with visible light. The KDP and ADP family of materials have limited transmission at long wavelengths due to the infrared absorption as the result of O-H lattice modes.

The IR transmission range of PMN-PT ceramics exceeds those of many other IR electrooptic modulator materials and is comparable with PLZT electrooptic ceramics. No significant absorption bands are observed before 5.6  $\mu\text{m}$  and transmission decreases gradually to become total absorbing near 10  $\mu\text{m}$ .

#### 4.4 REFRACTIVE INDICES AND DISPERSION

The refractive index and its dispersion measurement showed that 0.93PMN-0.07PT has a very high refractive index ( $>2.7$  for  $\lambda < 450$  nm). The refractive index also showed dispersion in the visible region characteristic of the optical spectrum on the long wavelength side of a UV absorption peak for normal dispersion. Appendix 1 contains the measured refractive index values and dispersion curves for PMN-PT ceramics.

Comparing the end members of the PMN-PT system the materials density decreases in going from PMN (8.14 g/cm<sup>3</sup>) to PbTiO<sub>3</sub> (7.96 g/cm<sup>3</sup>), the increasing polarizability with more PbTiO<sub>3</sub> raising the refractive index, though band structural changes overrides the effect of lowered density which would tend to lower the index.

Evaluation of the refractive index as a function of frequency and temperature evidence a persistence of a non-reversible average local polarization to temperatures (with a  $T_d$  of approximately 390°C) much higher than the temperature of the dielectric maximum. The increase in the principal refractive index in the PMN-PT system by about  $2.5 \times 10^{-3}$  for each mole percent of PbTiO<sub>3</sub> added to PMN is in close accord with the increase predicted by the partial derivation of the single term Sellmeier oscillator equation. More substantial changes in the absorption spectrum during the ferroelectric phase transition would be expected for PbTiO<sub>3</sub> because of the more significant band level and polarizability shifts connected with the displacement of the Pb atoms relative to the oxygen octahedra framework as compared to the relatively small shifts of other A-site cations. The Pb 6s<sup>2</sup> electrons certainly make important contributions to oscillator

strengths. The bandgap and average interband oscillator energy  $E_c$  tends to increase with increasing principal quantum number of the B-cation, i.e., in the order Ti, Nb, Ta.

The relaxation features from the static refractive index measurement are also described in Appendix 1.

#### 4.5 ELECTROOPTIC PROPERTIES

Both the halfwave voltage measurement method and the Senarmont compensator method were used in the electrooptic property study to measure the transverse EO coefficients and the halfwave voltage. The EO coefficients were determined from the voltage needed to induce the first fully transmitting state. Table II listed the transverse  $R$  coefficients and quadratic  $g$  coefficients for Pb-perovskites measured. Full details of the EO properties of PMN-PT transparent ceramics are the content of a Ph.D. thesis (Appendix 4).

#### 4.6 PHOTOREFRACTIVE EFFECT

PMN-PT ceramics have photoferroelectric properties and show marked sensitivity to UV light near the value of their bandgap ( $\sim 3.35$  eV). Photorefractive properties were examined by studying the effect of longwave UV 365 nm radiation on the electrooptic effect in a transverse shutter configuration. Contrast ratios could be greatly modified by simultaneous UV illumination and electric field bias on the transparent PMN-PT samples. A large dynamic range and sensitivity was indicated by the sizable saturation value of the photoinduced refractive index change of  $\Delta n > 10^{-4}$  show with the modest UV source employed in this study.

Electrooptic sensitivity may be more easily controllable in PMN-PT ceramics than in PLZT, based upon the selective substitution of cations to introduce trap levels into the electronic energy bandgap with variable carrier absorption and drift lengths.

#### 4.7 SWITCHING SPEED

The measurement of the EO shutter response for PMN-PT ceramic compositions were taken as a function of applied pulse widths to determine the speed and the depth of

Table II. Electrooptic and polarization optic coefficients of Pb perovskite compositions

Composition	R Coefficient ( $10^{-16}\text{m}^2/\text{V}^2$ )	g Coefficient ( $\text{m}^4/\text{C}^2$ )
PMN <sup>†</sup>	1.35	0.015
PLMN <sup>††</sup>	0.27	0.006
.93PLMN-.07PT	2.1	0.0056
.90PMN-.10PT	14.1	0.0066
.80PMN-.20PT	20.3	0.007
.70PMN-.30PT	$r_c = 400 \text{ (pm/V)}$	0.009
PLZT(8.4/65/35)	5.1	0.011
PST(S=0.85)	3.1	--
PLZT(8/65/35) <sup>†††</sup>	38	--
PLZT(9.5/65/35) <sup>†††</sup>	1.8	--

<sup>†</sup> Bonner et al, 1967

<sup>††</sup> Kim, 1990

<sup>†††</sup> Haertling, 1987

modulation. This response to an applied voltage pulse illustrates the possibilities of 0.93PMN-0.07PT in rapid optical shuttering applications, as seen in Figure 1. The leading and falling edges of the response curve shown in comparison with the applied pulse indicate that the ceramic can respond on a time scale of about 500 to 700 nsecs. The pulsed response is also seen to be reasonably symmetric for this composition and temperature. The response also returns to the "off" state uniformly and with high optical density after a short ringdown time. The ringing in the electrooptic switching response is readily apparent and is due to the piezoelectric or electrostrictive effect which changes the optical path length in "unclamped" samples which are free to vibrate. An example of electrooptic switching response for a 0.90PMN-0.10PT ceramic sample is shown in Figure 2. The response to the applied pulse for this composition and temperature is seen to be asymmetric with a longer leading edge response and a shorter falling edge response. The time needed to reach 10% - 90% switching exceeds 150  $\mu$ sec at this temperature. The measured response for PLZT ceramics were reported to be lower, attributable to the reorientation of the electrostrictive strains. Single crystals generally show a faster response time, e.g.,  $\sim$ 90 nsec in  $(\text{Pb,Ba})\text{Nb}_2\text{O}_6$ .<sup>8</sup>

#### 4.8 SUMMARY

PMN-PT compositions were shown to be well suited to serve as EO polarization modulators and optical switching applications because of many desirable qualities summarized as follows:

- Relaxor ferroelectrics without an external applied field, are optically isotropic in the quiescent state and exhibits very large contrast ratios when placed in combination with optical polarization control devices such as crystalline polarizers;
- Relaxor PMN-PT ferroelectrical ceramics can be made with large area geometries which would allow for wide aperture and large acceptance angles;
- The optical transmission of ferroelectric PMN-PT oxides can extend throughout the entire visible and much of the IR wavelength range. Along with antireflection coatings to counter the reflection losses stemming from their high refractive indices,

Figure 1. Transverse Electrooptic Switching Response for 0.93P(La)MN-0.07PT for various applied pulse widths at 632.8 nm and field of 1.5 kV/cm at T=24°C.

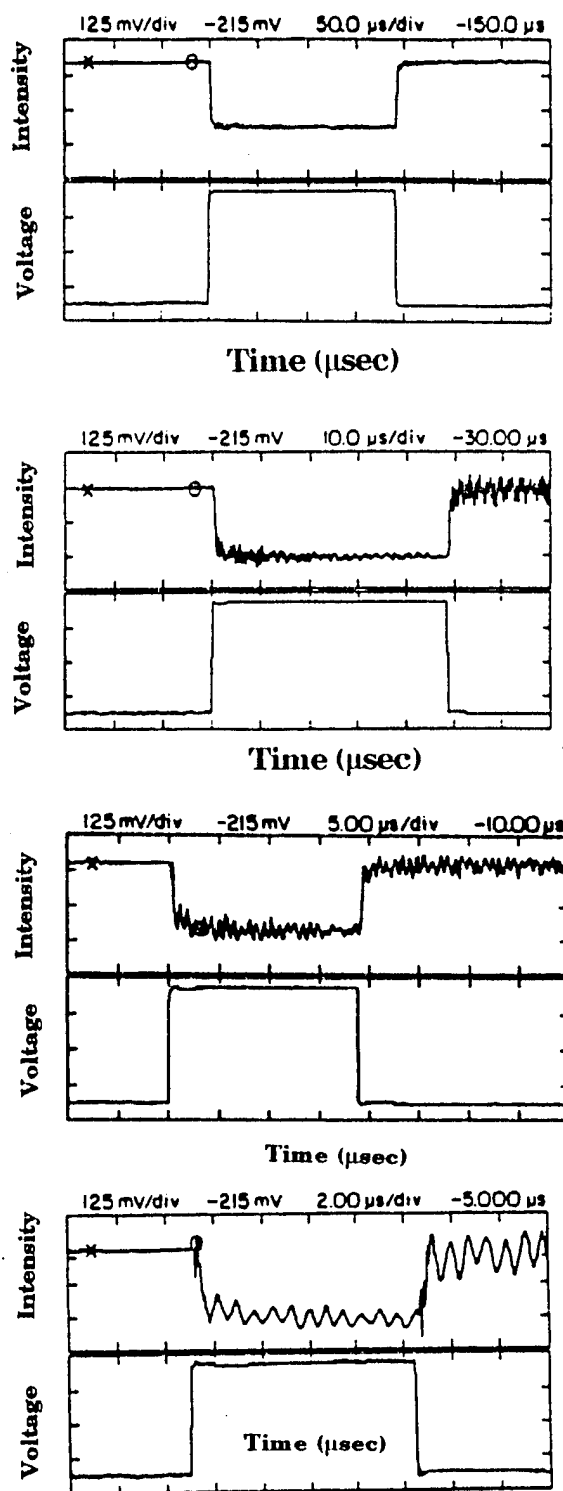
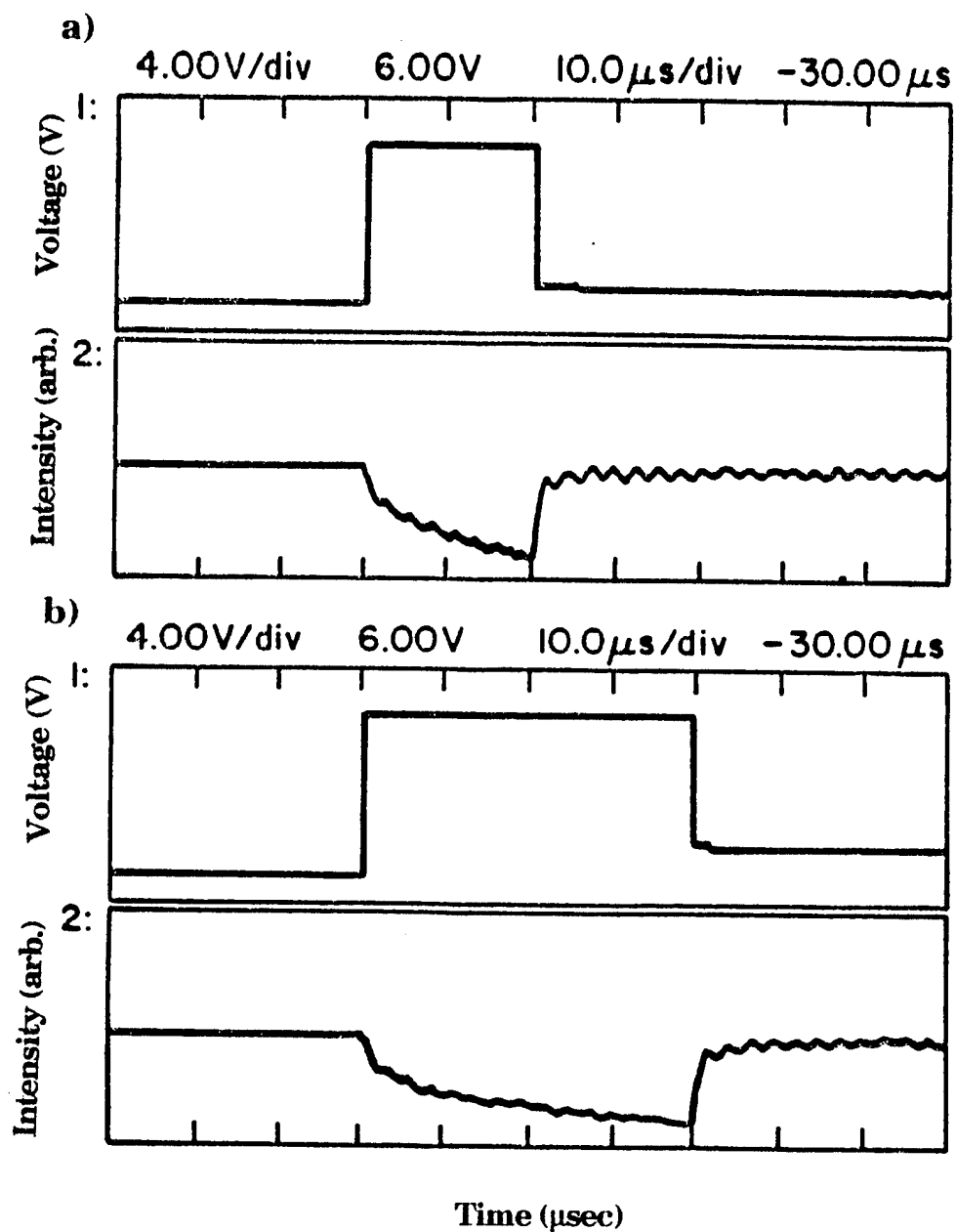


Figure 2. Transverse Electrooptic Switching Response for 0.90PMN-0.10PT with Applied Square Wave Voltage Pulse of 2kV/cm for Widths of a) 60  $\mu$ sec and b) 120  $\mu$ sec at  $T=24^\circ\text{C}$  and 632.8 nm.



- their introduction into an electrooptic modulator device system may results in acceptable low optical insertion losses;
- The application of an electric field sufficient to fully transmit the optical light beam through the modulation system may be substantially less than that required by traditional Pockels and liquid Kerr cell devices due to he large EO coefficients in materials like PMN-PT;
- The enhancement of the EO effect near the MPB was shown along with the loss of hysteresis with increasing temperature;
- The speed of EO shuttering response is rapid and thus relaxor materials would possess a large bandwidth range for optical communication and information processing. The isotropic cubic state becomes uniaxial under the action of the electric field and quickly relaxes back to its original optical isotropy without significant hysteresis even after many cycles and under large applied fields;
- PMN-PT is non-hygroscopic and is resistant to most environmental corrosives;
- The PMN-PT relaxor have extremely low thermal expansion and consequently are less sensitive to thermal fluctuations both in sample preparation and for stable optical device operation.

## 5. SINGLE CRYSTAL FIBERS GROWN BY LHPG

In this program we have focused our efforts on the tungsten bronze family as these materials in crystal form have been studied by Rockwell International Science Center and in our previous work, documented in the literature. Night Vision Labs and several other places in the US and abroad and the useful application of the SBN family -  $(\text{Sr},\text{Ba})\text{Nb}_2\text{O}_6$ , are well documented in the literature. We have also grown  $\text{LiNbO}_3$  fibers with controlled dopant of cerium (Ce) and/or iron (Fe) to study the effect of doping on the photorefractive performance, and also demonstrate the feasibilities of using crystal fibers in sensors and device applications.

The LHPG technique has several unique features that are of special importance for this program. These advantages include containerless crystal growth; capability of growing both incongruently and congruently melting compositions; ease of controlled dopants and rapid growth rates. The use of ferroelectric fiber is beneficial, not only because it avoids the difficulties of growing large, optical quality crystals, but also because many new important applications thus can be possible. A large volume of photorefractive material may be synthesized by packing an array of photorefractive fibers in a matrix fashion in many geometric configurations. Since nonlinear effects are intensity dependent, improved response may be achieved because of the longer interaction lengths than are possible with unconfined waves. Waveguides permit high energy densities by channeling radiation over much longer distances than are possible with free-space propagation of small beams.

For the fiber crystals we have undertaken the following studies:

- Evaluation of optical quality
- Estimation of the dislocation density in the fibers
- Growth striations in the fibers
- Electrooptic coefficients (also see following Section 5)
- Electrooptic coefficient as function of temperature (also see following Section 5)

All these factors are linked with the final performance of the device made out of these fibers and thus the studies have a significant importance for this project.

### **5.1 SBN FAMILY SINGLE CRYSTAL GROWTH**

The growth of single crystal fibers of the incongruently melting  $\text{Sr}_x\text{Ba}_{1-x}\text{Nb}_2\text{O}_6$  solid solution system was achieved for compositions across the solid solution range. Clear transparent crystals from starting composition of  $x=0.25, 0.40, 0.50, 0.61, 0.75$  and cerium doped SBN61 were successfully grown.

The growth of SBN61:Ce single crystal fibers under stable conditions resulted in long, uniform diameter, single crystal fibers. At a growth rate of about 40mm/h, stable growth

conditions were established after ~10 mm of growth, as determined by the rapid decrease in the dislocation density with increasing crystal length. Although the interior crystal quality was high, the outer surface of the single crystal fibers was found to contain many dislocation. Growth from single crystal feedrods produced crystals with far fewer dislocations than crystals grown from ceramic feedrods. The SBN61:Ce single crystal fibers did not grow in a single domain state.

Varying the growth rate under stable zone conditions did not affect the composition along the length of the SBN61:Ce crystal, nor did it affect the dislocation density or distribution within the fiber. Only under highly unstable growth conditions were compositional striations and large dislocation etch pits observed.

Full account of the growth study on the tungsten bronze SBN solid solution families is described in Appendix 3.

## 5.2 SBN FAMILY OPTICAL AND ELECTROOPTIC PROPERTIES

The undoped and cerium-doped SBN61 single crystal fibers grown by LHPG technique were studied for their optical and electrooptic properties. The effective electrooptic coefficient,  $r_c$ , halfwave voltage,  $V_\pi$ , and temperature dependence of the birefringence were examined in both as-grown and annealed single crystal fibers. The effects of the rapid growth rate and induced cation disorder on the optical properties were studied and the results were compared to Czochralski-grown crystals of comparable composition.

The  $r_c$  coefficients of the undoped SBN61 Czochralski grown crystal and single crystal fiber showed good agreement with each other, indicating that the linear electrooptic coefficients were not affected by the rapid growth rates found in the LHPG technique.

The addition of cerium reduced the  $r_c$  coefficients and increased the halfwave voltages relative to the undoped crystals. This is in agreement with the decrease in the dielectric constant observed in cerium-doped single crystals. There was no change in the  $r_c$  coefficients after annealing.

Frequency dispersion in the  $r_c$  coefficients and halfwave voltages of the as grown single crystal fiber was most likely caused by strain and cation disorder induced by the rapid growth rates. Post growth annealing eliminated the frequency dispersion and indicated that annealing is a necessary step to stabilize the crystal before application of these single crystal fibers in an electronic or optical device.

The quadratic  $g$  coefficients were calculated using the measured halfwave voltages, dielectric constant, and polarization. The  $g$  coefficient of the undoped SBN61 single crystal fiber was in better agreement with the literature value than the cerium doped SBN61 single crystal fiber.

The dependence of the birefringence with temperature of the single crystal fiber was found to agree with the literature. The as grown cerium doped single crystal fiber exhibited thermal hysteresis which was eliminated upon annealing. The response of the annealed single crystal fiber to an applied voltage displayed ringing at the voltage onset and decayed after 8  $\mu$ s.

Additional details on the optical and electrooptical properties of SBN single crystals are to be found in Appendix 2.

## 6. EO PROPERTIES OF SINGLE CRYSTALS AS FUNCTION OF TEMPERATURE

Lead barium niobate,  $\text{Pb}_x\text{Ba}_{1-x}\text{Nb}_2\text{O}_6$  (PBN), and Ce-doped strontium barium niobate,  $\text{Sr}_x\text{Ba}_{1-x}\text{Nb}_2\text{O}_6$  (Ce:SBN), in ferroelectric tungsten bronze family have drawn great interests because of their large electrooptic coefficients and promising applications in various optical and electrooptic devices. Linear electrooptic coefficients of PBN ( $x=0.50, 0.57$ ) and Ce:SBN ( $x=0.61$ , doped with 0.01mol% cerium) as functions of temperature have been measured using both the Senarmont compensator method and the modified Mach-Zehnder interferometer method. For Ce:SBN single crystals, the electric poling conditions are found critical in obtaining reproducible electrooptic measurement results. Piezoelectric effect makes recognizable contribution to the linear EO coefficient ( $r_{13}$ ) in the case of Ce:SBN. For PBN solid solutions, EO

excellent temperature independence over broad temperature range that makes it suitable for various EO device applications.

Contrary to earlier report,<sup>9</sup> we found the  $d_{31}$  piezoelectric constant of the Ce:SBN sample is negative.

### 6.1 DETERMINATION OF ELECTROOPTIC COEFFICIENTS $r_{13}$ AND $r_{33}$

The out put intensity of combined signal:

$$\frac{I_o}{I_i} = \sin^2\left(\frac{\Gamma}{2}\right) = \sin^2\left(\frac{\pi V}{2V_\pi}\right)$$

For  $V \ll V_\pi$  and  $\Gamma \sim \pi/2$ :  $\frac{I}{I_0} \approx \frac{1}{2} - \frac{\pi}{4} + \frac{\Gamma}{2}$

which indicates that the transmitted intensity is linearly related to the applied voltage as shown in the following figure. Where:

$\ell$ : Crystal dimension along wave propagation

$t$ : Crystal thickness in E-field direction

$\ell_0$ : Crystal dimension  $\ell$  at  $E=0$

$L$ : Light path inside the crystal

$\Gamma$ : Phase retardation

$V_{\pi-\pi}$ : Peak-to-peak value of the modulator

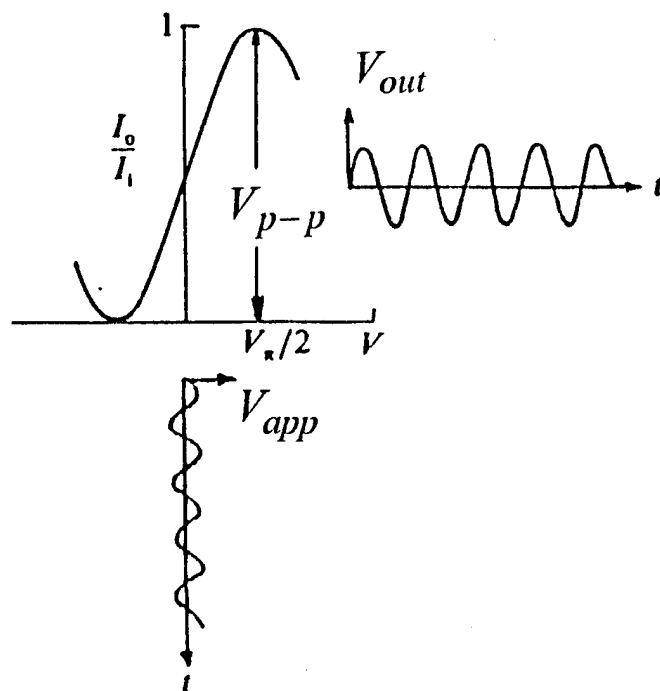
$V_{app}$ : rms value of applied AC signal

$V_{out}$ : rms value of output intensity

$$\Gamma = \frac{2\pi(\delta L)}{\lambda} = \frac{\pi V_{app}}{V_\pi}$$

$$\delta L = \Delta n \cdot \ell_0 + n \cdot \Delta \ell = \frac{\lambda}{\pi} \frac{V_{out}}{V_{p-p}}$$

$$\Delta \ell = \frac{\ell_0}{t} d_{31} V_{app}$$



$$r_{13} = -\frac{2}{n_1^3} \left( \frac{\delta L}{l_0} \frac{t}{V_{app}} - n_1 d_{31} \right) \text{ and}$$

$$r_{33} = -\frac{2}{n_3^3} \left( \frac{\delta L}{l_0} \frac{t}{V_{app}} - n_3 d_{31} \right)$$

effective  $r_c = r_{33} - \left( \frac{n_1}{n_3} \right)^3 r_{13}$  and reduced half wave voltage  $V_\pi^* = \frac{\lambda}{n^3 r_c}$ .

## 6.2 EXPERIMENTAL PROCEDURE

Single crystal specimens used for this investigation were grown by the Czochralski pulling technique. All samples were poled by applying a suitable DC field and slow cooled with the field to ambient temperature prior to the measurement, to ensure that the crystal will have large enough monodomain regions so that the entire cross-section of the light beam probes the same orientation state throughout its traversal through the crystal.

### 6.2.1 Modified Mach-Zehnder Interferometer Method

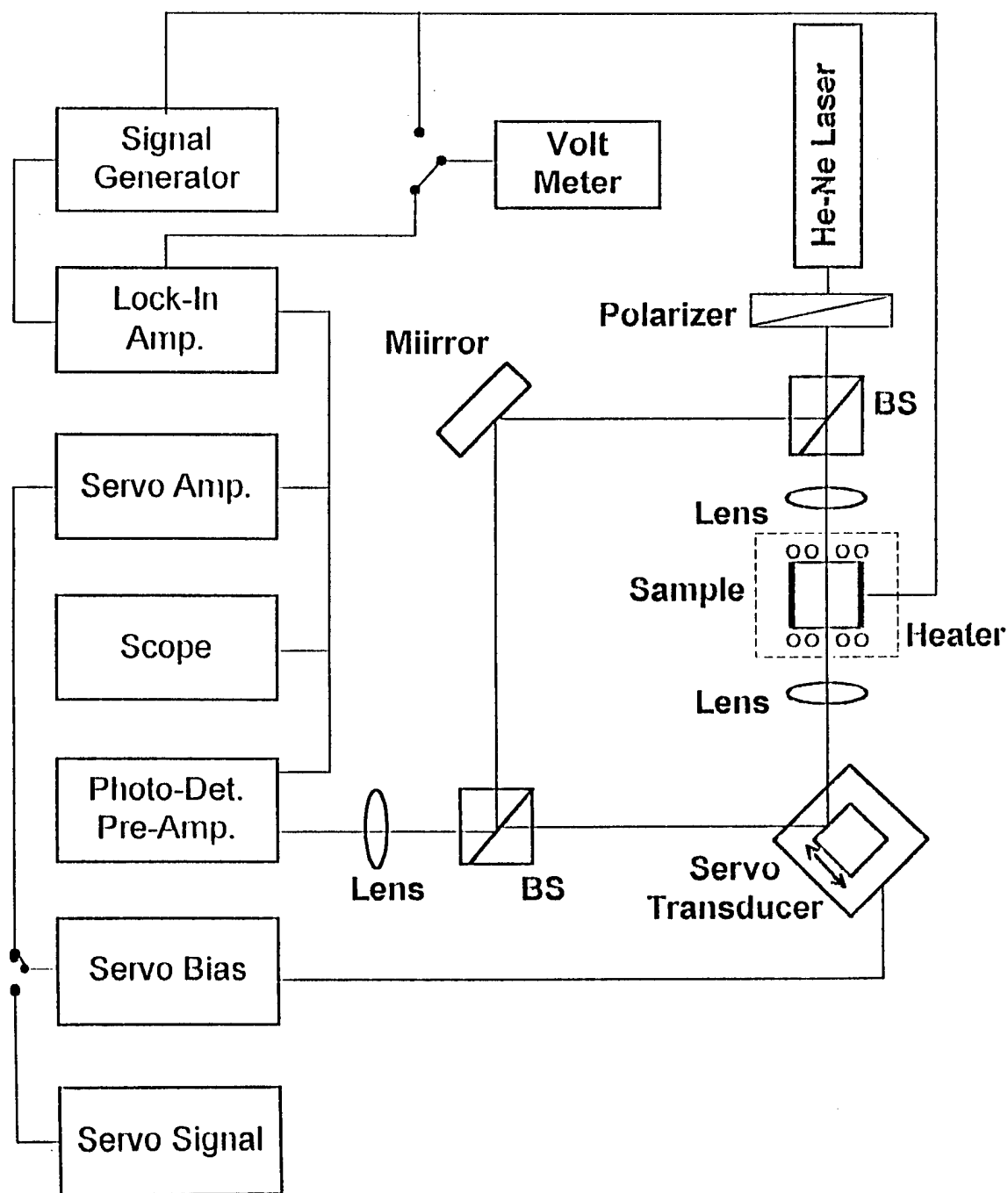
A modified Mach-Zehnder interferometer was used to measure electrooptic coefficients and field induced optical path length changes. The schematic configuration of the modified Mach-Zehnder interferometer is shown in Figure 3. This interferometer incorporates, as part of a servo-system, a piezoelectrically driven PZT stack mounted mirror that is capable of applying a known optical phase offset and a periodic modulation about these offset point. An electric field applied on the sample in one arm of the interferometer induces a phase shift and consequently changes of the intensity pattern.

Advantages of Mach-Zehnder Interferometer Method include:

#### (1) High Sensitivity

The interferometric method can be substantially more sensitive than the traditional polarimetric or photometric modulation techniques because phase shifts caused by

Figure 3. Schematic Configuration of the Modified Mach-Zehnder Interferometer.



optical path length changes of only a small fraction of a wavelength ( $<1/100$ ) are easily detectable. Optical path length changes of this magnitude for typical sample sizes correspond to birefringence changes of order  $\Delta n=10^{-6}$ ; and

## (2) Determination of Individual Transverse EO Components

The contribution of the individual EO coefficients in oxygen octahedra perovskite materials may be obtained. Changes of the refractive index along the principal axis of the optical indicatrix due to the electrooptic or elastooptic effect can be unambiguously attributed to individual tensor components and determined independently along with their signs.

A modified Mach-Zehnder interferometer method<sup>10</sup> was used to measure the electrooptic  $r_{33}$  and  $r_{13}$  coefficients and their temperature dependence. The transverse linear electrooptic coefficients, the half wave voltages and their temperature dependence were measured by using a Senarmont compensator method employing lock-in phase detection techniques. A He-Ne laser beam (10mW, 633nm) was used as a monochromatic light source. All the measurements were carried out in samples optically biased at mid-transmittance condition. Measurement signal frequency used was 1kHz, that is far from any piezoelectric resonances. Piezoelectric coefficients as function of temperature were measured by piezoelectric resonance technique.

Sample	Composition	Symmetry	$l$ (mm)	$t$ (mm)
PBN50	$\text{Pb}_{0.50}\text{Ba}_{0.50}\text{Nb}_2\text{O}_6$	Tetra., $T_c=420^\circ\text{C}$	2.101	0.570
PBN57	$\text{Pb}_{0.57}\text{Ba}_{0.43}\text{Nb}_2\text{O}_6$	Tetra., $T_c=316^\circ\text{C}$	1.061	0.894
Ce:SBN	$\text{Sr}_{0.61}\text{Ba}_{0.39}\text{Nb}_2\text{O}_6:0.01\text{mol}\%\text{Ce}$	Tetra., $T_c=78^\circ\text{C}$	0.78	1.372

## 6.3 MAJOR RESULTS AND DISCUSSION

The application of an electric field causes the optical phase to change by the following mechanisms: (1) the true EO effect changes the optical path by changing the refractive indices of crystals; (2) sample dimension change along the path of the optical beam

(caused by piezoelectric or electrostrictive effect). The piezoelectric contribution to the induced phase retardation can be significant in samples with high piezoelectric  $d_{31}$  coefficients at the measurement temperature. In Ce:SBN, the piezoelectric contribution to the  $r_{13}$  counts for ~20% of the total effect.

The  $r$  coefficients in Ce-doped SBN are comparable with the undoped SBN while the enhancement of the photorefractive properties in cerium-doped SBN61 has been reported. However, the halfwave voltage is higher than the undoped SBN, and systematical investigation on the doping effects of cerium is still lacking.

Polarization completeness has substantial influence on the electrooptic coefficients. Moderately poled samples usually yield only half the value optimized and inconsistency is often found in repeated measurements. Poling study in SBN single crystal samples showed a critical poling temperature above which the depoling process is considerably depressed. Reproducible measurement results were obtained in repeated measurements with temperature spans higher than  $T_c$ .

In contrast to the earlier report that the  $d_{31}$  is positive in SBN (Ducharme *et al.* 1987), we find  $d_{31}$  is negative using piezoelectric resonance technique. Electric field applied in the same direction to the polarization direction (opposite to the poling field direction) causes the crystal to contract in the perpendicular direction. We also found both  $r_{33}$  and  $r_{13}$  are negative in SBN and PBN crystals. Electric field applied in the optical axis direction increased the birefringence (and therefore the phase retardation). The total resulted  $r$  is combination of the EO and piezoelectric terms.

The  $r_{13}$  and  $r_{33}$  coefficients of PBN57 are higher than that of BaTiO<sub>3</sub>. Moreover, in PBN crystals, there is no ferroelectric phase transition near room temperature while BaTiO<sub>3</sub> has a tetragonal-orthorhombic phase transition near 10°C that causes a severe dielectric constant and electrooptic coefficient change with temperature. Though the  $r_{13}$  and  $r_{33}$  coefficients are comparatively smaller in PBN single crystals of tetragonal symmetry than that of Ce:SBN, the  $r$  coefficients are nearly constant over broad temperature range.

A summary and comparison of the EO properties of selected crystals is given in the Table III.

Table III. Ferroelectric and EO Properties of Selected Crystals (at 633nm and ~25°C)

Crystal	T <sub>c</sub> (°C)	Dielectric Constant		EO Coefficient (pm/V)		r <sub>c</sub> (pm/V)		Vπ* (V)	d <sub>31</sub> (pC/N)
		κ <sub>1</sub>	κ <sub>3</sub>	r <sub>13</sub>	r <sub>33</sub>	measured	calculated		
SBN61	78 <sup>a</sup>	450	900	47 <sup>#</sup>	235 <sup>#</sup>	304 <sup>@</sup>	204 <sup>#</sup>	170 <sup>%</sup>	24.6 <sup>#</sup>
BaTiO <sub>3</sub>	128	4100	150	19 <sup>#</sup>	97 <sup>#</sup>	79 <sup>#</sup>	76 <sup>#</sup>		28.7 <sup>#</sup> , -33.3
LiNbO <sub>3</sub>	1483	85.2	28.7	10.1	28.8	(+)16~28	17.7		-0.85
SBN61:Ce	78	460	1030	-52	-271	-	-224	240	-29
PBN50	420	1200	~150	-19	-57	-35.0,-40.3	-36	1330	-10
PBN57	316	1800	200	-32	-154	-162	-136	370	-10

<sup>a</sup> Neugaonkar et al. *Optical Engineering*, **26**(5), 392 (1987).

<sup>#</sup> Values are for λ=514.5nm by Ducharme et al. *IEEE J. Quantum Electronics*, **QE-23**, No 12, 2116 (1987).

<sup>@</sup> Yamamoto, *Ph.D. Thesis*, Penn State University (1990).

<sup>+</sup> Huibregtse et al. *J. Appl. Phys.* **30**, 899 (1959).

<sup>%</sup> Burns and Dacol, *Physical Review*, **B30**, 4012 (1984).

## 7. POSSIBLE FUTURE DIRECTIONS

### (1) Transparent ceramics in the PMN-PT family

It is clear from the work which has been done that the PMN-PT family of transparent ceramics has many advantages over the conventional PLZT compositions. However, it appears probable that the electrooptic or phase switching scattering mode structure could only provide a back up rather than a primary protection for exceedingly short pulse laser threats.

Works which need to be done includes:

- Full characterization of the switching speed for birefringence mode compositions
- Hot pressing of the higher PbTiO<sub>3</sub> compositions which could provide scattering mode protections.
- Detailed analysis of the phase switching under high field for the nano-polar to ferroelectric phase transition.

Unfortunately we did not have time or resource on the program to explore the photorefractive effects of these PMN-PT electrooptic ceramics. If the strong effects in the PLZT are preserved, the stoichiometric nature of the PMN-PT compositions should eliminate the troublesome intrinsic defects which Micheron<sup>4</sup> found so frustrating in his work so that doping control of the induced impurity levels in the band gap should become possible. The PMN-PT are in the same structure family as BaTiO<sub>3</sub> which is an excellent photorefractor, but hot pressing or hot forging is a much cheaper method to fabricate the long interaction length which the photorefractive systems require. Again however as with all photorefractive systems one would have to ask whether the speed can be brought to the level required for the very short pulse threats.

Work which could be proposed would include:

- Exploration of the transmission spectra of PMN-PT transparent ceramics fabricated from very high purity starting materials/
- Examination of the influence of suitable doping (ones such as Fe, Ce, Mn, Cr etc.)
- Detailed evaluation of the photorefractive effects in both lightly insulating and in very mildly reduced materials: the objective would be to demonstrate speed, sensitivity and versatility comparable to the BaTiO<sub>3</sub> and tungsten bronze single crystal compositions.

An advantage of the more comprehensive evaluation of the photorefractive possibility in the PMN-PT is that for high density optical storage these compositions can be more easily tailored than the bronzes to have low switch-over fields into the ferroelectric states and thus the strong possibility for domain stabilization of the hologram for long term or even archival storage.

## (2) Fiber systems using laser heated pedestal growth

Future work using the LHPG technique could include:

- The effect the surface layer has on the physical properties of single crystal fibers. The small geometry of the single crystal fibers provides a large surface area to volume ratio to enhance the effect.

- Incorporation of the single crystal fibers into pyroelectric or electrooptic devices, by using an individual fiber or assembling a composite of many fibers bundled together.
- Controlled environmental modifications of the growth chamber for added capability of growing volatile compounds such  $(\text{Pb},\text{Ba})\text{Nb}_2\text{O}_6$  compositions, particularly the compositions near the morphotropic phase boundary to obtain both high  $r_{33}$  and  $r_{51}$  values.
- Further investigation of doping mechanisms and effects in photorefractive fibers.
- Annealing studies to take out the strain occurred with the very high growth rates during the LHPG growth.
- Growing mixed tungsten bronze compositions which are difficult to grow in bulk crystal forms.

## 8. REFERENCES

- <sup>1</sup> R. Guo, A. Bhalla, G. Burns, and F.H. Dacol. "Studies on Annealing and Quenching of Strontium Barium Niobate (SBN) Single Crystals: A-Site Cation Ordering-Disordering Effect," *Ferroelectrics*, **93**, 1193-1204 (1989).
- <sup>2</sup> G. Haertling and C. Land, *J. Am. Ceram. Soc.*, **54**, 1 (1971).
- <sup>3</sup> J. Biggers and W. Schulze, *Am. Ceram. Soc. Bull.*, **53**, 809 (1974).
- <sup>4</sup> F. Micheron, C. Mayeux, A. Hermasin, and J. Nicolas, *J. Am. Ceram. Soc.*, **57**, 306 (1974).
- <sup>5</sup> Wuyi Pan, "Ferroelectric Type Materials for Actuator Applications," *Ph.D. Thesis, Penn State University* (1988).
- <sup>6</sup> S. L. Swartz and T. R. Shrout, *Mat. Res. Bull.*, **17**, 1245 (1982).
- <sup>7</sup> R. W. Whatmore, private communication (1991).
- <sup>8</sup> R. Guo, "Ferroelectric Properties of Lead Barium Niobate Compositions near the Morphotropic Phase Boundary," *Ph.D. Thesis, Penn State University* (1990).
- <sup>9</sup> Ducharme et al. *IEEE J. Quantum Electronics*, **QE-23**, 2116 (1987).
- <sup>10</sup> similar in design as described by W.Y. Pan and S.J. Jang, *Rev. Sci. Instrum.* **61**(8), 2109 (1990).

## 9. PUBLICATIONS

- (1) D. A. McHenry, J.R. Giniewicz, T.R. Shrout, S.J. Jang, and A.S. Bhalla, "Electrical and Optical Properties of Relaxor Ferroelectrics," *Ferroelectrics*, **102**, 161 (1990).
- (2) J.K. Yamamoto, D.A. McHenry, and A.S. Bhalla, "Strontium Barium Niobate Single Crystal Fibers: Optical and Electro-optic Properties," *J. Appl. Phys.* **70**, 3215-3222 (1991).
- (3) J.K. Yamamoto, S.A. Markgraf, and A.S. Bhalla, " $\text{Sr}_x\text{Ba}_{1-x}\text{Nb}_2\text{O}_6$  Single Crystal Fibers: Dependence of Crystal Quality on Growth Parameters," *J. Cryst. Growth*, **123**, 423-435 (1992).
- (4) D.A. McHenry, "Optical and Electrooptical Properties of Lead Magnesium Niobate-Lead Titanate," Ph.D. Thesis, Penn State University (1992).
- (5) F.T.S. Yu, S. Yin, F. Zhao, H. Zhou, and A.S. Bhalla, "Wavelength Multiplexing Fiber Holographic Construction Using a Ce and Fe Doped PR Fiber with a Tunable Visible Light Laser Diode," *IEEE Photonics Tech. Letters*, **5**, 1230-1233 (1993).
- (6) J. M. Pova, Ruyan Guo and A.S. Bhalla, "Linear Electrooptic Coefficients Measured Utilizing Modified Mach-Zehnder Interferometer Technique," *Proceedings of Thirty-Eighth Brazilian Congress of Ceramics*, Blumenau, Brazil (June 18-21, 1994).
- (7) Francis T.S. Yu, Shizhuo Yin, Jianzhong Zhang, and Ruyan Guo, "Application of Fiber Speckle Hologram to Fiber Sensing," *Applied Optics*, **33**(22) 5202-3 (1994).
- (8) J.M. Pova, R. Guo, and A.S. Bhalla, "Low Temperature Dielectric Relaxation Phenomena in Relaxor Ferroelectric Strontium Barium Niobate," *Ferroelectrics* **158**, 283-288 (1994).

## 10. PRESENTATIONS

- (1) R. Guo, D. A. McHenry, A. S. Bhalla, and L. E. Cross, "Electrooptic Properties of Lead Barium Niobate (PBN) Single Crystals," First International Meeting on Nonlinear Optics: Materials, Phenomena and Devices (NLO'90), July 16-20, 1990, Kauai, Hawaii. (p.257)
- (2) R. Guo, D. A. McHenry, A. S. Bhalla, and L. E. Cross, "Optical and Electrooptic Properties of Lead Barium Niobate Single Crystals," 93th Annual American Ceramic Society Meeting, Apr. 29-May 6, 1991, Cincinnati.
- (3) R. Guo, D.A. McHenry, A.S. Bhalla, and L.E. Cross, "Electrooptic Properties of Lead Barium Niobate (PBN) Single Crystals," International Symposium on Application of Ferroelectrics, Aug. 30-Sept. 2, 1992, Greenville, South Carolina.
- (4) A.S. Bhalla, J. Yamamoto, and R. Guo, "Electrical and Optical Properties of Single Crystal Fibers and Crystals of Tungsten Bronzes," INDO-US Workshop on Synthesis and Processing of Advanced Materials, Mar. 22-24, 1992, Delhi, India.
- (5) A.S. Bhalla, J. Yamamoto, and R. Guo, "Single Crystal Fibers for Integrated Optics Applications," (invited) International Symposium on Integrated Ferroelectrics, Mar. 9-11, 1992, San Francisco, California.

- (6) A.S. Bhalla, J. Yamamoto, and R. Guo, "Electrical and Optical Properties of Single Crystal Fibers and Crystals of Tungsten Bronzes," INDO-US Workshop on Synthesis and Processing of Advanced Materials," Mar. 22-24, 1992, Delhi, India.
- (7) Ruyan Guo, "Electrooptic Properties of Ferroelectric Lead Barium Niobate (PBN) Single Crystals," Sixth US-Japan Seminar on Dielectric and Piezoelectric Ceramics," Nov. 11-12, 1993, Maui, Hawaii (Extended abstract published in the proceeding, p.298-301).
- (8) J.M. Pova, R. Guo, and A.S. Bhalla, "Low Temperature Dielectric Phenomena in Relaxor Ferroelectric Strontium Barium Niobate Single Crystals," The 8th International Meeting on Ferroelectrics, Aug. 1993, Geithersburg, Maryland.
- (9) J.M. Pova, Ruyan Guo and A.S. Bhalla, "Linear Electrooptic Coefficients Measured Utilizing Modified Mach-Zehnder Interferometer Technique," Thirty-eighth Brazilian Congress of Ceramics, June 18-21, 1994, Blumenau, Brazil.
- (10) J.M. Pova, Ruyan Guo, and A.S. Bhalla, "Low Temperatures Dielectric Relaxation of Tungsten Bronze Single Crystals," XVII Meeting of National Society of Physics on Condensed Materials, June 7-11, 1994, Caxambu, MG, Brazil.
- (11) Ruyan Guo, J.F. Wang, J.M. Pova, and A.S. Bhalla, "Temperature Dependent Electrooptic Properties of Lead Barium Niobate and Strontium Barium Niobate Single Crystals," The Ninth IEEE International Symposium on the Applications of Ferroelectrics, Aug. 7-10, 1994, University Park, Pennsylvania.
- (12) F.T.S. Yu, A.S. Bhalla, S. Yin, F. Zhao, Z.K. Wu, D.M. Salemo, "(Ce,Fe):LiNbO<sub>3</sub> Photorefractive Crystal: Material Properties and Applications" (invited), The Ninth IEEE International Symposium on the Applications of Ferroelectrics, Aug. 7-10, 1994, University Park, Pennsylvania.

## 11. PARTICIPANTS

Name	Status	Remarks
L. Eric Cross	Evan Pugh Professor of Electrical Engineering	Co-PI
Amar S. Bhalla	Prof. of Solid State Science & Senior Scientist	Co-PI
Frank W. Ainger	Senior Scientist	
Qiming Zhang	Senior Research Associate	
J. K. Yamamoto	Research Assistant	Ph.D. (1991)
D. A. McHenry	Research Assistant	Ph.D. (1992)
Ruyan Guo	Faculty Research Associate	
J. Pova	Visiting Professor	
B.M. Jin	Visiting Research Associate	
Srikanth	Post-Doctoral Research Associate	

**Appendix 1.**

**“Electrical and Optical Properties of Relaxor Ferroelectrics,” Ferroelectrics, 102, 161  
(1990).**

**D. A. McHenry  
J.R. Giniewicz  
T.R. Shrout  
S.J. Jang, and  
A.S. Bhalla**

## ELECTRICAL AND OPTICAL PROPERTIES OF RELAXOR FERROELECTRICS

D. A. MCHENRY, J. R. GINIEWICZ, T. R. SHROUT, S. J. JANG and  
A. S. BHALLA

*Materials Research Laboratory, The Pennsylvania State University,  
University Park, Pennsylvania 16802 USA*

*(Received May 1, 1989)*

The dielectric and optic/electro-optic properties of hot-pressed ceramics of composition  $(1-x)(\text{Pb}_{1-y}\text{La}_y)(\text{Mg}_{1/3}\text{Nb}_{2/3})\text{O}_3 - x\text{PbTiO}_3$  ( $y = 0.01$ ) have been investigated. The materials exhibit high peak dielectric constants ( $>20000$ ) with typical relaxor ferroelectric behavior. The ceramics are adequately transparent for optical and electro-optical evaluation with transmission better than 50% at 600 nm. High refractive indices are observed ( $>2.5$  at 632.8 nm) and the dispersion of the refractive index is well described by a single-term Sellmeier equation. The temperature dependence of the refractive index exhibits a linear region above 390°C and a polarization induced decrease of the index via the electro-optic effect below this temperature. The transverse quadratic electro-optic coefficients,  $(R_{11}-R_{12})$  and  $(g_{11}-g_{12})$ , were evaluated both as a function of temperature and frequency. Electro-optic switching experiments indicate rapid response of less than 1  $\mu\text{sec}$ , suitable for transverse shutter mode operation.

### 1. INTRODUCTION

Relaxor ferroelectrics such as  $\text{Pb}(\text{Mg}_{1/3}\text{Nb}_{2/3})\text{O}_3$  and its solid solution with  $\text{PbTiO}_3$  are of particular interest for applications as multilayer capacitors,<sup>1</sup> electrostrictive actuators,<sup>2,3</sup> and piezoelectric transducers.<sup>4</sup> These applications are based on the exceptional dielectric and electrostrictive properties as well as the low thermal expansion exhibited by these materials.<sup>6,7</sup> Recently, relaxor ferroelectrics have been investigated for a variety of electro-optic properties; good electro-optic switching times and modest half-wave voltages,  $V_\pi$ , could make these materials viable alternatives to the  $(\text{Pb},\text{La})(\text{Zr},\text{Ti})\text{O}_3$  (PLZT) compositions conventionally used in electro-optic devices.<sup>8</sup> In addition to evaluating their device potential, optical property measurements on relaxors can substantiate previous studies in determining the onset and magnitude of the polarization for diffuse phase transitions of relaxor ferroelectrics.<sup>9,10</sup>

Typical perovskite relaxor ferroelectrics of the form  $\text{ABO}_3$  generally occur with the *A* and/or *B* sites shared by two or more cations whose valence and ionic radii are suitable for maintaining a stable atomic configuration. Both sites may be occupied by more than one kind of cation as in the  $(\text{Pb},\text{La})(\text{Zr},\text{Ti})\text{O}_3$  (PLZT) series of compounds where oxygen vacancies further compensate for the charge imbalances arising from the substitution of  $\text{La}^{3+}$  for  $\text{Pb}^{2+}$  on the *A*-site.<sup>11</sup> Compounds and complex compositions which involve the occupation of the *B*-site only by two or more cations are exemplified by  $\text{Pb}(\text{Mg}_{1/3}\text{Nb}_{2/3})\text{O}_3$  (PMN) and  $\text{Pb}(\text{Zn}_{1/3}\text{Nb}_{2/3})\text{O}_3$  (PZN) and their solid solutions with  $\text{PbTiO}_3$ .

$\text{Pb}(\text{Sc}_{1/2}\text{Ta}_{1/2})\text{O}_3$  and  $\text{Pb}(\text{Sc}_{1/2}\text{Nb}_{1/2})\text{O}_3$  are compounds for which the ionic valence and size as well as the relative distribution of their *B'* and *B''* cations on the *B*-site

allow for 1:1 ordering when the material is in a ferroelectric state, a condition detectable by means of x-ray diffraction, electron diffraction, and Raman scattering.<sup>12</sup> A model has been proposed for PMN in which regions of ordered (Mg-rich) and disordered (Nb-rich) regions coexist between which space charges are generated which effectively charge compensate thereby limiting the degree of order possible in the system.<sup>13</sup> This state of disorder is believed to lead to the "glassy" polarization behavior observable in the temperature dependences of both the electrostrictive strain and the refractive index exhibited by materials from these systems. Based on the values of these quantities as a function of temperature, a "glassy" polarization,  $P_d$ , which bears a quadratic relationship to the induced strain and the induced birefringence through the electrostriction and the quadratic electro-optic effect (Kerr Effect) is found to persist for a broad range of temperatures above  $T_c$  in contrast to the more abrupt disappearance of the reversible polarization,  $P_r$ , generally observed in normal ferroelectrics.<sup>9,10</sup>

The weak field dielectric permittivity and  $\tan\delta$  as a function of temperature exhibit broad frequency dependent (i.e.-dispersive) maxima as shown in Figure 1 characteristic of a diffuse ferroelectric phase transition for materials with no long-range structural order such as the  $\text{Pb}(\text{B}'_{1/3}\text{B}''_{2/3})\text{O}_3$  compounds and solid solutions. This behavior has been described by the theory of "compositional fluctuations" in which local variations in composition lead to the formation of ferroelectric (polar) and paraelectric (non-polar) microregions on the order of 100–200 Å.<sup>14</sup> Each polar region will possess its own Curie temperature dependent on its local composition so that the material as a whole will proceed through the transition over a range of temperatures known as the Curie range. Polar regions with volumes on the order of  $10^2$  Å are unstable against thermal agitation and, hence, the distribution and relative density of the microregions are strongly temperature dependent.<sup>10</sup> The dielectric response measured as a function of temperature and degree of long-range order for systems such as  $\text{Pb}(\text{Sc}_{1/2}\text{Ta}_{1/2})\text{O}_3$ , whose degree of structural (dis)order may be varied by controlled heat treatment, demonstrates a direct correlation between the degree of ordering of B-site cations and the diffuseness of the dielectric response, where a decrease in structural order leads to increased "smearing" of the permittivity maximum.<sup>15,16</sup> The observed relationship between structural order and the diffuseness of the phase transition has been cited as evidence in sup-

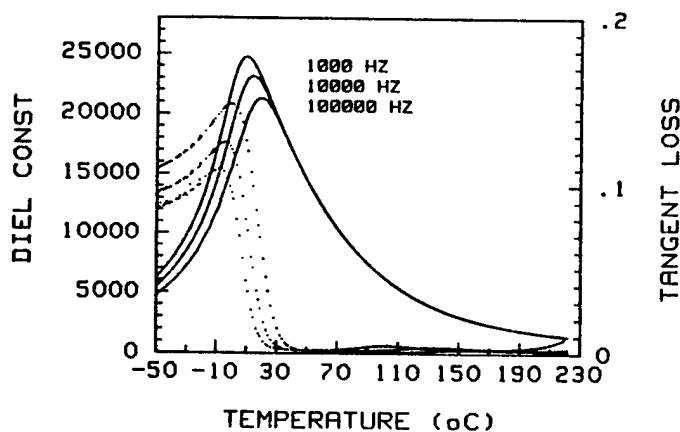


FIGURE 1  $K(T)$  and  $\tan\delta(T)$  for  $(0.93)(\text{Pb}_{0.99}\text{La}_{0.01})(\text{Mg}_{1/3}\text{Nb}_{2/3})\text{O}_3 - (0.07)\text{PbTiO}_3$

port of the "composition fluctuation" model.<sup>10</sup> Recent studies on  $(1-x)\text{Pb}(\text{Mg}_{1/3}\text{Nb}_{2/3})\text{O}_3 - (x)\text{PbTiO}_3$ , ( $x = 0.07$  and  $0.1$ ) and La-substituted compositions prepared by hot-uniaxial pressing as transparent ceramics have generated new data which suggests promising application potential and supports models previously proposed concerning the "glassy" polarization behavior<sup>9</sup> of this family of materials. The compositions investigated demonstrate the classic diffuse phase transition behavior (Figure 1) of PMN with a distinct enhancement of the electromechanical and capacitive properties. The optical and electro-optical character of these materials are also of interest in the development of relaxor-based optical devices and for further advances in the understanding of the fundamental mechanisms contributing to the diffuse phase transition. The results of this investigation are presented with particular regard to fundamental concepts and application considerations.

## 2. SAMPLE PREPARATION

In order to produce polycrystalline specimens transparent enough for optical/electro-optical property measurements, desirable characteristics including uniform grain-growth, high density, and the elimination or reduction of second phases are requirements not easily achievable by conventional sintering methods. The specimens used in this investigation were prepared by means of hot-uniaxial pressing with additions of excess  $\text{PbO}$  and  $\text{La}_2\text{O}_3$  to aid in densification and to promote transparency. Powders of  $(1-x)\text{PMN}-(x)\text{PT}$ , ( $x = 0.07$  and  $0.1$ ) were prepared by the columbite precursor method<sup>1</sup> in order to produce phase-pure compositions. Both excess  $\text{PbO}$  ( $\sim 2\text{--}5$  mol%) and/or  $\text{La}_2\text{O}_3$  ( $0.5$  mol%) compositional modifications were made to allow for a range of hot-pressing conditions and to enhance transparency. In general, ceramics with densities greater than 99.7% and optical transparency were achieved.<sup>5</sup>

## 3. EXPERIMENTAL RESULTS AND DISCUSSION

Transparent ferroelectric ceramics as exemplified by PLZT have demonstrated considerable usefulness as electro-optic materials. Practical applications for these ceramics include use in such devices as optical shutters, modulators, displays, and gate arrays for optical data processing.<sup>17</sup> Recent measurements of  $(1-x)(\text{Pb}_{1-y}\text{La}_y)(\text{Mg}_{1/3}\text{Nb}_{2/3})\text{O}_3 - x\text{PbTiO}_3$  (PLMN-PT) relaxor ferroelectric ceramics indicate that this and similar compositions can be made with reasonable transparency and large electro-optic coefficients comparable to those of the PLZT compositions currently in use.<sup>8</sup>

The range of transparency for the ceramics under investigation extends through the visible and into the near IR with transmission in excess of 50% at wavelengths longer than 550 nm for samples 1.0 mm thick. The fundamental UV optical absorption wavelength of about 375 nm is in agreement with the wavelength reported for other corner-shared oxygen-octahedra materials.<sup>18</sup> Improvements in optical transmission characteristics for PLMN-PT ceramics could be anticipated with the use of ultra-high purity powders and improved processing conditions.

The dispersion of the refractive index was measured by means of the method of minimum deviation.<sup>8,9</sup> The dispersion data were fitted to a single-term Sellmeier oscillator equation of the form,

$$n^2 - 1 = S_0 \lambda_0^2 / (1 - \lambda_0^2 / \lambda^2) = E_d E_0 / (E_0^2 - E^2) \quad (1)$$

where  $E$  and  $E_0$  are the energy of the incident light and the average oscillator energy, respectively,  $\lambda$  and  $\lambda_0$  are the wavelength of the incident light and the average oscillator position respectively, and  $E_d$  is the dispersion energy.<sup>18</sup> The Sellmeier parameters are derived from a straight-line least squares fit of  $(n^2 - 1)^{-1}$  vs.  $(1/\lambda^2)$ . The room temperature Sellmeier parameters for various  $(1-x)$ -( $\text{Pb}_{1-y}\text{La}_y$ )( $\text{Mg}_{1/3}\text{Nb}_{2/3}$ ) $\text{O}_3$  -  $x\text{PbTiO}_3$  compositions and the end-members PMN and  $\text{PbTiO}_3$  of the system appear in Table I. The temperature dependence of the Sellmeier parameters  $E_0$  and  $E_d$  are shown, respectively, in Figures 2a and 2b as determined from measuring the refractive index to high temperature for .93 PLMN - .07 PT. The slope,  $dE_0/dT$ , is related to the shift of the absorption spectra as a function of temperature. This change is apparently linear in the temperature range measured with a value of approximately  $-6.48 \times 10^{-4}$  eV/°C.

Refractive index measured as a function of temperature can also be a sensitive indicator of polarization fluctuations in the precursor region in the vicinity of the paraelectric-ferroelectric transition. The temperature dependence of (0.93)-( $\text{Pb}_{0.99}\text{La}_{0.01}$ )( $\text{Mg}_{1/3}\text{Nb}_{2/3}$ ) $\text{O}_3$  - (0.07) $\text{PbTiO}_3$  at four different wavelengths is shown in Figure 3. An essentially linear region is observed at high temperatures. A departure from linearity occurs at a temperature of about 390°C at all four wavelengths. The behavior of the refractive index below this temperature (referred to as  $T_d$ )<sup>9,19</sup> is believed to be significantly affected by locally ordered yet randomly oriented polarization,  $P_d$ , which may occur well above the Curie temperature in relaxor ferroelectrics. Hence, for perovskite ferroelectric ceramics the refractive index departure from linear behavior  $\Delta n$  can be given by the expression for the quadratic electro-optic effect with respect to the polarization,

$$\Delta n = (\Delta n_{\parallel} + 2\Delta n_{\perp})/3 = -(n_0^3)/2 [(g_{33} + 2g_{13})/3]P_d^2 \quad (2)$$

where  $\Delta n$  is expressed as an average of the  $\Delta n$ 's both parallel and perpendicular to the polar [111] directions, and  $n_0$  is the refractive index of the undistorted indicatrix,  $P_d$  is the local polarization, and the  $g$  coefficients are the appropriate

TABLE I  
Refractive Index Parameters for the PMN-PT System

	PMN <sup>5</sup>	(0.93)( $\text{Pb}_{0.99}\text{La}_{0.01}$ ) ( $\text{Mg}_{1/3}\text{Nb}_{2/3}$ ) $\text{O}_3$ - (0.07) $\text{PbTiO}_3$	0.90 PMN- 0.10 PT	$\text{PbTiO}_3$ <sup>20</sup>
$n$ @ 632.8 nm	2.5219	2.5399	2.5455	2.688
$\lambda_0$ ( $\mu\text{m}$ )	0.216	0.218	0.220	0.222
$S_0$ ( $\times 10^{14} \text{ m}^{-2}$ )	1.013	1.012	1.00	1.09
$E_0$ (eV)	5.73	5.69	5.64	5.59
$E_d$ (eV)	27.2	27.40	27.31	30.3
$f$ (eV) <sup>2</sup>	156	155.9	154	168
$E_d/S_0$ ( $\times 10^{-14} \text{ eVm}^2$ )	5.66	5.62	5.64	5.13

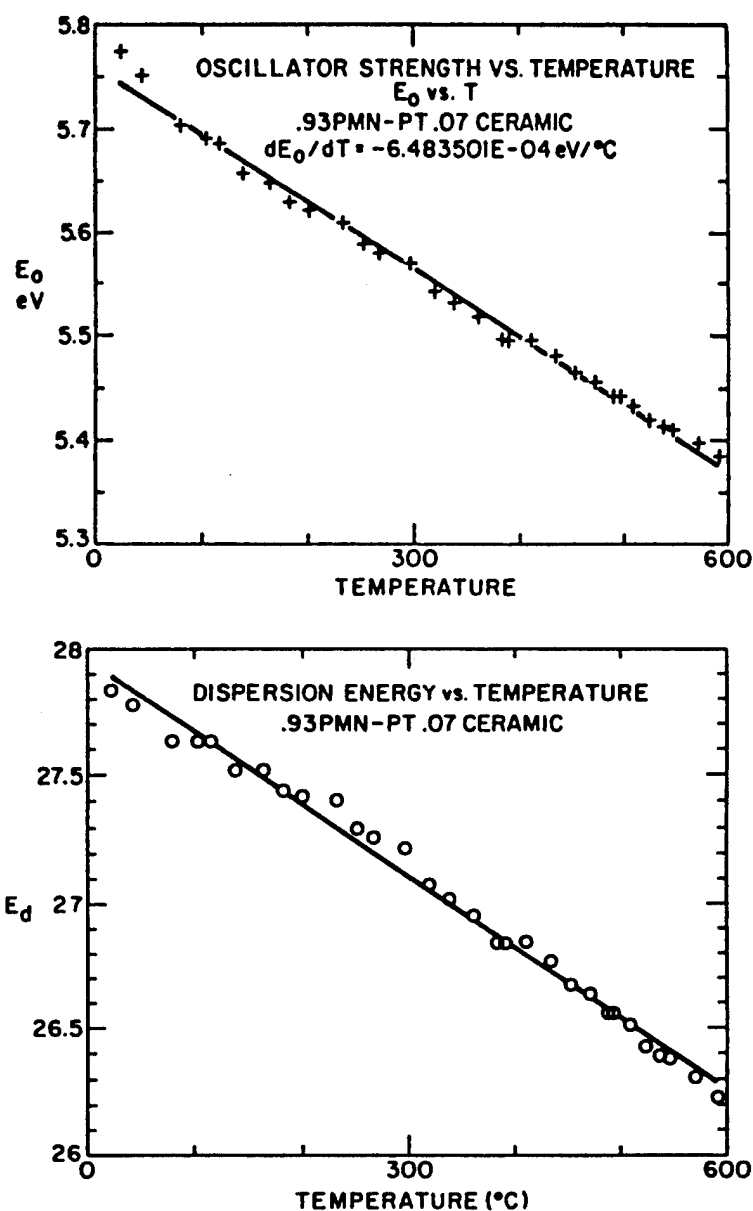


FIGURE 2 (a)  $E_0$  vs. temperature and (b)  $E_d$  vs. temperature for  $(0.93)(\text{Pb}_{0.99}\text{La}_{0.01})(\text{Mg}_{1/3}\text{Nb}_{2/3})\text{O}_3 - (0.07)\text{PbTiO}_3$

coefficients for this symmetry.<sup>19</sup> The magnitude of the average random local polarization,  $P_d$ , is evaluated by means of equation (2) using the measured values of  $n_0$ ,  $\Delta n$ , and the electro-optic  $g$  coefficients.<sup>8</sup> Values of  $P_d$  calculated in this way for  $(0.93)(\text{Pb}_{0.99}\text{La}_{0.01})(\text{Mg}_{1/3}\text{Nb}_{2/3})\text{O}_3 - (0.07)\text{PbTiO}_3$  appear in Figure 4.

The PLMN-PT ceramics investigated at room temperature exhibit "slim loop" ferroelectric hysteresis (Figure 5)  $P$  vs.  $E$ . The material has pseudocubic symmetry in its undistorted state; with the application of an electric field a uniaxial birefringent (presumably rhombohedral) ferroelectric phase may be induced.

The electro-optic effect for active optical ceramics operated in a transverse shutter mode can be described in terms of the expression for the quadratic electro-optic

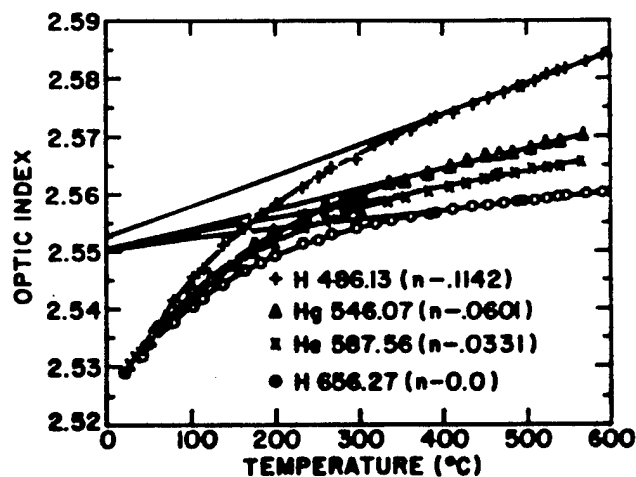


FIGURE 3 Refractive Index vs. temperature for  $(0.93)(\text{Pb}_{0.99}\text{La}_{0.01})(\text{Mg}_{1/3}\text{Nb}_{2/3})\text{O}_3 - (0.07)\text{PbTiO}_3$

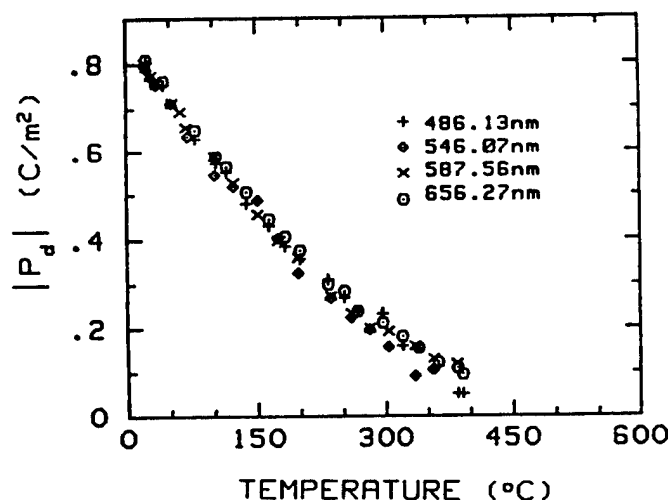


FIGURE 4 Polarization,  $P_d$ , as a function of temperature calculated from refractive index measurements using equation (2).

effect which relates to the applied electric field as follows:

$$\Delta n = -\left(\frac{1}{2}\right) n_0^3 (R_{11}-R_{12}) E_1^2 \quad (3)$$

where  $\Delta n$  is the induced birefringence,  $n_0$  is the refractive index of the undistorted indicatrix,  $R_{11}-R_{12}$  is the effective averaged unclamped (low frequency) quadratic electro-optic coefficient, and  $E_1$  is the applied field. The transverse electro-optic response represented by  $R_{11}-R_{12}$  is typically the largest induced in a perovskite ferroelectric ceramic.

The quadratic electro-optic coefficients were determined by means of the AC Senarmont compensator setup illustrated in Figure 6. The induced birefringence at room temperature is plotted against the square of the electric field in Figure 7. It can be seen that the electro-optic response is well described by the quadratic electro-optic effect where the proportionality constant relating  $\Delta n$  and  $E^2$  yields  $R_{11}-R_{12} = 2.1 \times 10^{-16} \text{ (m}^2/\text{V}^2\text{)}$  at room temperature. The temperature depend-

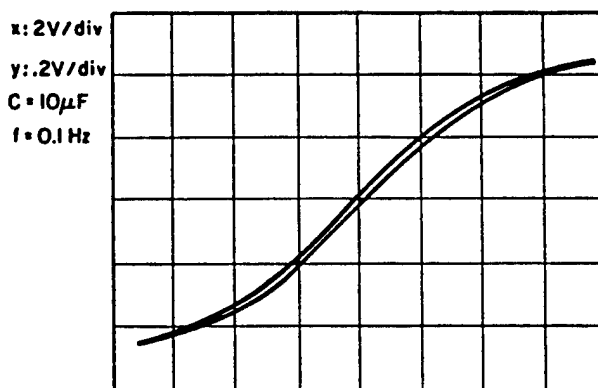


FIGURE 5 Ferroelectric hysteresis loop for  $(0.93)(\text{Pb}_{0.99}\text{La}_{0.01})(\text{Mg}_{1/3}\text{Nb}_{2/3})\text{O}_3 - (0.07)\text{PbTiO}_3$  at  $T = 20^\circ\text{C}$

## A.C. SENARMONT COMPENSATOR ELECTROOPTIC EXPERIMENT

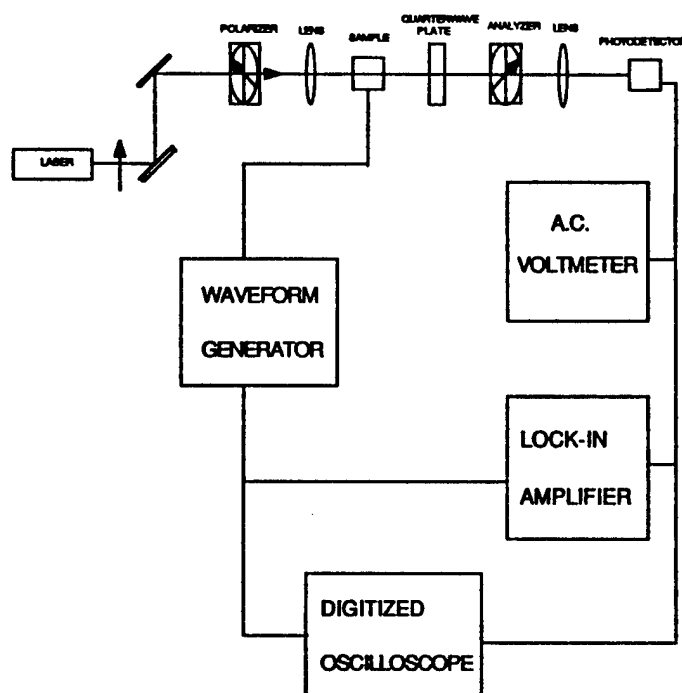


FIGURE 6 Schematic of the Senarmont Compensator  $\Delta n(E)$  measurement system

ence of  $R_{11}-R_{12}$  is shown in Figure 8 (curve-1). The electric field-related quadratic electro-optic coefficients are clearly temperature dependent. This is generally true for ferroelectrics operated near a phase transition where the values of the dielectric permittivity also change considerably with temperature. The maximum dielectric constant for small-field and low-frequency (1 KHz) conditions occurs at  $T \sim 9^\circ\text{C}$  for  $(0.93)\text{PLMN} - (0.07)\text{PT}$  and decreases markedly at higher temperatures above the Curie range, a trend reflected in the temperature dependence of the  $R$ -coefficients.

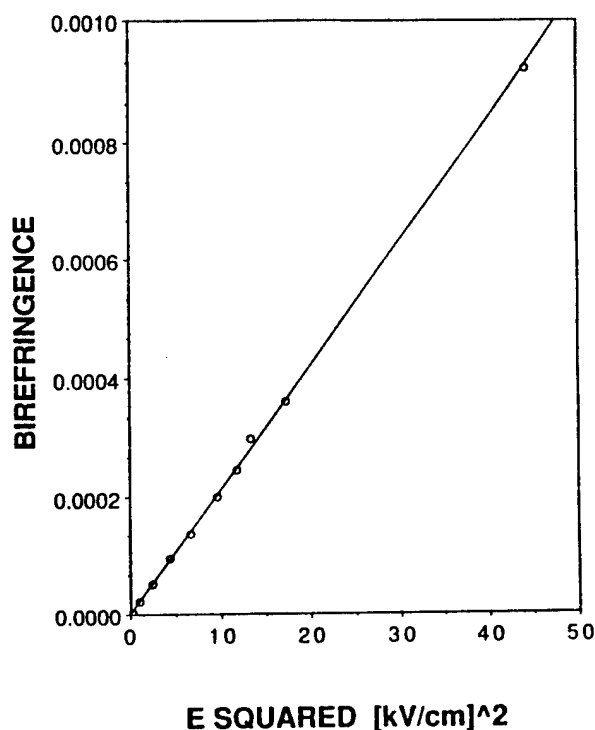


FIGURE 7 Induced birefringence  $\Delta n$  vs.  $E^2$  for  $(0.93)(\text{Pb}_{0.99}\text{La}_{0.01})(\text{Mg}_{1/3}\text{Nb}_{2/3})\text{O}_3 - (0.07)\text{PbTiO}_3$  at  $T = 20^\circ\text{C}$

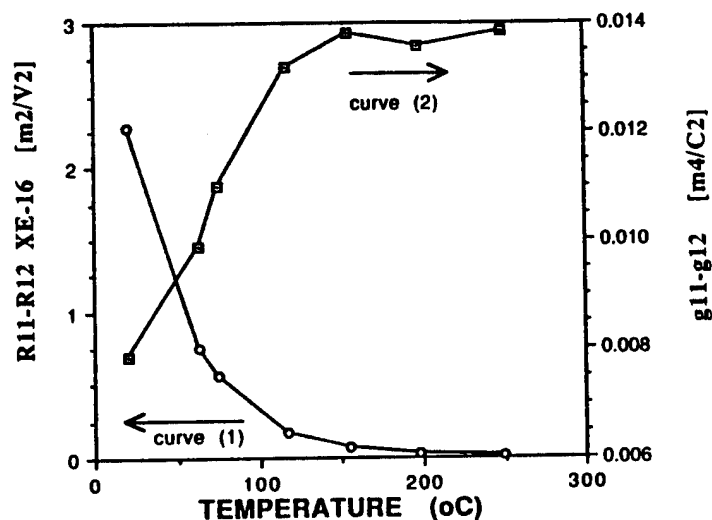


FIGURE 8 1.)  $(R_{11}-R_{12})$  vs. temperature for  $(0.93)(\text{Pb}_{0.99}\text{La}_{0.01})(\text{Mg}_{1/3}\text{Nb}_{2/3})\text{O}_3 - (0.07)\text{PbTiO}_3$ ; 2.)  $(g_{11}-g_{12})$  vs. temperature for  $(0.93)(\text{Pb}_{0.99}\text{La}_{0.01})(\text{Mg}_{1/3}\text{Nb}_{2/3})\text{O}_3 - (0.07)\text{PbTiO}_3$

Alternatively, the electro-optic effect may be expressed in terms of the polarization as,

$$\Delta n = -(1/2) n_0^3 (g_{11}-g_{12}) P_1^2 \quad (4)$$

This formulation is generally preferable when dealing with ferroelectric materials

since the response in terms of the polarization relates more directly to the fundamental polarization-related phenomena that accompany ferroelectric transitions. The two types of quadratic electro-optic coefficients are related through the dielectric permittivity as,

$$(g_{11}-g_{12}) = (R_{11}-R_{12})/(\epsilon \epsilon_0)^2 \quad (5)$$

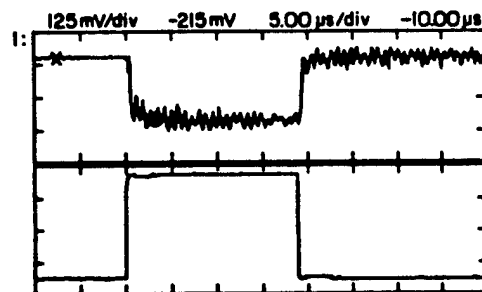
where  $\epsilon$  is the dielectric permittivity and  $\epsilon_0$  is the permittivity of free space.

The temperature dependence of  $g_{11}-g_{12}$  is shown in Figure 8 (curve-2). The polarization electro-optic coefficients,  $g_{ij}$ , are usually much less temperature dependent than the electric field-related coefficients,  $R_{ij}$ . For the polarization optic coefficients there is a gradual increase with temperature with a leveling off to  $g_{11}-g_{12} = 0.014$  ( $C^2/m^4$ ) at about  $200^\circ C$ . The temperature dependence of the  $g$ -coefficients has been reported as confirming the presence of polar phase regions for relaxors in the same temperature range where the quadratic dependence of the birefringence on applied electric field holds true.<sup>25</sup>

It has been previously observed that the polarization-optical coefficients are nearly the same for all oxygen octahedra materials ( $g_{11}-g_{12} = 0.11 \pm 0.02$   $m^4/C^2$ ). It has also been noted, however, that Pb-based perovskites (including the ferroelectric relaxors) are exceptions to this, exhibiting  $g$ -coefficients that are an order of magnitude smaller than the value common to the other oxygen-octahedra materials. This lowering of the  $g$ -coefficient in Pb-based systems has been attributed to a polarization induced shift of the electronic band gap due to the displacement of the  $Pb^{2+}$  sublattice which is generally not accounted for in the formulation of the  $g$ -coefficients.<sup>20</sup>

The frequency dependence of ( $g_{11}-g_{12}$ ) has been measured and the response is observed to be nondispersive at low frequencies ( $<100$  KHz) in agreement with the frequency dependence of the dielectric permittivity in this same frequency regime. This is expected for the composition under investigation since the Curie range over which the diffuse dielectric and electro-optic behavior occurs is below

#### ELECTROOPTIC SWITCHING RESPONSE



TOP: SAMPLE TRANSMISSION VS. TIME  
BOTTOM: APPLIED SQUARE VOLTAGE PULSE

$.93(Pb_{0.99}La_{0.01})(Mg_{1/3}Nb_{2/3})O_3 - .07 PbTiO_3$

RESPONSE TIME ( $<1\mu sec$ )  
VOLTAGE PULSE  $1.15$  KV/CM

FIGURE 9 Signal Response as a function of time for  $(0.93)(Pb_{0.99}La_{0.01})(Mg_{1/3}Nb_{2/3})O_3 - (0.07)PbTiO_3$

room temperature. This is a possible advantage in terms of device application over the PLZT compositions generally employed which exhibit dispersive dielectric behavior at room temperature that translates to the electro-optic frequency response as well.<sup>21</sup>

Response times for electro-optic switching have been examined by applying square wave pulses of different voltages and pulse widths. As compared with the switching times reported for bulk PLZT of 1–10  $\mu\text{sec}$ <sup>22–25</sup> the response time for these PLMN-PT ceramic electro-optic switches is rapid; less than 1  $\mu\text{sec}$ . The response of a  $(0.93)(\text{Pb}_{0.99}\text{La}_{0.01})(\text{Mg}_{1/3}\text{Nb}_{2/3})\text{O}_3 - (0.07)\text{PbTiO}_3$  sample to a 157 V square pulse of about 18  $\mu\text{sec}$  duration is shown in Figure 9. It was observed that the rise time consistently was  $<1 \mu\text{sec}$  and that the fall time is generally faster than the rise time. The post-switching oscillations are due to electrostrictive vibrations in the unclamped ceramic. This electrostrictive response to the applied voltage contributes via the strain-optic effect to the amplitude of the transmitted signal.

#### 4. CONCLUSIONS

- (1) The various descriptions of the diffuse behavior associated with relaxor ferroelectric compounds as expressed in terms of the theory of compositional fluctuations<sup>14</sup> and in particular, the model concerning “glassy” polarization behavior<sup>9,19</sup> is consistent with the data for  $(0.93)(\text{Pb}_{0.99}\text{La}_{0.01})(\text{Mg}_{1/3}\text{Nb}_{2/3})\text{O}_3 - (0.07)\text{PbTiO}_3$  ceramic specimens investigated. The weak field dielectric permittivity and  $\tan\delta$  as a function of temperature exhibit the broad frequency dependent maxima characteristic of the diffuse ferroelectric phase transition of materials with no long-range structural order. Evaluation of the refractive index as a function of frequency and temperature evidence a persistence of a non-reversible average local polarization to temperatures (with a  $T_d$  of approximately 390°C) very much higher than the temperature of the dielectric maximum. This trend follows that observed for other PMN and PZN relaxors and is well described by the relationships derived to describe “glassy” polarization behavior in these systems.
- (2) The La-modified  $(0.93)\text{Pb}(\text{Mg}_{1/3}\text{Nb}_{2/3})\text{O}_3 - (0.7)\text{PbTiO}_3$  compositions investigated exhibit good electro-optic response, rapid switching time and a moderate half-wave voltage as compared to PLZT indicating future possibilities for electro-optic device applications. The low transition temperature of this composition allows for efficient room temperature operation of such devices, a possible advantage over the PLZT compositions generally employed which exhibit dispersive dielectric behavior at room temperature thereby limiting, to a certain extent, the electro-optic frequency response of the device.<sup>21</sup>

#### ACKNOWLEDGEMENT

The authors wish to thank Dr. K. Vedam for the use of his optical equipment and to Dr. Qiming Zhang, Dr. Wuyi Pan, and Roy Austin, Jr. for their assistance in this investigation. The contributions of Frank Ainger of Plessey Co. in the preparation of the specimens and the support of the DARPA Nanocomposite Project are also gratefully acknowledged.

## REFERENCES

1. T. R. Shrout and A. Halliyal, *American Ceramic Society Bulletin*, **66**(4), 704 (1987).
2. K. Uchino, *American Ceramic Society Bulletin*, **65**(4), 647 (1986).
3. K. Uchino, S. Nomura, S. J. Jang, L. E. Cross and R. E. Newnham, *Journ. Appl. Phys.*, **51**(2), 1142 (1980).
4. S. Takahashi, A. Ochi, M. Yonezawa, T. Yano, T. Hamatsuki and I. Fukui, *Ferroelectrics*, **50**, 181 (1983).
5. N. Kim, W. Huebner, S.-J. Jang and T. R. Shrout, *Ferroelectrics*, **93**, 341 (1989).
6. S. J. Jang, Ph.D. Thesis, The Pennsylvania State University (1979).
7. K. Uchino, S. Nomura, L. E. Cross, R. E. Newnham and S. J. Jang, *Journ. Material Science*, **16**, 569 (1981).
8. D. McHenry, J. R. Giniewicz, S. J. Jang, A. Bhalla and T. R. Shrout, *Ferroelectrics*, **93**, 351 (1989).
9. G. Burns and F. Dacol, *Phase Transitions*, **5**, 261 (1983).
10. L. E. Cross, *Ferroelectrics*, **76**, 241 (1987).
11. K. Okasaki, M. Masuda, S. Tashiro, and S. Ishibashi, *Ferroelectrics*, **22**, 681 (1978).
12. N. Setter, Ph.D. Thesis, The Pennsylvania State University, (1980).
13. A. D. Hilton, C. A. Randall, D. J. Barber and T. R. Shrout, (to be published).
14. G. A. Smolenskii, A. I. Agranovskaya, *Sov. Phys. Solid State*, **1**, 1429 (1959).
15. C. G. F. Stenger and A. J. Burggraaf, *physica status solidi (a)*, **61**, 275 (1980).
16. N. Setter and L. E. Cross, *Journ. Appl. Phys.*, **54**, 4356 (1980).
17. G. H. Haertling and C. E. Land, *Journ. of the Am. Ceram. Society*, **54**, 1 (1971).
18. M. DiDomenico, Jr. and S. H. Wemple, *Journ. of Appl. Phys.*, **40**(2), 720 (1968).
19. G. Burns and F. H. Dacol, *Physical Review B*, **28**(5), 2527 (1983).
20. P. D. Thatcher, *Applied Optics*, **16**, 3210 (1977).
21. F. S. Chen, *Optics Communication*, **6**, 279 (1972).
22. J. R. Maldonado and A. H. Meitzler, *IEEE Transactions of Electronic Devices*, **148** (1970).
23. G. Wolfram, *Ferroelectrics*, **10**, 39 (1971).
24. C. J. Kirkby, *Ferroelectrics*, **37**, 567 (1981).
25. M. Ozolinsh, *Mat. Res. Bull.*, **17**, 741 (1982).

**Appendix 2.**

**“Strontium Barium Niobate Single Crystal Fibers: Optical and Electro-optic Properties,”**  
*J.Appl. Phys.* 70, 3215-3222 (1991).

J.K. Yamamoto  
Dean A. McHenry, and  
A.S. Bhalla

# Strontium barium niobate single-crystal fibers: Optical and electro-optic properties

Joyce K. Yamamoto,<sup>a)</sup> Dean A. McHenry, and Amar S. Bhalla

The Pennsylvania State University, Materials Research Laboratory, University Park, Pennsylvania 16802

(Received 19 March 1991; accepted for publication 12 June 1991)

The room-temperature transverse electro-optic,  $r_c$ , coefficient, halfwave voltage,  $V_\pi$ , and temperature dependence of the birefringence,  $\Delta n_0(T)$ , were determined for  $\text{Sr}_{0.61}\text{Ba}_{0.39}\text{Nb}_2\text{O}_6$  single-crystal fibers produced by the laser-heated pedestal growth technique. The effect cerium doping, 0.034 at. %, had on the measured properties is also reported. Concurrent measurements on a Czochralski-grown  $\text{Sr}_{0.61}\text{Ba}_{0.39}\text{Nb}_2\text{O}_6$  single crystal enabled comparison of the single-crystal fibers to a bulk-grown single crystal. The growth rate of the  $\text{Sr}_{0.61}\text{Ba}_{0.39}\text{Nb}_2\text{O}_6$  single-crystal fibers was approximately an order of magnitude greater than the Czochralski-grown  $\text{Sr}_{0.61}\text{Ba}_{0.39}\text{Nb}_2\text{O}_6$  single crystal. The effect the rapid growth rate had on the optical properties is also discussed.

## I. INTRODUCTION

The laser-heated pedestal growth (LHPG) technique is similar to the float zone technique for single crystal growth, where the molten material is self-contained by the surface tension of the melt. It differs from the float zone technique in that the diameter of the LHPG single crystals is usually less than one millimeter, an order of magnitude smaller than conventional float zone crystals. A carbon dioxide laser serves as the energy source in the LHPG technique, making oxide materials relatively easy to grow at low power levels due to their efficient absorption of the 10.6- $\mu\text{m}$  energy. A number of oxide and nonoxide materials have been grown by this technique. Further information can be found in the literature.<sup>1</sup>

Interest in single-crystal fibers is currently directed towards a variety of structural, optical, electronic, acoustic, and magnetic applications. Single-crystal fibers can be thought to possess one-dimensional properties, and through the selection of material and crystallographic orientation, a physical property may be minimized or maximized along the fiber axis. The growth of single crystals for optical applications has focused on laser host materials, e.g., doped  $\text{Al}_2\text{O}_3$  and  $\text{Y}_3\text{Al}_5\text{O}_{12}$ ,<sup>2</sup> and optically nonlinear materials, e.g.,  $\text{LiNbO}_3$ ,<sup>3</sup> and  $\text{BaTiO}_3$ .<sup>4</sup> The photorefractive properties of  $\text{Sr}_{0.61}\text{Ba}_{0.39}\text{Nb}_2\text{O}_6$  single-crystal fibers has been reported,<sup>5</sup> where its application as a holographic storage media was evaluated.

The interest in the optical properties of  $\text{Sr}_x\text{Ba}_{1-x}\text{Nb}_2\text{O}_6$  has been fueled by the large electro-optic coefficients and low halfwave voltages.<sup>6</sup> Looking at compositions across the solid solution range, the linear electro-optic coefficients increase with increasing strontium concentration. The refractive indices,  $n_o$  and  $n_e$ , have been measured by the minimum deviation method as a function of wavelength and temperature.<sup>7</sup> The extraordinary index,  $n_e$ , was very sensitive to both temperature and composition, in agreement with electro-optic results. The longitu-

dinal electro-optic coefficient,  $r_{33}$ , was an order-of-magnitude larger than the transverse coefficients,  $r_{13}$  and  $r_{42}$ , indicating that the polar direction was the most susceptible to structural and electronic changes. These results are also supported by lattice parameter data of different compositions in the solid solution phase field.<sup>8,9</sup>

There have been several attempts to measure the electro-optic coefficients of  $\text{Sr}_{0.61}\text{Ba}_{0.39}\text{Nb}_2\text{O}_6$  (SBN61), but there has been little agreement between experimental results. The inconsistencies have been largely attributed to the temperature dependence of the optical retardation,<sup>10</sup> inferior crystal quality,<sup>11</sup> and piezoelectric,<sup>12</sup> and space-charge effects.<sup>13</sup> Recently, an interferometric technique was used to measure both the phase retardation and piezoelectric response of an undoped SBN60 single crystal, enabling the separation of each contribution to the measured coefficients.<sup>10</sup>

The addition of dopants to SBN61 served to enhance some of the optical properties. Cerium and lanthanum have been added to the congruent composition. Although cerium doping shifts the absorption edge from 0.37 to 0.50  $\mu\text{m}$ , the photorefractive sensitivity increased<sup>14</sup> and the beam fanning response time decreased<sup>15</sup> from the undoped composition. Lanthanum doping has been found to increase the transverse  $r_c$  coefficient and reduce the halfwave voltage of SBN50 single crystals.<sup>16</sup>

It was the aim of this work to investigate the optical properties of SBN single crystals grown by the LHPG technique and compare them to crystals grown by the Czochralski technique. It has been shown that these single-crystal fibers are free of compositional striations,<sup>17</sup> but studies into the differences these crystals may have from crystals grown by other techniques have not been undertaken. The very rapid growth rates possible in this growth technique may have an effect upon the physical properties, particularly since the structure of this compositional family is known to be defective.<sup>18</sup> It has been shown that the dielectric and pyroelectric properties of SBN61 are sensitive to the degree of cation ordering within the oxygen octahedra framework, induced by quenching and annealing at temperatures between 600 and 1000 °C.<sup>19</sup> The rapid

<sup>a)</sup>Present address: National Institute for Research in Inorganic Materials, 13th Group, 1-1 Namiki, Tsukuba, Ibaraki 305, Japan.

growth rates attainable with the LHPG technique were used to grow both undoped and cerium-doped SBN61 single-crystal fibers. The electro-optic transverse,  $r_c$  coefficients, halfwave voltages and temperature dependence of the birefringence were examined in both as-grown and annealed single-crystal fibers. The effect the rapid growth rate and induced cation disorder had on the optical properties were studied and the results were compared to Czochralski-grown (CZ-grown) crystals of comparable composition.

## II. EXPERIMENTAL PROCEDURE

### A. Measurement techniques

The electro-optic effect is the change of the refractive index of a crystal,  $n$ , with the application of an electric field. For linearly polarized light incident upon a crystal, the resulting refractive index ellipsoid is rotated by the applied field, thereby changing the refractive indices in the crystal. This linear field induced change in the refractive index can be expressed as

$$\Delta\left(\frac{1}{n^2}\right)_{ij} = \sum_k r_{ijk} E_k \quad (1)$$

where  $r_{ijk}$  is the linear electro-optic (Pockels) coefficient and  $E_k$  is the applied electric field.<sup>20,21</sup> For SBN, a member of point group 4mm at room temperature, the electro-optic matrix has three independent nonzero coefficients and can be expressed in reduced notation:  $r_{13} = r_{23} \neq 0$ ,  $r_{42} = r_{51} \neq 0$ ,  $r_{33} \neq 0$ .<sup>22</sup>

For the configuration of light propagating down the  $a$  axis and the electric field applied along the polar  $c$  axis, the change in birefringence for the tetragonal symmetry is expressed as

$$\Delta n(E) = \frac{1}{2}(n_o^3 r_c E_c), \quad (2)$$

where  $r_c$  is the transverse electro-optic coefficient. This transverse electro-optic coefficient can be expressed in terms of  $r_{13}$  and  $r_{33}$ :

$$r_c = r_{33} - \left(\frac{n_o}{n_e}\right)^3 r_{13}. \quad (3)$$

The halfwave voltage,  $V_\pi$  is defined as the voltage required to induce a phase shift,  $\Gamma$ , of  $\pi$  between the two polarization components or  $\Gamma(E) = \pi$ . It can also be expressed in terms of the  $r$  coefficient:<sup>20</sup>

$$V_\pi = \frac{\lambda}{n_o^3 r} \cdot \frac{d}{l}, \quad (4)$$

where  $d$  is the electrode spacing and  $l$  is the optical path length. The halfwave voltage is an important parameter used to compare the performance of different electro-optic materials.

The Senarmont compensator method was used to measure the room-temperature electro-optic coefficients and the halfwave voltages. The experimental arrangement is shown in Fig. 1. Light from a Hughes 10-mW HeNe laser, 6328 Å was passed through a polarizer oriented 45° from

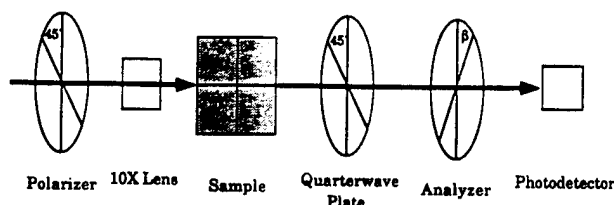


FIG. 1. Schematic drawing of the Senarmont Compensator technique used to measure the electro-optic coefficients and halfwave voltages.

the principle axis of the crystal. To reduce the laser spot size, a long focal length (10×) lens was placed before the sample. A calcite quarter-wave plate was placed after the sample with the fast axis in the same orientation as the polarizer. The analyzer was placed next in line and was oriented at an azimuthal angle  $\beta$ .

The transverse  $r_c$  coefficients and the halfwave voltages were determined by applying different ac modulating voltages across the crystal and observing the response of the transmitted light intensity.<sup>23</sup>

The analyzer is set so one half of the intensity of the transmitted light is incident upon the photodetector. The transmitted intensity varies linearly with the applied voltage, and the phase retardation is described as

$$\Gamma(\omega) = [2\pi L \Delta n(\omega) / \lambda]. \quad (5)$$

The birefringence can be calculated from the known optical path length,  $L$ , and  $\lambda$ . The birefringence can then be expressed in terms of the applied voltage using Eq. (4) and by plotting  $\Delta n$  versus the applied voltage the transverse  $r_c$  coefficient can be calculated from the slope of the curve.

The halfwave voltages were determined using a linear approximation of the halfwave voltage and is obtained without the application of large dc voltages. It is based on the application of small voltages ( $\Delta V \ll V_\pi$ ) and observing the change in the light intensity through the crystal at 50% attenuation of the transmitted light.

Using this technique, the transmitted light intensity is expressed in terms of the applied voltage<sup>24</sup>

$$\Delta I = \Delta V \left( \frac{\pi I_0}{2 V_\pi} \right) \quad (6)$$

and by plotting  $\Delta I$  vs  $\Delta V$ , the halfwave voltage can be calculated from the slope of the curve.

There are two advantages of this indirect method to measure the halfwave voltage. It eliminates the application of large voltages to the sample, thereby minimizing the possibility of depoling or damaging the single crystal. The method is also very sensitive to accurate angular positioning, where clear frequency doubling can be observed. The disadvantages are that it is sensitive to signal noise and temperature fluctuations in the output intensity, and the amplitude of the output intensity is very small, requiring careful measurement of the output intensity.<sup>23</sup>

The total birefringence is the sum of the birefringence induced by the spontaneous polarization,  $P_s$ , and by structural contributions,  $\Delta n_0(T)$ <sup>20</sup>

$$\Delta n_T = -\frac{1}{2}n_0^3(g_{11} - g_{12})P_s^2 + \Delta n_0(T), \quad (7)$$

where  $g_{11}$  and  $g_{12}$  are the quadratic electro-optic coefficients. In a ferroelectric material like SBN the birefringence,  $\Delta n_0(T)$ , decreases with increasing temperature as the ferroelectric/paraelectric transition temperature,  $T_c$ , is approached and above  $T_c$  only the high-temperature contribution remains. The small size of the single-crystal fibers prevented a direct measurement of the polarization-induced birefringence, but measurement of the temperature dependent contribution was possible by monitoring the phase modulation of the plane polarized light through the crystal as a function of temperature. This allowed a qualitative comparison of the birefringence of as-grown and annealed single crystal fibers to a CZ-grown crystal.

The natural birefringence as a function of temperature of poled single crystals was measured as a function of temperature using the experimental setup in Fig. 1. The light intensity modulation through the sample as a function of temperature was plotted using an X-Y recorder. The temperatures corresponding to transmitted light intensity minima and maxima were digitized to present the data in a normal format. A phase retardation of  $\lambda/2$ , designated by one pass between an intensity minimum and maximum, was used to calculate the relative change in birefringence between room temperature and a higher temperature,  $T$ . Because  $n_0$  is not known, the measured birefringence represents the difference between the total room temperature birefringence and  $n_0$ . A heating rate of  $1^\circ/\text{min}$  was used for all experiments.

The switching response, an important parameter in optical devices, was measured to determine how quickly the crystal responded to an external voltage pulse. The experimental set-up was similar to that shown in Fig. 1, except a Hewlett-Packard (HP) 214B Pulse Generator and Cober Electronics High Power Pulse Generator Model 604A were used to apply external voltage. Both the applied voltage pulse and the transmitted light intensity response were recorded and displayed on a HP digitizing oscilloscope.

The complete experimental setup is shown in Fig. 2. A sweep generator was used to drive the voltage across the crystal. The response from the photodetector and the applied ac field across the sample was simultaneously observed using a HP 54201A digitizing oscilloscope. An accurate measurement of the photodetector output was obtained using a two-phase lock-in amplifier.

The sample holder was capable of axial rotation about three mutually perpendicular axes. The sample was held in place by a spring-loaded prong that also provided electrical connection. The temperature dependence of the birefringence was obtained by placing a small furnace over the sample and the holder.

The electroded sample was placed in the sample holder and poled at room temperature with an 11-kV/cm field for 30 min. The light intensity incident on the photodetector was recorded as a function of applied voltage and the transverse electro-optic coefficients and halfwave voltages of un-

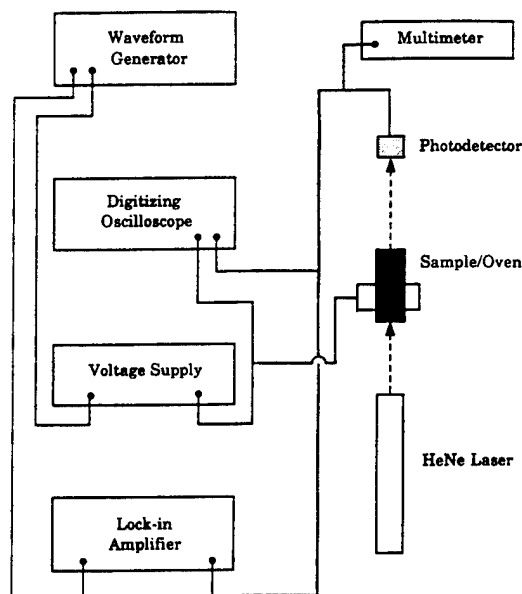


FIG. 2. Schematic drawing of the complete experimental setup used to make the electro-optic measurements.

doped and cerium-doped SBN61 single-crystal fibers were measured.

## B. Sample preparation

The undoped and 0.034 at.% cerium-doped SBN61 single-crystals fibers were grown by the LHPG technique. The cerium content was determined by flame emission spectroscopy. The feedrods were cut from a large sintered ceramic pellet and growth of the single crystals was from an *c*-axis oriented single-crystal seed. The single-crystal fibers were grown at a pull/feed ratio of 60/30 mm/h and the resulting 600- $\mu\text{m}$ -diam crystal was transparent and pink in color. Subsequent growth runs using a single-crystal fiber as a feedrod were possible, enabling further reduction in the crystal diameter. These crystals were typically 300–400  $\mu\text{m}$  in diameter, Fig. 3. The crystals were clear, and using an optical microscope, no compositional striations were observed at magnifications up to 1000 $\times$ . Typi-

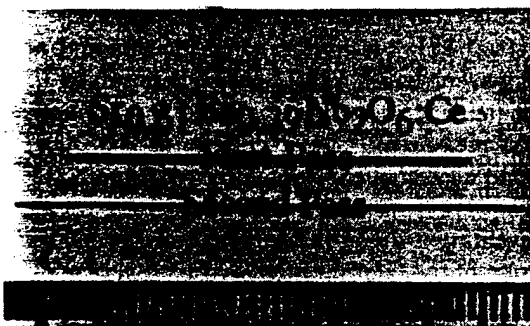


FIG. 3. Photograph of cerium-doped SBN61 single-crystal fibers grown by the laser-heated pedestal growth technique. The first pass crystal was grown from a ceramic feedrod and the second pass crystal was grown from a single-crystal fiber. Each division equals 1 mm.

TABLE I. Transverse electro-optic coefficients ( $r_c$ ) and normalized halfwave voltages ( $[E^*I]_{\lambda/2}$ ) of SBN61 single-crystal fibers at  $\lambda = 633$  nm.  $l$  = optical path length,  $t$  = electrode separation distance. Measurement error  $\sim 20\%$ .

Composition	$l$ ( $10^{-3}$ m)	$t$ ( $10^{-3}$ m)	$r_c$ ( $10^{-12}$ V/m)		$[E^*I]_{\lambda/2}$ (V)	
SBN61 (Czochralski; annealed)	54.7	61.3	304	305	175	166
			204 <sup>a</sup>		170 <sup>b</sup>	
SBN61 (single-crystal fiber; annealed)	0.375	0.86	307	307	174	174
SBN61:Ce (single-crystal fiber; as-grown)	0.435	0.61	138	164	362	378
SBN61:Ce (single-crystal fiber; annealed)	0.40	0.78	146	146	363	366

<sup>a</sup>Reference 10.

<sup>b</sup>Reference 30.

cally 4–6 W of power was sufficient to melt a 0.75-mm-square ceramic rod. Further details concerning the growth of the SBN61 single-crystal fibers will be presented in the literature.<sup>25</sup>

The SBN61 samples were taken from 600- $\mu$ m-diam single-crystal fibers. The cerium-doped samples were cut from adjacent areas on the fiber. Back-reflection x-ray Laue was used to orient the  $a$  axes and  $c$  axis. The samples were sized with 5- $\mu$ m alumina paste and then diamond polished, and were typically  $400 \times 300 \times 700$   $\mu$ m in size. The optical path was parallel to the smallest dimension and the modulating voltage was applied along the longest dimension. The as-grown sample was heated to 200 °C to relieve any induced polishing strains, and the annealed samples were held at 1000 °C for 4 h and slowly cooled. The 200 °C heat treatment was far below the temperature where cation order/disorder was observed.<sup>19</sup> The samples were electroded with air-dried silver paint.

The CZ-grown crystal was previously used to study the effect of cation order and disorder on the dielectric and pyroelectric properties of SBN61.<sup>19</sup> The crystal was  $54.7$  mm  $\times$   $61.3$  mm  $\times$   $52.7$  mm and all six sides were diamond polished. Before measurements were taken on the sample, it was annealed at 1000 °C for 3 h and slowly cooled. The crystal was clear, transparent and free of striations.

### III. RESULTS AND DISCUSSION

Using the calculations described earlier, the unclamped ( $< 1$  kHz) transverse  $r_c$  coefficients and normalized halfwave voltages,  $[E^*I]_{\lambda/2}$ , were determined (Table I). Measurements were taken at two different frequencies; the first measurement was typically at 200–300 Hz and the second measurement was between 600 and 800 Hz. The crystals were easily depoled at moderate voltages, thereby preventing a direct measurement of the halfwave voltage. A plot of the birefringence as a function of applied electric field resulted in a linear relationship, with the birefringence going to zero at zero applied voltage (Fig. 4).

The  $r_c$  coefficients of the annealed undoped single-crystal fiber and CZ-grown SBN61 crystals were in close agreement. The quality of the CZ-grown crystal was very good. No compositional striations were observed, but the signal

tended to drift during the measurement. This signal instability was attributed to the large crystal size, where the increase in the natural birefringence modulation was due to the longer optical path length (54.7 mm) and the effect temperature fluctuations had on the birefringence, Eq. (6). The natural birefringence has been shown to be very sensitive to small ( $< 1$  °C) changes in temperature, where complete modulation of the transmitted light occurred within 2–3 °C.<sup>23</sup>

The addition of cerium reduced the  $r_c$  coefficient of the single-crystal fibers to approximately one half that of the undoped crystal. This was observed in both as-grown and annealed single-crystal fibers. Frequency dispersion in both the  $r_c$  coefficient and halfwave voltage was observed in the as-grown cerium-doped single-crystal fiber, which was not present in the annealed fiber. This instability was attributed to the high strain state and cation disorder in the as-grown fibers caused by the rapid growth rates present in the LHPG technique. This has also been observed in the dielectric properties of annealed and as-grown single crystals.<sup>26</sup>

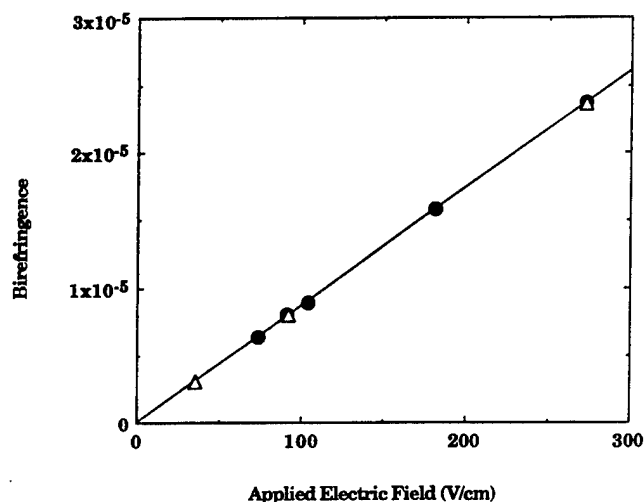


FIG. 4. Birefringence vs applied electric field of an annealed cerium-doped SBN61 single crystal. The measurements were taken at 263 Hz (●) and at 662 Hz (△).

TABLE II. Calculated  $g'$  coefficients of cerium-doped and undoped SBN61 single-crystal fibers ( $\lambda = 633$  nm).  $K_c$  = room temperature dielectric constant (1 kHz),  $n_c$  = refractive index (633 nm),  $V_\pi$  = halfwave voltage,  $P$  = room-temperature polarization,  $g'_p$  = perovskite  $g$  coefficient,  $g'_{tb}$  = tungsten bronze  $g$  coefficient.

	$l$ ( $10^{-3}$ m)	$t$ ( $10^{-3}$ m)	$K_c$	$n_c$	$V_\pi$ (V)	$P$ (C/m <sup>2</sup> )	$g'_p$ (m <sup>4</sup> /C <sup>2</sup> )	$g'_{tb}$
SBN61	0.375	0.86	2100 <sup>a</sup>	2.28 <sup>b</sup>	87	0.25 <sup>a</sup>	0.09	0.08
SBN61:Ce	0.40	0.78	1070 <sup>a</sup>	2.26 <sup>c</sup>	181	0.24 <sup>a</sup>	0.07	0.06
SBN61:Ce (Czochralski)			1480					
SBN61 (Czochralski)							0.12 <sup>d</sup>	0.10 <sup>e</sup>

<sup>a</sup>Reference 26.

<sup>b</sup>Reference 35.

<sup>c</sup>Calculated from G. L. Wood, W. W. Clark, M. J. Miller, E. J. Sharp, G. J. Salamo, and R. R. Neurgaonkar, IEEE J. Quantum Electron. QE-23, 2126 (1987).

<sup>d</sup>Calculated from Ref. 33.

<sup>e</sup>Reference 33.

An accurate measurement of the true  $r_{13}$  and  $r_{33}$  coefficients were made using a Mach-Zender interferometric technique operating at modulating frequencies below acoustic resonances.<sup>10</sup> This technique allows separation of the true electro-optic coefficients from piezoelectric contributions to the measured coefficients. A piezoelectric  $d_{23}$  constant of  $25 \times 10^{-12}$  V/m was reported for the SBN61 single crystal. The piezoelectric contribution to the  $r$  coefficients was calculated, and the effect was found to be small compared to the error in the  $r_{13}$  and  $r_{33}$  coefficients.

Due to the dispersion in the refractive indices, the  $r_{ij}$  coefficients at 514 nm are approximately 10% lower than the refractive indices at 633 nm. Taking the dispersion and the reported error in the individual coefficients into account, the  $r_c$  coefficient at 633 nm was calculated to be  $204 \pm 28 \times 10^{-12}$  m/V.<sup>10</sup> The error in the  $r_c$  coefficient of the undoped SBN61 CZ-grown crystal measured by the Senarmont compensator method was estimated to be 20% or an  $r_c$  of  $300 \pm 60 \times 10^{-12}$  m/V. The total measured  $r_c$  coefficient is in fair agreement with the adjusted  $r_c$  coefficient in the literature.<sup>10</sup>

The reduction in the  $r_c$  coefficient with cerium doping seemed to contradict the enhancement in the photorefractive properties reported in cerium-doped SBN61.<sup>27</sup> The coordination of the cerium ion in the SBN octahedra framework may affect the photorefractive and electro-optic properties. Cerium in twelve coordination is reported to be pink in color, and in nine coordination it is reported to be yellow-green in color.<sup>28</sup> The effect the cerium coordination has on the electro-optic properties has not been systematically investigated, although some work has been reported.<sup>28,29</sup>

The halfwave voltages of the single crystals were calculated using the procedure described earlier; Table I. The CZ-grown crystal exhibited some frequency dispersion but this was most likely caused by instability in the phase modulation as observed in the  $r_c$  coefficient experiment. The bulk and single-crystal fiber SBN61 were good agreement with each other. The halfwave voltages of the as-grown and annealed cerium-doped SBN61 single-crystal fibers were also in good agreement with each other, and again

frequency dispersion was observed in the as-grown single crystal. There was a large increase in the halfwave voltage with the addition of cerium. The reason for the larger halfwave voltages is not clear nor has it been reported in the literature. The halfwave voltage has been reported to be dependent upon the domain state of the crystal.<sup>30</sup> Polydomain undoped crystals reportedly had a normalized halfwave voltage of 680 V, four times greater than the single domain value of 170 V, at 633 nm. The single-domain value was in good agreement with the poled SBN61 samples measured in this work.

The quadratic electro-optic  $g$  coefficients were calculated following the literature<sup>31,32</sup> as a check of the  $r_c$  and halfwave voltage measurement. It has been shown that the  $g$  coefficients are constant for nonlead-containing oxygen octahedra ferroelectrics<sup>21</sup> and were calculated for annealed SBN61 and SBN61:Ce single-crystal fibers. From Eq. (3), the transverse  $r_c$  coefficient is a function of both  $r_{33}$  and  $r_{13}$  coefficients, where they can be expressed as a function of the quadratic electro-optic coefficients,  $g_{11}$  and  $g_{12}$ , respectively<sup>20</sup>

$$r_{33} = \frac{2(g_{11})_p \epsilon_0 (K_c - 1) P_s}{\xi^3}, \quad (8a)$$

$$r_{13} = \frac{2(g_{12})_p \epsilon_0 (K_c - 1) P_s}{\xi^3}. \quad (8b)$$

Combining these terms together using Eq. 3, the  $r_c$  coefficient can be expressed in terms of both  $g_{11}$  and  $g_{12}$  coefficients, and allows  $g'_p$ , where  $g'_p = (g_{11})_p - (g_{12})_p$ , to be expressed in terms of experimentally measured quantities.

For the light propagating along the  $a$  axis and the modulating voltage applied along the  $c$  axis, the  $g$  coefficients,  $g'_p$ , were calculated using the relation<sup>32</sup>

$$g'_p = (g_{11})_p - (g_{12})_p = \frac{\lambda t \xi^3}{2 n_3^3 l \epsilon_0 V_\pi K_3 P}, \quad (9)$$

where  $g_p$  is the  $g$  coefficient of the perovskite structure,  $\xi$  is the packing factor, and the other variables are defined in Table II. The packing factor is used to describe the rela-

tionship between the  $g$  coefficient of the complex oxygen octahedra crystal to the  $g$  coefficient of the perovskite crystal

$$\xi^3 = \frac{g_{\text{perovskite}}}{g_{\text{tungsten bronze}}}, \quad (10)$$

and  $\xi$  for the tungsten bronze structure was taken from the literature to be 1.06.<sup>31</sup>

Using the halfwave voltage and measured room-temperature dielectric constant and polarization, the calculated  $g$  coefficients resulted in values close to the literature value of  $0.10 \text{ m}^4/\text{C}^2$  for the tungsten bronze structure,<sup>33</sup> Table II. The disagreement in the  $g$  coefficient may be associated with the temperature dependence of the natural birefringence on the modulated signal, as discussed earlier. The  $g$  coefficient of the annealed cerium-doped fiber resulted in a slightly lower  $g$  coefficient. A decrease of approximately 50% in the dielectric constant was also observed in the cerium-doped single-crystal fiber. Since both the dielectric constant and  $r$  coefficients of oxygen octahedra ferroelectric materials are closely related via a polarization-optic mechanism,<sup>21</sup> the large decrease in the  $r_c$  coefficient with cerium doping can be considered to be real. The dielectric constant and polarization of a CZ-grown cerium-doped SBN61 single crystal was measured at room temperature at 1 kHz. The dielectric constant of this crystal decreased from the undoped CZ-grown crystal. The change in the electro-optic properties with cerium doping appears to be independent of growth technique, since the cerium had the same effect on crystals grown by the LHPG technique. Further work is ongoing into the electro-optic of the CZ-grown cerium-doped crystal to enable a detailed comparison of the two CZ-grown crystals. The origins of this behavior is not known but it appears that the cerium is reducing the field induced polarization.

The temperature dependence of the birefringence for all samples are shown in Figs. 5–7. The birefringence of the annealed, undoped, SBN61 single-crystal fiber and the CZ-grown SBN61 crystal are shown in Fig. 5. The birefringence of the single-crystal fiber is similar to the CZ-grown crystal. The general behavior of the birefringence agreed with previously reported results, where the nonlinearity in birefringence above the transition temperature was observed. Unfortunately, measurements to higher temperatures where linear behavior has been reported was not possible.<sup>34</sup> Thermal hysteresis of the birefringence during temperature cycling, previously reported in SBN50,<sup>7</sup> was not observed in either crystal. The transition temperature, approximated by the fastest change in birefringence, of the single-crystal fiber was  $68^\circ\text{C}$ , and  $86^\circ\text{C}$  for the CZ-grown crystal. The difference in transition temperatures was due to compositional differences between the two crystals, since it is known that the transition temperature is very sensitive to compositional variations.<sup>8</sup> The composition of the single-crystal fiber did not vary along the length of the fiber, as shown by transition temperature measurements as a function of position along the fiber.<sup>26</sup>

The difference in the magnitude of the birefringence between the CZ-grown crystal and the single-crystal fiber

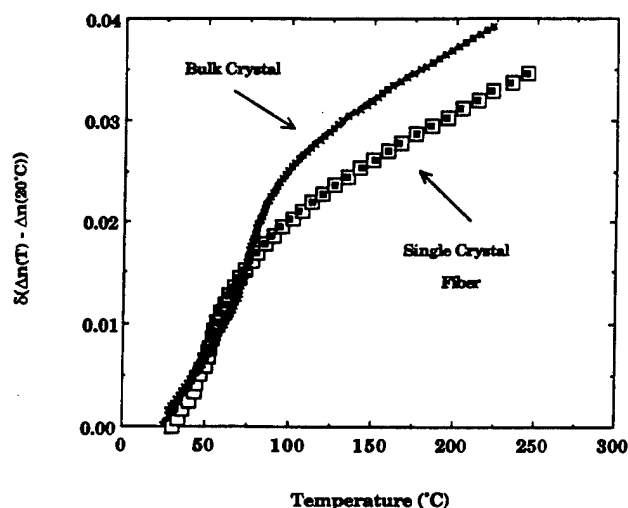


FIG. 5. Birefringence vs temperature of an annealed undoped SBN 61 single-crystal fiber and Czochralski-grown single crystal,  $\lambda = 633 \text{ nm}$ . Measurement on heating of the single-crystal fiber is indicated by an open marker and on cooling by a filled marker. The birefringence of the bulk crystal did not change with heating or cooling.

was due the size difference of the two crystals, Table I. From Eq. (5), the change in the phase retardation,  $\Gamma(\omega)$ , is dependent upon the optical path length,  $L$ . The longer optical path length of the CZ-grown crystal resulted in greater interaction of the crystal with the transmitted light. Due to the qualitative nature of this experiment, a comparison between the birefringence of the CZ-grown and LHPG-grown crystals cannot be drawn. An accurate comparison would require separation of the various contributions to the total birefringence.

The temperature dependence of the birefringence of the cerium-doped as-grown and annealed SBN61 single-crystal fibers are shown in Figs. 6 and 7, respectively. The general shape of the curves agreed with the literature and

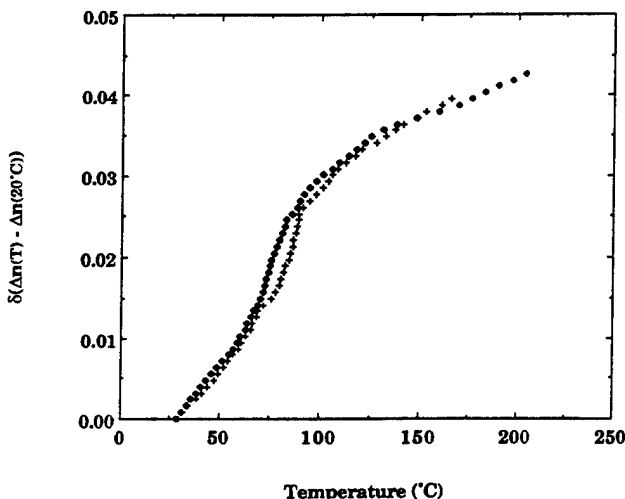


FIG. 6. Birefringence vs temperature of an as-grown cerium-doped SBN61 single-crystal fiber,  $\lambda = 633 \text{ nm}$ . Measurement on heating indicated by a cross marker and on cooling by a filled diamond marker.

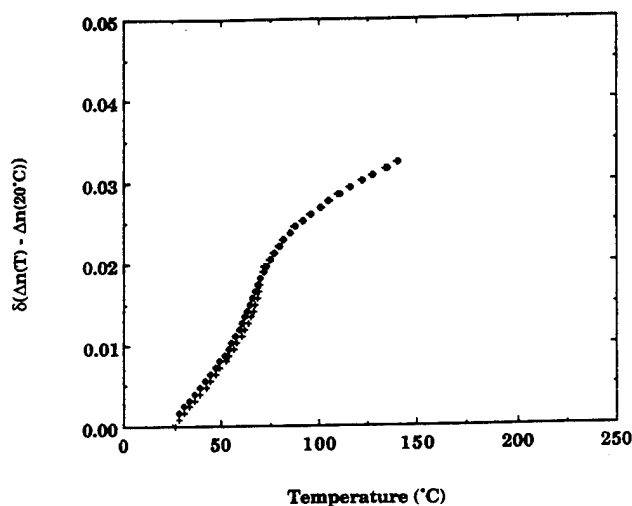


FIG. 7. Birefringence vs temperature of an annealed cerium-doped SBN61 single-crystal fiber,  $\lambda = 633$  nm. Measurement on heating indicated by a cross marker and on cooling by a filled diamond marker.

the measured undoped single crystals.<sup>34</sup> The as-grown sample exhibited thermal hysteresis in the birefringence, which was not observed in the annealed crystal. The as-grown crystal also exhibited a larger birefringence than the annealed crystal, and irregular variations in the birefringence at temperatures above 150 °C. Both were attributed to the strain and cation disorder in the crystal caused by the rapid growth rate. The phase transition temperature was also higher in the as-grown sample which agrees with the dielectric and pyroelectric properties.<sup>26</sup> This is another indication that the single crystal fibers require annealing to stabilize the electric and optical properties.

The switching response of the annealed SBN61:Ce single-crystal fiber (bottom) was measured with an applied voltage pulse of 100 V, 48  $\mu\text{s}$  in duration (top), Fig. 8. The analyzer was set to the minimum transmittance to observe the largest change in the output intensity. The crystal easily followed the applied voltage, and the ringing due to the unclamped piezoelectric effect quickly decays after 8  $\mu\text{s}$ . This was similar to the reported behavior in the literature.<sup>35</sup>

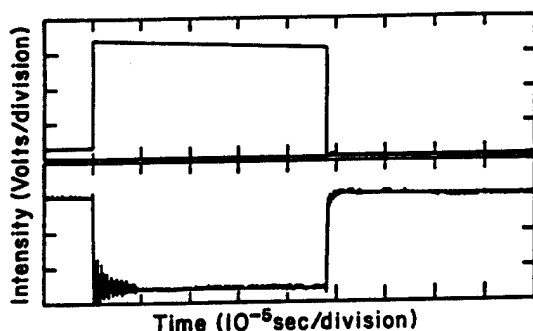


FIG. 8. Reproduction of the switching response of an unclamped, annealed SBN61 cerium-doped single-crystal fiber (bottom) to an applied 100-V 48  $\mu\text{s}$  pulse (top).

## IV. CONCLUSIONS

The  $r_c$  coefficients of the undoped SBN 61 Czochralski-grown crystal and single-crystal fiber were in good agreement with each other, indicating that the linear electro-optic coefficients were not affected by the rapid growth rates found in the LHPG technique.

The addition of cerium reduced the  $r_c$  coefficients and increased the halfwave voltages relative to the undoped crystals. This is in agreement with the decrease in the dielectric constant observed in cerium-doped single crystals. There was no change in the  $r_c$  coefficients after annealing.

Frequency dispersion in the  $r_c$  coefficients and half-wave voltages of the as-grown single-crystal fiber was most likely caused by strain and cation disorder induced by the rapid growth rates. Post-growth annealing eliminated the frequency dispersion and indicated that annealing is a necessary step to stabilize the crystal before application of these single-crystal fibers in an electronic or optical device.

The quadratic  $g$  coefficients were calculated using the measured halfwave voltages, dielectric constant, and polarization. The  $g$  coefficient of the undoped SBN61 single-crystal fiber ( $g'_{ib} = 0.08$ ) was in better agreement with the literature value ( $g'_{ib} = 0.10$ ) than the cerium-doped SBN61 single-crystal fiber ( $g'_{ib} = 0.06$ ).

The dependence of the birefringence with temperature of the single-crystal fiber was found to agree with the literature. The as-grown cerium-doped single-crystal fiber exhibited thermal hysteresis which was eliminated upon annealing. The response of the annealed single-crystal fiber to an applied voltage displayed ringing at the voltage onset and decayed after 8  $\mu\text{s}$ .

## ACKNOWLEDGMENTS

The authors would like to thank Dr. R. Guo for insightful discussions and Dr. L. E. Cross and Dr. S. J. Jang for their support.

<sup>1</sup> R. S. Feigelson, *Crystal Growth of Electronic Materials*, edited by E. Kaldis (Elsevier, New York, 1985), Chap. 11.

<sup>2</sup> L. G. DeShazer and S. C. Rand, *Proc. SPIE* **618**, 95 (1987).

<sup>3</sup> Y. S. Luh, R. S. Feigelson, M. M. Fejer, and R. L. Byer, *J. Cryst. Growth* **78**, 135 (1986).

<sup>4</sup> M. Saifi, B. Dubois, E. M. Vogel, and F. A. Thiel, *J. Mater. Res.* **1**, 452 (1986).

<sup>5</sup> L. Hesselink and S. Redfield, *Opt. Lett.* **13**, 877 (1988).

<sup>6</sup> P. V. Lenzo, E. G. Spencer, and A. A. Ballman, *Appl. Phys. Lett.* **11**, 23 (1967).

<sup>7</sup> E. L. Venturini, E. G. Spencer, P. V. Lenzo, and A. A. Ballman, *J. Appl. Phys.* **39**, 343 (1968).

<sup>8</sup> M. H. Francombe, *Acta Crystallogr.* **13**, 131 (1960).

<sup>9</sup> K. Megumi, N. Nagatsuma, Y. Kashiwada, and Y. Furuhashi, *J. Mater. Sci.* **11**, 1583 (1976).

<sup>10</sup> S. Ducharme, J. Feinberg, and R. R. Neurgaonkar, *IEEE J. Quantum Electron.* **QE-23**, 2116 (1987).

<sup>11</sup> A. J. Fox, *J. Appl. Phys.* **44**, 254 (1973).

<sup>12</sup> M. Ingold and P. Gunter, *Proc. SPIE* **1018**, 12 (1988).

<sup>13</sup> V. Afanasjev, S. Korpela, and T. Tuomi, *Ferroelect.* **65**, 175 (1985).

<sup>14</sup> R. R. Neurgaonkar, W. K. Cory, J. R. Oliver, E. J. Sharp, M. J. Miller, W. W. Clark, G. L. Wood, and G. L. Salamo, *Mater. Res. Bull.* **24**, 589 (1989).

<sup>15</sup> K. Megumi, H. Kozuka, M. Kobayashi, and Y. Furuhashi, *Appl. Phys. Lett.* **30**, 631 (1977).

- <sup>16</sup>S. T. Liu, R. B. Maciolek, J. D. Zook, and B. Rajagopalan, *Ferroelect.* **87**, 265 (1988).
- <sup>17</sup>J. K. Yamamoto and A. S. Bhalla, *Mater. Res. Bull.* **24**, 761 (1989).
- <sup>18</sup>M. E. Lines and A. M. Glass, *Principles and Applications of Ferroelectrics and Related Materials* (Clarendon, Oxford, 1977).
- <sup>19</sup>R. Guo, A. S. Bhalla, G. Burns, and F. H. Dacol, *Ferroelect.* **93**, 397 (1989).
- <sup>20</sup>M. DiDomenico and S. H. Wemple, *J. Appl. Phys.* **40**, 720 (1969).
- <sup>21</sup>P. Gunter, *Ferroelect.* **75**, 5 (1987).
- <sup>22</sup>J. F. Nye, *Physical Properties of Crystals* (Clarendon, Oxford, 1957).
- <sup>23</sup>M. Aillerie, M. D. Fontana, F. Abdi, C. Carabatos-Nedelec, and N. Theofanous, *Proc. SPIE* **1018**, 94 (1988).
- <sup>24</sup>P. Gunter, *Opt. Commun.* **11**, 285 (1974).
- <sup>25</sup>J. K. Yamamoto, S. A. Markgraf, and A. S. Bhalla (unpublished).
- <sup>26</sup>J. K. Yamamoto and A. S. Bhalla (unpublished).
- <sup>27</sup>G. A. Rakujlic, A. Yariv, and R. R. Neurgaonkar, *Proc. SPIE* **613**, 110 (1986).
- <sup>28</sup>M. D. Ewbank, R. R. Neurgaonkar, W. K. Cory, and J. Feinberg, *J. Appl. Phys.* **62**, 374 (1987).
- <sup>29</sup>E. Kratzig and O. F. Schirmer, *Photorefractive Materials and Their Applications, I. Fundamental Phenomena* (Springer, New York, 1988).
- <sup>30</sup>B. N. Zakharov, A. K. Zeinaly, N. M. Lebedeva, A. M. Mamedov, and A. R. Mordukhaev, *Sov. Phys. Solid State* **22**, 161 (1980).
- <sup>31</sup>S. H. Wemple and M. DiDomenico, *J. Appl. Phys.* **40**, 735 (1969).
- <sup>32</sup>L. G. Van Uitert, J. J. Rubin, W. H. Grodkiewicz, and W. A. Bonner, *Mater. Res. Bull.* **4**, 67 (1969).
- <sup>33</sup>G. Burns and F. H. Dacol, *Phys. Rev. B* **30**, 4012 (1984).
- <sup>34</sup>A. S. Bhalla, R. Guo, L. E. Cross, G. Burns, F. H. Dacol, and R. R. Neurgaonkar, *Phys. Rev. B* **36**, 2030 (1987).
- <sup>35</sup>S. Sakamoto and T. Yazaki, *Appl. Phys. Lett.* **22**, 429 (1973).

**Appendix 3.**

**" $\text{Sr}_x\text{Ba}_{1-x}\text{Nb}_2\text{O}_6$  Single Crystal Fibers: Dependence of Crystal Quality on Growth Parameters," *J. Cryst. Growth.* 123, 423-435 (1992).**

**J.K. Yamamoto  
S.A. Markgraf, and  
A.S. Bhalla**

## $\text{Sr}_x\text{Ba}_{1-x}\text{Nb}_2\text{O}_6$ single crystal fibers: dependence of crystal quality on growth parameters

Joyce K. Yamamoto<sup>1,2</sup>, Steven A. Markgraf<sup>3</sup> and Amar S. Bhalla

*Materials Research Laboratory, Pennsylvania State University, University Park, Pennsylvania 16802, USA*

Received 26 November 1991; manuscript received in final form 15 February 1992

The laser-heated pedestal growth technique was used to grow undoped and cerium-doped strontium barium niobate,  $\text{Sr}_x\text{Ba}_{1-x}\text{Nb}_2\text{O}_6$ , single crystal fibers. Crystals approximately 400–600  $\mu\text{m}$  in diameter and 30–40 mm in length, of compositions extending across the solid-solution range,  $0.25 < x < 0.75$ , were grown. The pull/feed rates were varied, at a constant ratio of 2-to-1, and the effect on the resulting crystal quality and composition of cerium-doped  $\text{Sr}_{0.61}\text{Ba}_{0.39}\text{Nb}_2\text{O}_6$  was studied. Crystal quality was evaluated through the observation of dislocation patterns produced in an acid-etch technique, and the compositional homogeneity was monitored by the change in the ferroelectric transition temperature as a function of growth rate and position along the fiber. High quality single crystal fibers were produced at growth rates up to 40 mm/h. The single crystals were compositionally homogeneous and relatively dislocation-free. The freezing and melting interfaces were unusually shaped but similar to that observed in the float zone growth of  $\text{NaNO}_3$ , suggesting that Marangoni convection may be responsible for the distortion observed at the interfaces.

### 1. Introduction

Single crystal fibers are currently receiving attention as potential components in a variety of optical, electrical, and structural applications. The large length-to-diameter ratio is appealing for composite structures; through the selection of the proper composition and crystallographic orientation it may be possible to minimize or maximize a desired physical property along the fiber axis. Many compositions have been grown using the laser-heated pedestal growth (LHPG) technique [1], and these include both oxide and nonoxide materials. In particular,  $\text{Al}_2\text{O}_3$ ,  $\text{LiNbO}_3$ , and  $\text{BaTiO}_3$  have been studied for applications in

laser delivery systems and non linear optical devices [2–4].

The material we chose to grow using the LHPG technique was  $\text{Sr}_x\text{Ba}_{1-x}\text{Nb}_2\text{O}_6$  (SBN). SBN exists as a solid-solution system in the range of  $0.25 < x < 0.75$ , where interest in the optical properties of selected compositions in this system has been fueled by the large electro-optic coefficients and low halfwave voltages. The optical properties of Czochralski-grown  $\text{Sr}_x\text{Ba}_{1-x}\text{Nb}_2\text{O}_6$  single crystals have been extensively investigated, and many of its dielectric, pyroelectric and optical properties have been found to be strongly dependent on composition. The congruently melting composition in this system,  $\text{Sr}_{0.61}\text{Ba}_{0.39}\text{Nb}_2\text{O}_6$  (SBN61), yields the best quality crystals and therefore has received the most attention [5–8].

The photorefractive properties of cerium-doped  $\text{Sr}_{0.61}\text{Ba}_{0.39}\text{Nb}_2\text{O}_6$  (SBN61:Ce) single crystal fibers have been reported, where its application as a holographic storage media was evaluated [9]. It has been shown that post-growth annealing of the single crystal fibers is necessary

<sup>1</sup> Author to whom correspondence should be addressed.

<sup>2</sup> Present address: Corporate Research and Development Center, Mitsui Mining and Smelting Co. Ltd., 1333-2 Haraichi, Ageo-shi, Saitama 362, Japan.

<sup>3</sup> Present address: Magnetic and Electronic Materials Research Laboratory, Hitachi Metals Ltd., 5200 Mikajiri, Kumagaya-shi, Saitama 360, Japan.

to eliminate instabilities in the optical properties and to improve the transverse electro-optic coefficients [10]. A preliminary study of the LHPG growth of SBN determined that the preferred growth orientation was along the  $c$ -axis [11]. Clear distinct X-ray diffraction spots indicated that the crystal was not heavily strained, and compositional striations perpendicular to the growth direction were not observed.

The application of single crystal fibers in miniature lasers, and other electrical and optical devices, requires a high degree of crystalline perfection in order to reduce scattering and to increase efficiencies. Since SBN is not congruently melting and previous studies have focused on congruently melting materials, the feasibility of growth of the highly incongruently melting compositions and the effect the rapid growth rates may have on various crystal properties is of interest. Therefore, it is important to study how different growth parameters affect the crystalline fiber. In this work several parameters were investigated; the effect of ceramic versus single crystal feed material, growth rate, and interface shape on the crystal quality and compositional homogeneity of the resulting single crystal fibers were studied.

## 2. Experimental procedure

### 2.1. Equipment

The LHPG equipment was similar to that described in the literature [1]. The power source was a water cooled, tunable  $CO_2$  50 W laser. The circular laser radiation,  $TEM_{00}$ , was transformed into an annulus by a reflexicon [12]. The annulus was directed onto a parabolic mirror, which focused the radiation back to its focal point, forming the hot zone. The pulling heads were high precision 5-phase microstepper motors, with a single step increment of 25  $\mu m$ . The quoted accuracy of the microstepper motors was 0.1% at 999.9 mm/h. The growth chamber was a stainless steel vacuum chamber, which enclosed the reflexicon and the internal optics to minimize air current disturbances, and all growth was in air.

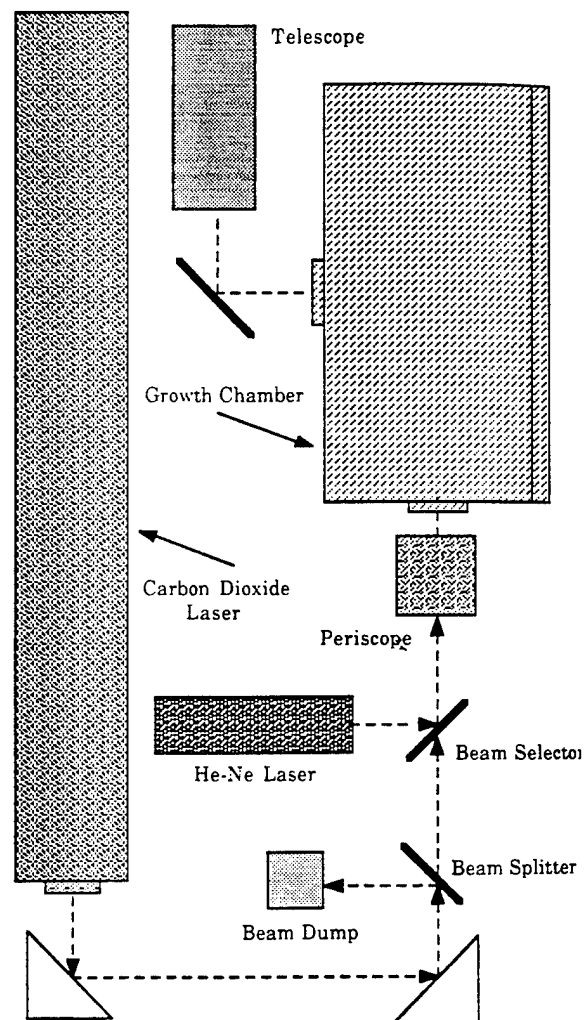


Fig. 1. Schematic diagram of the laser heated pedestal growth station.

The alignment, seeding and growth was visually imaged outside the growth chamber by a short focal length telescope, which was in line with a CCD camera. A schematic diagram of the LHPG station is shown in fig. 1.

### 2.2. Preform preparation

The preforms, or starting feedrods, were all prepared in the same manner using the mixed-oxide method. The purity of the starting powders varied between 99.995% to 99.999%. Therefore, to achieve maximum benefit of the high-purity powders, care was taken in the processing proce-

ture to minimize contamination. The starting powders were ball-milled in anhydrous ethanol for 12 h and dried, and the powder mixture was firmly packed into a platinum crucible. The crucible was covered and placed into a molybdenum disilicide furnace for calcination. The calcining temperatures varied between 1200 and 1425°C.

After calcining, the powder was ground in a Diamonite mortar and pestle, and sieved through a 110  $\mu\text{m}$  polyethylene mesh. Phase confirmation was checked by X-ray powder diffraction. If the powder was single phase, processing continued to the next step. If further calcination was necessary, the previous procedure was repeated until a fully reacted single phase powder was produced.

A nonaqueous binder (DuPont 5200 MLC) was added at 6 wt% to the single phase powder, mixed, ground, and sieved again through a 110  $\mu\text{m}$  polyethylene mesh. The sieved powder was pressed into a pellet 3.5 cm in diameter and 1 cm in thickness. The pellet was then sintered in barium zirconate sand to prevent cracking and deformation in the sample.

The sintered pellet was sliced into wafers approximately 2 mm thick and the surface of the wafer was sanded flat using a diamond surface sander. The sanding also removed the outer surfaces of the pellet which had been in contact with the barium zirconate powder. The final thickness of the wafer was usually 0.5 to 0.75 mm, and corresponded to the preform dimensions. The thin wafers were cut into square rods using a diamond-embedded wafering saw, and subsequently thoroughly soaked in acetone to remove cutting oils and other organic contaminants. The preforms were approximately 2 cm in length.

### 2.3. Growth

The undoped SBN61 single crystal fibers were grown from a ceramic feedrod using spontaneous nucleation onto another ceramic feedrod. The cerium-doped SBN61 (SBN61:Ce) crystals were grown from a SBN61:Ce *c*-axis oriented seed, and the feedrod was either a ceramic or a previously grown single crystal (first-pass crystal). Since the use of a dislocation-free seed, and careful polishing and etching have been reported to pro-

duce high-quality SBN crystals [13,14], care was taken in the preparation of the seed crystals. The production of a suitable SBN61:Ce seed crystal required a two-step process to ensure correct orientation and compositional homogeneity. The first step was growth from a cerium-doped ceramic feedrod to an oriented undoped SBN61 single crystal. The lower end of this cerium-doped crystal, opposite the undoped seed, was oriented by back-reflection X-ray Laue and polished flat and perpendicular to the long axis of the crystal. This crystal then became the oriented seed for the second growth of a new crystal from a cerium-doped ceramic feedrod. The crystal quality of this second crystal was checked by acid etching, and the orientation of the *c*-axis was approximately  $1^\circ \pm 0.5^\circ$  off the fiber axis. This second fiber served as the seed for all the crystals grown in this experiment. All crystal growth was in the upward direction. The cerium content of the single crystal fibers was 0.034 at% as determined by flame emission spectroscopy, and major impurities were not detected.

### 2.4. Characterization

The effect the growth rate had on the composition and crystal quality was investigated in cerium-doped SBN61 single crystal fibers. The Curie temperature,  $T_C$ , has been shown to be very sensitive to compositional changes that may have occurred in the growth process [7]. Therefore, the composition of the single crystal fibers was checked by the measurement of the ferroelectric/paraelectric transition temperature. Slices were taken from the single crystal fiber, and both sides were diamond polished flat and perpendicular to the *c*-axis. The samples were 500–600  $\mu\text{m}$  in diameter and 100  $\mu\text{m}$  thick. Gold sputtered electrodes were deposited, and the sample was placed in a sample holder designed for these very small crystals. The capacitance and loss of poled crystals were measured on heating as a function of temperature.  $T_C$  was determined by monitoring the capacitance as a function of temperature, under weak field conditions, and  $T_C$  was taken as the temperature of the capacitance maximum.

Acid etching has been used to reveal structural variations in Czochralski-grown SBN single crystals [15]. Room-temperature hydrofluoric (HF) acid is an excellent etchant for this purpose. Four different etch pits have been reported on oriented *c*-plates: square pyramidal, octagonal pyramidal, square spiral, and square closed terrace pits. These pits were attributed to dislocations based upon two observations: upon further etching the pointed tip remained sharp, and there was a one-to-one correspondence of etch pits on opposite faces of the sample. In this study, the density and distribution of dislocation etch pits, both parallel and perpendicular to the growth axis, were examined. The procedure used to etch the single crystal fibers was similar to the reported technique [15]. Sections were cut from the fiber and diamond polished. Each sample was placed in 40 ml of 50% HF acid for 3–5 h and after rinsing they were photographed in reflected polarized light with an optical microscope.

To study the shape of the LHPG freezing interface, the molten zone was quenched by quickly blocking the laser beam during stable growth. The frozen zone was polished parallel to the growth axis, producing a thin polished plate through the center of the zone, allowing observation of both the melting and freezing interfaces. These polished plates were then observed in transmitted light with an optical microscope.

### 3. Results and discussion

#### 3.1. Crystal growth

In the growth of the undoped and cerium-doped SBN61 compositions, a stable molten zone was easily established. Discussions concerning the shape and stability of LHPG molten zones are presented in the literature [16–19], and for SBN a stable zone required a meniscus angle of less than  $0^\circ$ . A stable SBN molten zone was determined by observing the dislocation etch pit density, produced by acid etching, of crystals grown from molten zones of both negative and positive meniscus angles. The dislocation etch pits were observed on polished faces parallel to the *c*-axis.

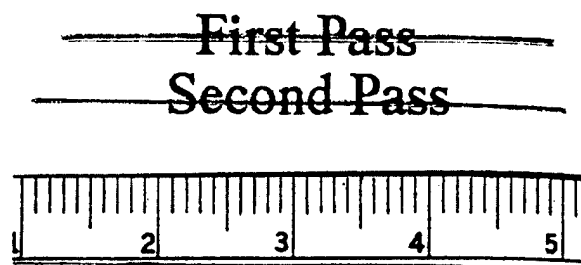


Fig. 2. Photograph of SBN61:Ce single crystal fibers grown by the LHPG technique. "First pass" is growth from a ceramic and "second pass" is growth from a "first pass" single crystal. Each division is 1 mm.

Very few dislocation etch pits were observed in crystals grown from a zone having a negative meniscus angle, in contrast to the high density of etch pits in crystals grown from a molten zone having a positive meniscus angle [16].

The undoped SBN61 single crystals were colorless and free of cracks. The cerium-doped SBN61 single crystals were pink and the color was uniform along the length of the crystal. The diameters of these single crystals were uniform, 600  $\mu\text{m}$ , except for occasional {110} facets that were most likely due to uneven laser energy distribution. Neither the seed nor the feedrod were rotated during growth. Very small surface ridges perpendicular to the growth axis were observed on the surface of the single crystal fibers. Examples of cerium-doped SBN61 single crystal fibers grown using the LHPG equipment are shown in fig. 2.

Compositions farther away from the congruently melting composition, e.g. SBN25 and SBN75, were more difficult to grow and resulted in crystals of inferior crystal quality. These crystals were clear and transparent, inclusions and coring were not observed, but large facets and irregular diameter variations were present.

The final length of the crystal was dependent upon several parameters; the dimensions and density of the feedrod, the diameter reduction ratio, the final diameter of the single crystal fiber and the translation limitations of the equipment. Typically for a 600  $\mu\text{m}$  diameter crystal, using a

feedrod of  $0.5 \text{ mm} \times 0.5 \text{ mm} \times 20 \text{ mm}$ , the length of the grown crystal was 40–45 mm.

### 3.2. Preferred growth orientation

The preferred growth orientation of the SBN61:Ce crystals was determined by spontaneous nucleation using a ceramic feedrod of the same composition as the seed. Growth along the  $c$ -axis, with no exception, occurred regularly and was in agreement with previous studies on LHPG grown undoped SBN61 [10].

Growth of SBN61:Ce using an  $[110]$  oriented seed was investigated to determine if other growth orientations were possible. The  $[110]$  seed was cut from a Czochralski-grown SBN61 crystal. The growth conditions were similar to previous growth runs. Growth along this direction was not possible under these conditions; the material directly below the seed was extensively cracked, and a steady zone was difficult to establish. Recently it has been shown that growth along the  $(110)$  axis is possible, making SBN single crystal fibers more useful in some optical applications [20].

### 3.3. Crystal quality: growth rate dependence of SBN61:Ce

Three sets of growth conditions (table 1) were selected to study the pull/feed rate dependence. The reduction ratio is defined as the ratio between the pull rate to the feed rate. Under steady-state conditions there is a balance between the mass entering and leaving the molten zone; therefore, a constant reduction ratio results in approximately equal crystal diameters for each run. The constant crystal diameter eliminated any contributions that radial temperature gradients, if

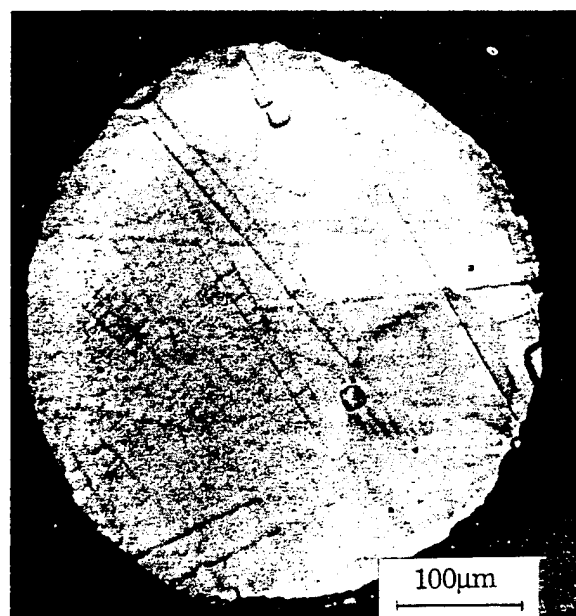


Fig. 3. Dislocation etch-pit pattern of the SBN61:Ce single crystal fiber seed crystal used in the growth rate experiment. Observed face is perpendicular to the  $c$ -axis.

present, may have had on the results, and enabled a better comparison of growth rate effects.

The acid-etched face of the SBN61:Ce seed used in the growth runs is shown in fig. 3. A section was taken perpendicular to the growth axis, and the dislocation etch pits were produced as described earlier. The center of the crystal was dislocation-free, with only two square pyramidal etch pits observed at the periphery of the crystal. In contrast, the etch pattern of a SBN61:Ce single crystal fiber grown from a ceramic feedrod is shown in fig. 4. The sample was removed from the middle of the fiber, where stable growth conditions were present. The central region was dislocation-free, but the outer region had a high concentration of dislocations. The distribution of the dislocations also indicates that the melt disturbances affected primarily the outer regions of the fiber. The melt disturbances caused by air bubbles did affect the crystal quality, and indicated that the density of the initial feedrod played an important role in determining the resulting crystal quality.

From these results, the feedrods used in the following experiment were first densified by grow-

Table 1  
Growth conditions of the SBN61:Ce single crystal fibers

Label	Feed rate (mm/h)	Pull rate (mm/h)	Reduction ratio
B2-19	10	20	2
B2-16	20	40	2
B2-17	40	80	2

ing single crystal fibers, using a ceramic feedrod as a seed, at 60 mm/h pull rate and 30 mm/h feed rate. This yielded single crystal fibers of 40–50 mm in length and 600  $\mu\text{m}$  in diameter. The molten zone was stable except for slight movement in the melting interface caused by bubbles from the ceramic feedrod.

The second pass on each fiber was grown at the specific growth rates shown in table 1. No bubbles were seen, and both interfaces were stationary. The shape and size of the molten zones for the second-pass runs did not vary with growth rate. To examine the crystal quality of the fibers as a function of the growth rate, a section was taken from both ends of each fiber, each grown under stable conditions, and polished perpendicular to the growth axis. Each section was acid etched under identical conditions and observed through an optical microscope in reflected white light.

The etch pits caused by dislocations were clear and distinct, with a clear, well-defined shape. Pits caused by flaws in the polished surface were shallow and diffuse in form [15]. For each section,

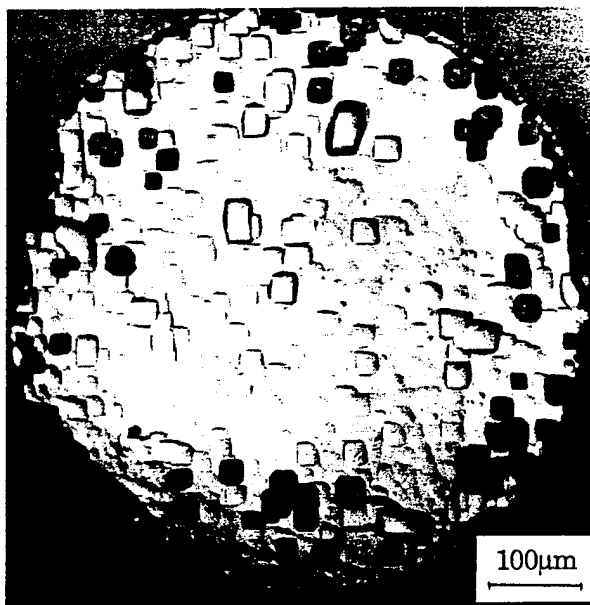


Fig. 4. Dislocation etch-pit pattern of an SBN61:Ce single crystal fiber, grown from a ceramic feedrod (first-pass crystal). Observed face is perpendicular to the  $c$ -axis.

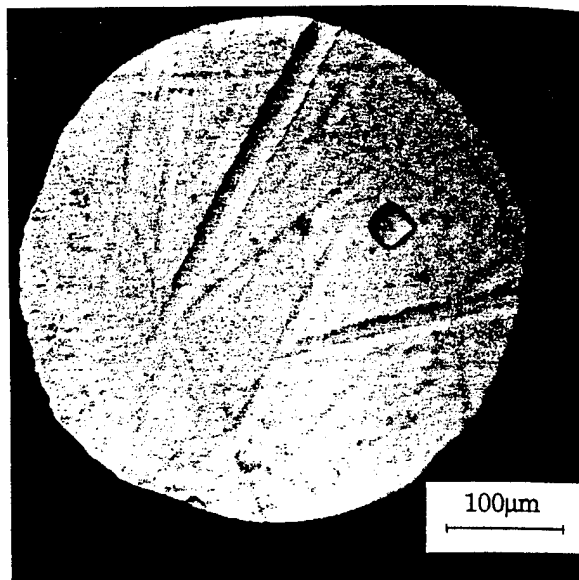


Fig. 5. Dislocation etch-pit pattern of the B2-17 single crystal fiber taken from a section near the end of the fiber (last growth). Observed face is perpendicular to the  $c$ -axis.

the etch-pit patterns were mirror images of the opposite face, further indicating that the well defined pits were due to dislocations extending through the crystal.

The initial section of the fiber was nearest to the seed and the final section was the last growth of the crystal. For all three growth conditions in table 1, the initial sections were more defective than the final sections. A typical etch-pit pattern of a final section is shown in fig. 5. In all etched sections the center of the fibers were clear of dislocations, and any etch pits present were located at the perimeter of the fiber. No dependence was observed between dislocation density and growth rate. Under stable conditions, the number of dislocations decreased with increasing length. Microvoids, observed in alumina single crystal fibers [21], were not observed in SBN single crystal fibers. Crystals grown at 40 mm/h were clear and transparent, indicating that at these rapid growth speeds the melting and freezing interfaces were stable.

From these results it appeared that dislocations were present in the initial growth, but as growth proceeded eventually no dislocations were

observed. To monitor this in more detail, sections along the length of sample B2-17 (table 1) were polished and acid etched. Sections closer to the seed, where unstable growth conditions were present, were etched and found to be highly defective, with etch pits covering the entire surface, fig. 6. This face had a high density of both square and octagonal pyramidal pits, as well as square spiral and closed terrace pits. This was the first time square spiral and closed terrace pits were observed in the single crystal SBN fiber. In Czochralski-grown SBN all four types of etch pits occur with similar frequency [13].

As sections along the length of the fiber were removed and etched, the number of dislocations decreased. This is clearly observed in figs. 5 and 6, showing a clear decrease in the number of dislocation etch pits. This is also depicted in fig. 7, where the number of dislocations on the etched

face is shown as a function of distance from the seed. After approximately 10 mm of growth, the majority of the dislocations were removed (at least at the resolution of our examination).

The type of etch pits observed also changed with increasing growth. Towards the end of unstable growth, the square spiral and closed terrace etch pits were no longer observed, leaving only the pyramidal etch pits. The step heights of the dislocations producing the terrace and spiral dislocations, approximately several microns, were reported to be higher than the dislocations responsible for the pyramidal etch pits [15]. Therefore, it seems that large perturbations in the molten zone, present just after seeding, promoted all four types of dislocations, but as the perturbations decreased and the molten zone stabilized, the larger dislocations were not formed. Eventually the pyramidal etch pits in the center of the fiber were removed when stable growth conditions were established.

The unstable growth region of sample B2-17 (table 1) was polished parallel to the fiber axis and viewed in transmitted polarized light. Compositional striations were observed perpendicular to the growth direction (fig. 8a). They were irregularly spaced and were only present in the center of the fiber. This was in contrast to crystals grown under stable conditions. Compositional striations were not observed in SBN50, SBN61 and SBN75 single crystal fibers produced from stable zones (fig. 8b) [11].

There is one final observation concerning the dislocation distribution in the SBN single crystal fibers. The outer surface of all etched samples had a high dislocation density, regardless of the interior crystal quality (fig. 9). This was to be expected because the outer surface was in a different thermal environment than the rest of the molten zone, promoting dislocation formation. This may become a factor in optical device applications, because the higher dislocation density at the surface will increase light scattering, and may also affect post-growth diffusion rates in cladding procedures. It may also affect attempts to utilize single crystal fibers as substrate materials, where lattice mismatch between the substrate and the film can influence the quality of the second layer.

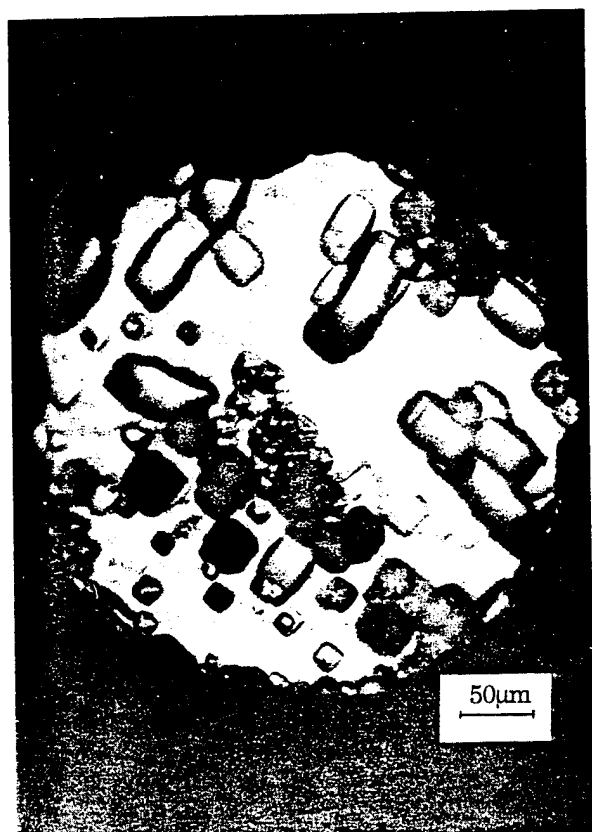


Fig. 6. Dislocation etch-pit patterns of the B2-17 single crystal fiber taken from a section near the seed (first growth). Observed face is perpendicular to the  $c$ -axis.

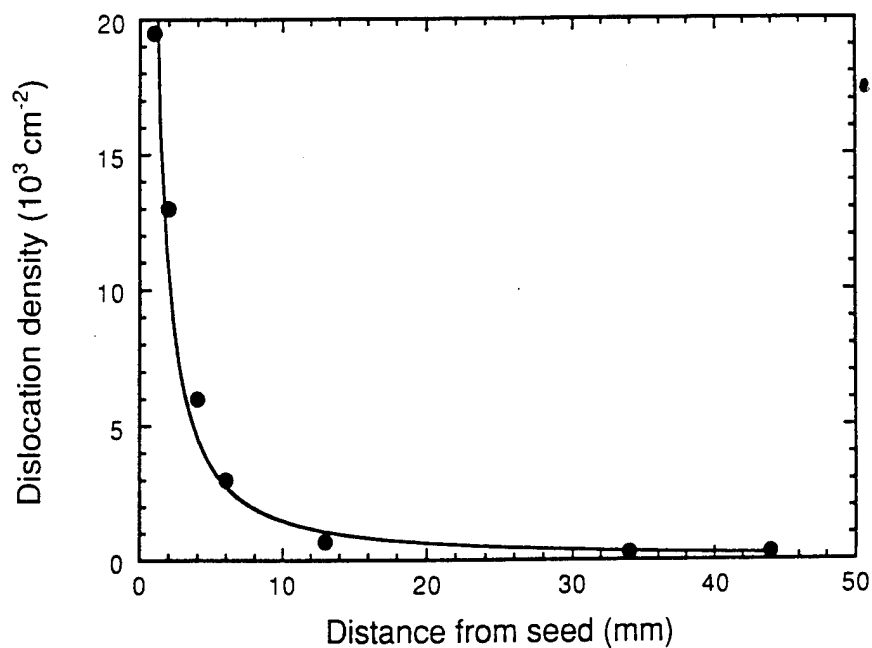


Fig. 7. Dislocation density as a function of growth length along the B2-17 single crystal fiber. The cross-sectional area was assumed to be constant along the fiber.

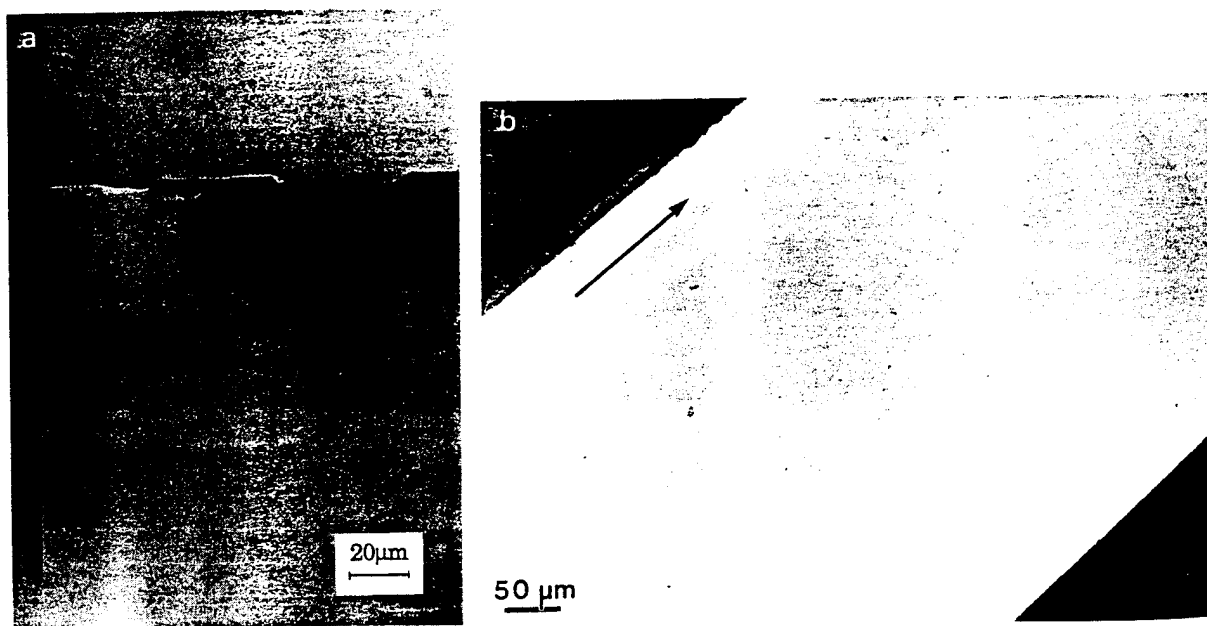


Fig. 8. (a) Compositional striations observed in a single crystal fiber grown under unstable conditions; (b) absence of compositional striations observed in a single crystal fiber grown under stable conditions. Observation was through cross polarized white light, parallel to the growth axis. Arrows denote growth direction.

### 3.4. Growth rate effects on compositional homogeneity

To determine if there was a compositional dependence on the growth rate of the SBN61:Ce single crystal fibers, the dielectric properties were examined. The Curie temperature at the bottom and top of each fiber in table 1 was measured as described earlier, and the results are shown in table 2. Within experimental error, there was no difference in the Curie temperature at each end of the fiber, indicating that the composition of the crystal did not change appreciably as growth progressed. There was a slight increase in the Curie temperature with increasing growth rate, and overall the transition temperatures were higher than Czochralski-grown crystals. The higher transition temperature was due to the increased disorder of the Sr and Ba cations in the

Table 2

Curie temperature of SBN61:Ce single crystal fibers as a function of growth rate and position

Feed/pull rate (mm/h)	$T_C$ at 1 kHz (°C)		$\Delta T_C$ (°C)
	Initial growth	Final growth	
10/20	89.2	91.1	1.9
20/40	90.3	92.0	1.7
40/80	93.8	90.1 *	1.9 *

Experimental error is  $\pm 1\%$  except \* where error is  $\pm 3\%$ .

oxygen octahedra framework as a result of the increased growth rate [16].

### 3.5. Shape of the melting and freezing interfaces

In crystal growth the shape of the freezing interface is important in determining the quality of the grown crystal. The shape of this interface affects the flow patterns and thermal gradients in the zone, which in turn affects the chemical homogeneity and dislocation density of the growing crystal. This has been studied by many investigators, where several parameters were addressed: gravitational forces, small crystal diameters, and simulated zero gravity conditions [22–24]. The results indicated that gravitational effects can be neglected for small geometries and this was experimentally confirmed in the growth of alumina and silicon using the LHPG technique [25]. It was found that for small diameters, zone stability is primarily controlled by the surface tension of the melt. In the growth of SBN by the Czochralski method it was established that by controlling the melt–solid interface, dislocations and compositional striations were eliminated. The desired interface in Czochralski-grown SBN is flat or convex towards the melt [26,27].

Alumina LHPG molten zones have been studied and modeled in the past because it is a well characterized, congruently melting material. Many of the physical parameters necessary to model an SBN zone are unknown, therefore in this section we will detail our empirical observations. The zone formed from crystal-to-crystal growth is shown in fig. 10. Both melting and freezing interfaces were symmetric about the fiber axis and convex to the melt. The melting and



Fig. 9. Dislocation etch pits observed on the outer surface of the SBN61:Ce single crystal fiber.

freezing interface had an area in the center that was flat and perpendicular to the fiber axis. There was also a small dome protruding into the zone at both melting and freezing interfaces. The shape of the interfaces may have been altered, due to zone contraction on cooling, but similar studies on  $\text{LaB}_6$  single crystal fiber zones did not display the curvature observed in the SBN frozen zones [28].

Higher magnification photographs of the melting and freezing interfaces of the crystal-to-crystal

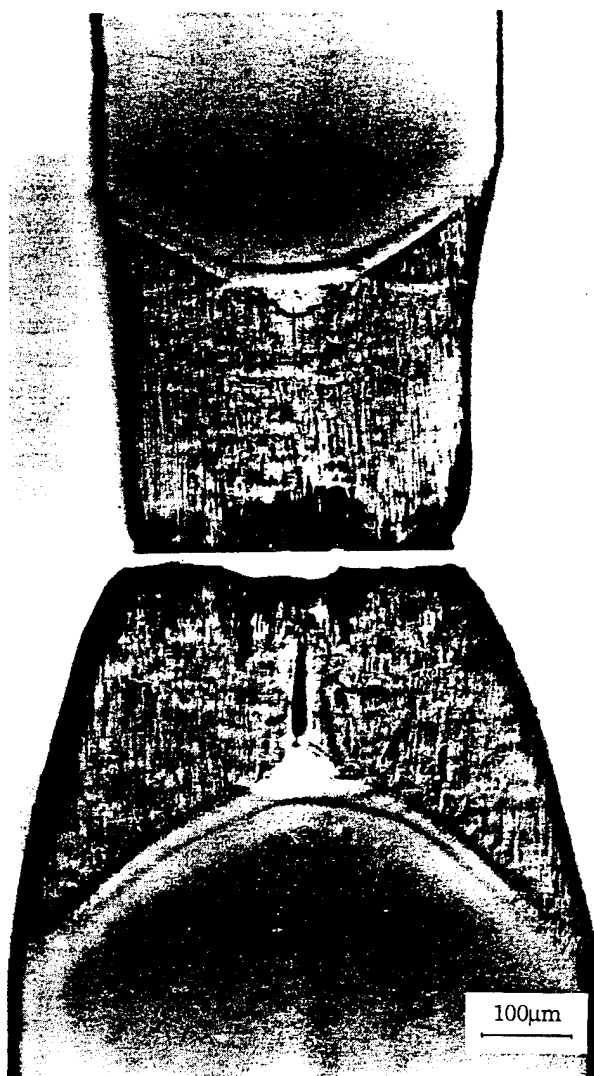


Fig. 10. Polished cross-section of the freezing (top) and melting (bottom) interfaces in a stable SBN61:Ce single crystal-fed molten zone.



Fig. 11. Enlarged view of the freezing (top) and melting (bottom) interfaces in a single-crystal-fed molten zone, 500X magnification.

SBN61:Ce zone are shown in fig. 11. The small uniformly shaped domes form a part of the outline of the interface. They are transparent and homogeneous, and do not have the many small bubbles present in the frozen zone material, indicating that crystallization had occurred.

The origin of the small domes is unclear, but one possibility focuses on Marangoni convection. Studies on Marangoni convection caused by the induced surface tension gradient along the free melt surface in the float zone growth of  $\text{NaNO}_3$ , demonstrated that convection in this material was appreciably large [29]. It was observed that

Marangoni convection strongly influenced the shape of the melt–solid interface, forming a shallow dome in the center of both interfaces. If this is also true for the SBN molten zone, convection in the melt may have caused the unusual melt–solid interface shape and indicates that under these growth conditions, the forces in the molten zone are more complex than previously considered.

The ceramic-fed zone did not have the dome in the center of the freezing interface, but the central area was flat like the crystal-fed zone. The turbulence caused by the air bubbles within the melt may have disrupted mixing, preventing the formation of the dome at the freezing and melting interfaces.

From fig. 4, a high dislocation density was observed at the periphery of the fiber while only a few dislocations were observed in the center of the fiber, in fibers grown from a ceramic feedrod. The tendency of the central area of the single crystal fiber to be dislocation-free can be understood from observation of the shape of the freezing interface. There are two possible explanations, one based on Marangoni convection and

the other based on gravitational effects. In Marangoni convection, the convection cells are only found at the outer region of the zone, leaving the central region undisturbed. Air bubbles in the ceramic-fed zone, stirred by convection, would cause disturbances at the freezing interface in the periphery region only (fig. 12). If these forces were strong enough to disturb the melt–solid interface, the induced strain in the lattice would promote dislocation formation near the outer regions of the fiber. If convection was not present, then gravitational forces could have also caused the air bubbles to accumulate at the upper region of the molten zone. Growth experiments in the downward direction would aid in understanding the origin of the dislocation patterns.

In our samples the observed striations, produced only in unstable growth, were found only in the central area of the fiber and not at the periphery (fig. 8a). This indicates that the central area of the stable freezing interface, where strong mixing would not be present, was sensitive to compositional perturbations. Mixing, driven by convection, would decrease this tendency towards striation formation in the outer region of the

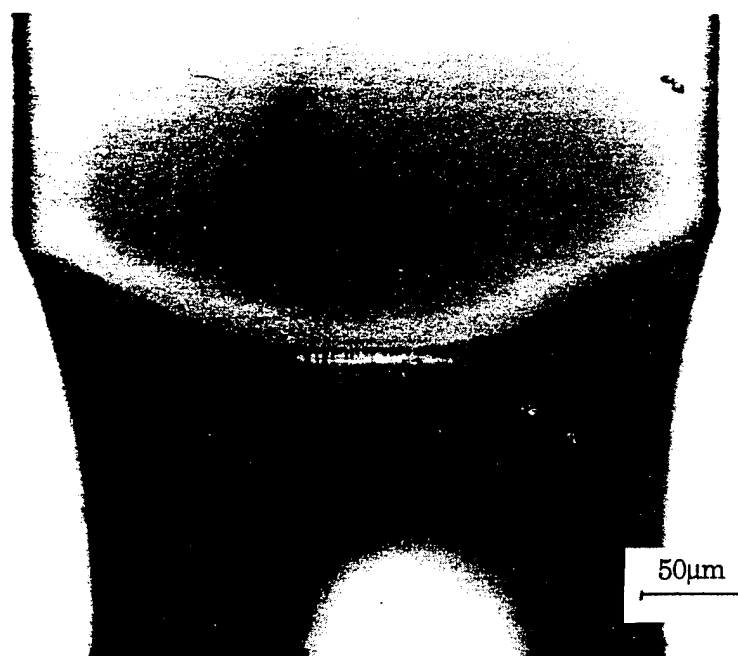


Fig. 12. Polished cross-section of the freezing interface in a stable ceramic-fed molten zone of the SBN61:Ce single crystal fiber.

fiber, even though equilibrium in the molten zone was not attained. Rotation of the seed and feedrod may also promote better mixing of the melt, reducing the possibility of the formation of compositional striations.

### 3.6. Domain configuration of the SBN single crystal fibers

To determine if the SBN61:Ce fibers grew in a single domain state, the pyroelectric properties were measured on an as-grown fiber and then re-measured on the same sample after poling. Using the Byer-Roundy technique, the pyroelectric response was measured as the samples were heated from room temperature, 20°C, at a rate of 4°C/min [30].

Because the transition temperature was close to room temperature, care was taken not to expose the sample to heat, which could change the domain configuration during sample preparation. After measuring the pyroelectric current on heating, an electric field (11 kV/cm) was applied, and the sample was cooled to room temperature. The field was removed and the sample was shorted for 2 min to remove excess charge. The pyroelectric current was measured again, on heating, under the same conditions.

The pyroelectric current of the as-grown and poled sample as function of temperature is shown in fig. 13. The polarization could not be accurately calculated because of the extensive conduc-

tion at higher temperatures. The poled sample did exhibit a very small peak at 97°C, corresponding to the Curie temperature and this was reproducible in subsequent measurements. A comparison of the magnitude of the current at 97°C of the as-grown and poled samples indicate that the as-grown fiber is not single domain. The high conductivity and Curie temperature in these fibers, not observed in the Czochralski-grown crystals, indicated that the single crystal fibers are highly defective or disordered, and this may be attributed to the rapid growth rate. After annealing at 1000°C, the conductivity was eliminated and the Curie temperature was reduced. The resulting temperature dependence of the pyroelectric current was similar to Czochralski-grown SBN [15].

## 4. Conclusions

The growth of single crystal fibers of the incongruently melting  $\text{Sr}_x\text{Ba}_{1-x}\text{Nb}_2\text{O}_6$  solid-solution system was achieved for compositions across the solid-solution range. Clear transparent crystals from starting compositions of  $x = 0.25, 0.40, 0.50, 0.61, 0.75$  and cerium-doped SBN61 were successfully grown.

The growth of SBN61:Ce single crystal fibers under stable conditions resulted in long, uniform diameter, single crystal fibers. At a growth rate of about 40 mm/h, stable growth conditions were established after ~10 mm of growth, as determined by the rapid decrease in the dislocation density with increasing crystal length. Although the interior crystal quality was high, the outer surface of the single crystal fibers was found to contain many dislocations. Growth from single crystal feedrods produced crystals with far fewer dislocations than crystals grown from ceramic feedrods. The SBN61:Ce single crystal fibers did not grow in a single domain state.

Varying the growth rate under stable zone conditions did not affect the composition along the length of the SBN61:Ce crystal, and nor did it affect the dislocation density or distribution within the fiber. Only under highly unstable growth conditions were compositional striations

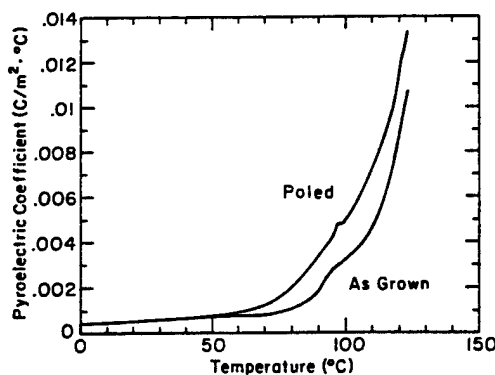


Fig. 13. Pyroelectric coefficient versus temperature of an as-grown and subsequently poled, as-grown SBN61:Ce single crystal fiber *c*-plate.

and large dislocation etch pits, e.g. square spiral and closed terrace dislocation etch pits, observed.

The SBN61:Ce single crystal-fed zone displayed an unusual and previously unreported dome in the center of both melting and freezing interfaces. The shape of these interfaces was thought to be caused by convection within the molten zone, driven by surface tension gradients on the melt surface. The ceramic-fed zones retained the same general shape, but did not have the small domes observed in the single crystal-fed zones. This was consistent with the observed dislocation distribution and the placement of the compositional striations in single crystal fibers grown under various conditions.

#### Acknowledgements

The technical assistance of D. Brennenman, T. Gingher, P. Klinger and R. Wilson was greatly appreciated.

#### References

- [1] R.S. Feigelson, *Mater. Sci. Eng. B* 1 (1988) 67.
- [2] D.H. Jundt, M.M. Fejer and R.L. Byer, *Appl. Phys. Letters* 55 (1989) 2170.
- [3] Y.S. Luh, R.S. Feigelson, M.M. Fejer and R.L. Byer, *J. Crystal Growth* 85 (1986) 264.
- [4] M. Saifi, B. Dubois, E.M. Vogel and F.A. Thiel, *J. Mater. Res.* 1 (1986) 452.
- [5] S. Ducharme, J. Feinberg and R.R. Neurogaonkar, *IEEE J. Quantum Electron.* QE-23 (1987) 2116.
- [6] R.R. Neurogaonkar, W.K. Cory, J.R. Oliver, E.J. Sharp, M.J. Miller, W.W. Clark, G.L. Wood and G.J. Salamo, *Mater. Res. Bull.* 24 (1989) 589.
- [7] A.M. Glass, *J. Appl. Phys.* 40 (1969) 4699.
- [8] P.V. Lenzo, E.G. Spencer and A.A. Ballman, *Appl. Phys. Letters* 11 (1967) 23.
- [9] L. Hesselink and S. Redfield, *Opt. Letters* 13 (1988) 877.
- [10] J.K. Yamamoto, D.A. McHenry and A.S. Bhalla, *J. Appl. Phys.* 70 (1991) 3215.
- [11] J.K. Yamamoto and A.S. Bhalla, *Mater. Res. Bull.* 24 (1989) 761.
- [12] W.R. Edmonds, *Appl. Opt.* 12 (1973) 1940.
- [13] Y. Ito, H. Kozuka, Y. Kashiwada and Y. Furuhashi, *J. Appl. Phys.* 14 (1975) 1443.
- [14] R.B. Maciulek, T.L. Schuller and S.T. Liu, *J. Electron. Mater.* 5 (1976) 415.
- [15] Y. Ito and Y. Furuhashi, *Phys. Status Solidi (a)* 23 (1974) 147.
- [16] J.K. Yamamoto, PhD Thesis, Pennsylvania State University (1990).
- [17] T. Surek and S.R. Coriell, *J. Crystal Growth* 37 (1977) 253.
- [18] A.B. Dreeben, K.M. Kim and A. Schujko, *J. Crystal Growth* 50 (1980) 126.
- [19] M.M. Fejer, PhD Thesis, Stanford University (1986).
- [20] J.P. Wilder, D.H. Jundt, L. Galambos and L. Hesselink, *J. Crystal Growth* 114 (1991) 500.
- [21] J.L. Nightingale, PhD Thesis, Stanford University (1986).
- [22] S.R. Coriell, S.C. Hardy and M.R. Cordes, *J. Colloid Interface Sci.* 60 (1977) 126.
- [23] W.G. Pfann and D.W. Hagelbarger, *J. Appl. Phys.* 27 (1965) 12.
- [24] J.R. Carruthers and M. Grasso, *J. Crystal Growth* 13/14 (1972) 611.
- [25] K.M. Kim, A.B. Dreeben and A. Schujko, *J. Appl. Phys.* 50 (1979) 4472.
- [26] Y. Ito, H. Kozuka, Y. Kashiwada and Y. Furuhashi, *J. Appl. Phys.* 14 (1975) 1443.
- [27] K. Megumi, N. Nagatsuma, Y. Kashiwada and Y. Furuhashi, *J. Mater. Sci.* 11 (1976) 1583.
- [28] T. Aida and T. Fukazawa, *J. Crystal Growth* 78 (1986) 263.
- [29] D. Schwabe, A. Scharmann, F. Preisser and R. Oeder, *J. Crystal Growth* 43 (1978) 305.
- [30] R.L. Byer and C.B. Roundy, *Ferroelectrics* 3 (1972) 333.

**Appendix 4.**

**"Optical and Electrooptical Properties of Lead Magnesium Niobate-Lead Titanate,"  
Ph.D. Thesis, Penn State University (1992).**

**D.A. McHenry**

The Pennsylvania State University  
The Graduate School  
Program in Solid State Science

**OPTICAL AND ELECTROOPTICAL PROPERTIES OF  
LEAD MAGNESIUM NIOBATE - LEAD TITANATE**

A Thesis in  
Solid State Science  
by  
Dean A. McHenry

Submitted in Partial Fulfillment  
of the Requirements  
for the Degree of

Doctor of Philosophy

May 1992

© 1992 by Dean A. McHenry

## ABSTRACT

The optical and electrooptical properties of a relaxor ferroelectric Lead magnesium niobate,  $\text{Pb}(\text{Mg}_{1/3}\text{Nb}_{2/3})\text{O}_3$  (PMN), and its solid solution with Lead titanate,  $\text{PbTiO}_3$  (PT) to form  $(1-x)\text{Pb}(\text{Mg}_{1/3}\text{Nb}_{2/3})\text{O}_3 - (x)\text{PbTiO}_3$  (PMN-PT) have been examined in hopes of realizing its potential usefulness as an electrooptic material. A better insight into the underlying nature of optical phenomena in this and other relaxor ferroelectric solid solution systems was also a goal of this effort. Fundamental optical property measurements such as spectral transmission, refractive index, birefringence, thermooptic and electrooptic coefficients were undertaken in order to characterize compositional and structural relationships for PMN-PT.

Spectral transmission measurements for these perovskite structure materials indicate an optical bandgap of about 3.35 eV corresponding to the onset of transmission in the near UV near 380 nm. Increasing transmission of light (near 60%) for thin polished ceramic samples of PMN-PT occurs out into the infrared regime without significant absorption to wavelengths greater than  $5\mu\text{m}$  and then decreasing transmission to become totally absorbing at  $10\mu\text{m}$ .

Refraction of light as a function of frequency for many PMN-PT compositions was examined by the minimum deviation method. For this system the refractive index increases nearly linearly from PMN ( $n_d = 2.5219$ ) by  $2.415 \times 10^{-3}$ /mole %  $\text{PbTiO}_3$  added. The optical dispersion was successfully modeled upon a single term Sellmeier oscillator equation even

for these  $\text{Pb}^{2+}$  A-site perovskite compounds which have a Pb 6s<sup>2</sup> electronic energy level in the region of the lowest conduction band modifying the predominant B-O oxygen-octahedra interactions.

Thermooptic properties,  $n(T)$ , were undertaken over a temperature range sufficient to ascertain the ferroelectric polarization contribution to the refractive index. Birefringence measurements sensitive to long range polar order were also performed as a complement to the  $n(T)$  measurements. The  $n(T)$  curves for the compositions with small amounts of  $\text{PbTiO}_3$  were shown to exhibit relaxor effects exemplified by a purely paraelectric linear high temperature regime and then a gradual departure from linear behavior at a temperature well above ( $\sim 300^\circ\text{C}$ ) the dielectric constant maximum temperature. This reduction of the refractive index is explained by the existence of short range ordered regions of local polarization (superparaelectric behavior). The average polarization remains zero in this regime but the nonzero root mean square polarization biases the refractive index by the quadratic electrooptic effect. Only below the freezing temperature  $T_f$  of the interacting and coalescing polar regions is there a measurable optical anisotropy  $\Delta n(T)$  observed from uniformly distorted macroscopic scale domains. The field induced birefringence for .80PMN-.20PT of .005 is comparable to other perovskite materials.

For this system of relaxor ferroelectrics the response to simultaneous optical and electrical fields as an electrooptic media has been demonstrated to be based on other solid-state features such as their dielectric, polarization, and ferroelectric properties. Electrooptic and polarization hysteresis loops were measured as a function of electric field and temperature. The measured quadratic electrooptic R coefficients at room

temperature (e.g  $14.1 \times 10^{-16} \text{ m}^2/\text{V}^2$  for .90PMN-.PT with  $\lambda = 632.8\text{nm}$ ) were such that several halfwaves of retardation could be produced for modest fields. Electrooptic shuttering experiments indicated that switching speeds of the order 700nsec could be readily achieved in .93PLMN-.07PT bulk ceramic samples. Polarization optic coefficients were found to be of order  $.01\text{m}^4/\text{C}^2$  and in common with many other Pb perovskite relaxors an order of magnitude smaller than non Pb materials. In addition to electrically controllable birefringence, longitudinal electrooptic light scattering and spectral filtering effects were also observed.

Because of their large electrooptic coefficients, photorefractive effects have been shown to be readily induced by the excitation of free carriers caused by illumination from near bandgap (375 nm) radiation. Photoassisted domain switching (PDS) has been observed during measurement of polarization -electric field hysteresis loops. Photorefractive induced birefringence ( $>10^{-4}$ ) under simultaneous UV illumination and electric field has been demonstrated in polycrystalline ceramics of composition .90PMN-.10PT. This photorefractive index pattern storage was demonstrated to be maintainable at least for several hours, reversible under the action of an electric field of opposite polarity, and erasable by thermal treatment or broadband illumination.

The large quadratic electrooptic coefficients in polycrystalline ceramics of PMN-PT, comparable to any previously measured electrooptic ceramics, and linear electrooptic coefficients demonstrated in near morphotropic phase boundary single crystals such as .70PMN-.30PT may prove to be of significant interest for applications involving electrooptic modulation and photorefractive effects.

**Appendix 5.**

**"Wavelength Multiplexing Fiber Holographic Construction Using a Ce and Fe Doped PR Fiber with a Tunable Visible Light Laser Diode," *IEEE Photonics Tech. Letters*, **5**, 1230-1233 (1993).**

**F.T.S. Yu  
S. Yin  
F. Zhao  
H. Zhou, and  
A.S. Bhalla**

# Wavelength-Multiplexed Holographic Construction Using a Ce: Fe: Doped PR Fiber with a Tunable Visible-Light Laser Diode

Francis T. S. Yu, *Fellow, IEEE*, Shizhuo Yin, and Amar S. Bhalla, *Member, IEEE*

**Abstract**—A wavelength-multiplexed reflection-type photorefractive (PR) fiber hologram using a tunable visible-light laser diode is presented. We have shown that the wavelength-multiplexed PR fiber hologram offers a higher and more uniform wavelength selectivity than that of the transmission-type. Experimental demonstrations of wavelength-multiplexed reflection-type PR fiber hologram are provided, which are consistent with the theoretical analysis.

Manuscript received June 22, 1993; revised July 29, 1993. This work was supported by the Defense Advanced Research Projects Agency through the U.S. Army Research Office under Contract DAAL 03-92-G-0328.

F. T. S. Yu, S. Yin, and A. S. Bhalla are with The Pennsylvania State University, Department of Electrical and Computer Engineering, University Park, PA 16802.

IEEE Log Number 9212448.

THE use of photorefractive (PR) materials for data storage and interconnection has attracted wide attention in optical signal processing and computing [1]–[8]. The salient features of PR material are the large storage capacity, high diffraction efficiency, and high angular and wavelength selectivities. The using of PR fibers [4], [9]–[11] to substitute PR bulk crystals in recent years has also provided an alternative to a variety of applications. In this paper, we shall first discuss the angular and the wavelength selectivities of PR fiber hologram, using the coupled wave theory of Kogelnik [12], in which we have noted that the estimated results are consistent with the experimental data, reported by Hesselink *et al.* [7]. Since the reflection-type wavelength multiplexed hologram offers a low crosstalk and a higher and uniform selectivity, [1], [13]

our discussion, in experimental part, will focus on this type.

From the previous works [1], [2] we know that the angular selectivities (in terms of the external write-in angle  $\alpha$ ) can be written as

$$\left\{ \frac{1}{\Delta \alpha} \right\}_t = \frac{\sin \alpha \cos \alpha}{\sqrt{n^2 - \sin^2 \alpha}} \frac{d}{\lambda}, \quad (1)$$

$$\left\{ \frac{1}{\Delta \alpha} \right\}_r = \frac{\sin \alpha \cos \alpha}{\sqrt{n^2 - \cos^2 \alpha}} \frac{d}{\lambda}. \quad (2)$$

To calculate the wavelength selectivities,  $k$ -vector diagrams (the detail discussions about it can be found in [1]) are considered as shown in Fig. 1. By referring to the moment conservation principle, a change in the diffraction beam angle  $\theta$  ( $\theta$  is the internal write-in angle) by  $\Delta \theta$  is needed if the readout wavelength is deviated from the recording wavelength ( $\lambda$ ) by  $\Delta \lambda$ . In view of Fig. 1(a), we have

$$(|k| + \Delta k) \sin \theta + (|k| + \Delta k) \sin (\theta - \Delta \theta) = 2|k| \sin \theta \quad (3)$$

where  $|k| = 2\pi n/\lambda$ . Thus, the wavelength selectivity for the transmission-type fiber hologram can be estimated as

$$\left| \frac{\lambda}{\Delta \lambda} \right| = 1 + \frac{2}{\frac{\sin \theta}{\sin (\theta - \Delta \theta)} - 1}. \quad (4)$$

By using the Snell's refraction law, the wavelength selectivity for the transmission-type is given by

$$\left\{ \frac{\lambda}{\Delta \lambda} \right\}_t = 1 + \frac{2}{\frac{\sin \alpha/n}{\sin \left[ \sin^{-1} \left( \frac{\sin \alpha}{n} \right) - \frac{\lambda}{d \sin \alpha} \right]} - 1} \quad (5)$$

which is a more exact solution as compared with the result that we have previously derived [1]. The previous result is the first-order approximation result, which is more valid for  $\alpha$  in the range of  $10^\circ$ – $80^\circ$ . However, this result is more valid for  $\alpha$  in the range of  $22^\circ$ – $88^\circ$ .

Similarly, for the reflection-type fiber hologram, as represented by the  $k$ -vector diagram in Fig. 1(b), the wavelength selectivity of the fiber hologram can be estimated as [1]

$$\left\{ \frac{\lambda}{\Delta \lambda} \right\}_r = \frac{\sqrt{n^2 - \cos^2 \alpha}}{\lambda} d. \quad (6)$$

To test the validity of these results as used for fiber holograms, we use the transmission-type angular-multiplexed type hologram as an example of comparing the theoretical analysis with the experimental data obtained by Hesselink [7] as tabulated in Table I. From this table, we see that the estimated results are closed to the experimental data (in the same order). The consistency may be

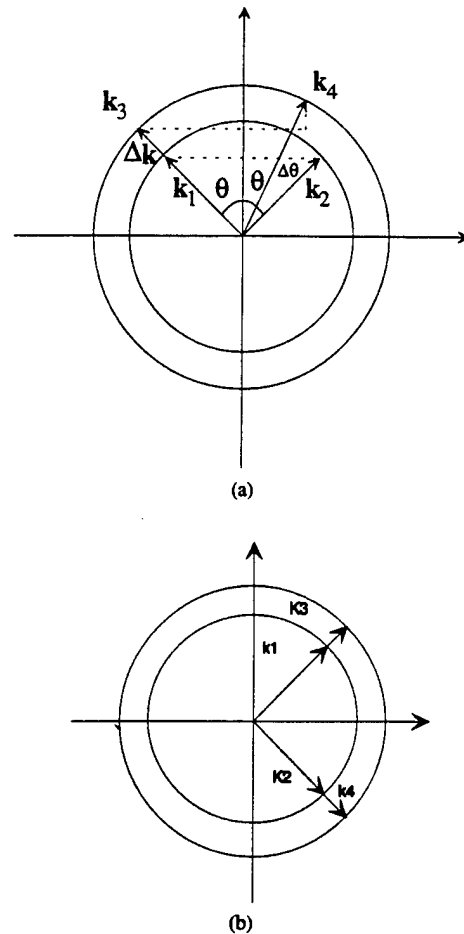


Fig. 1. Momentum conservation principle.  $k_1, k_2$ ; writing wave vectors.  $k_3$ ; readout wave vector.  $k_4$ ; diffracted wave vector.  $\Delta k$  reading wavelength deviation. (a) For transmission-type hologram. (b) For reflection-type hologram.

TABLE I  
CALCULATED AND EXPERIMENTAL DATA OF ANGULAR SELECTIVITY  
FOR FIBER HOLOGRAM  $\lambda = 515$  NM  $N = 2.28$ ,  $D = 4$  MM

Recording Angle ( $2\alpha$ )	Angular Selectivity Calculated Results (Degree)	Angular Selectivity Experimental Data (Degree)
0.7	2.41	1.43
3	0.64	0.86
5	0.39	0.57
10	0.19	0.44
20	0.098	0.26

explained as that the crystal fiber used in the experiment is several hundred microns in diameter and several millimeters in length. Thus, the performance of the fiber is similar to the performance of bulk crystals.

Fig. 2 shows the normalized angular and wavelength selectivities for both types of fiber holograms, in which we see that the angular selectivities are limited by  $15^\circ \leq \alpha \leq 75^\circ$  (FWHM). As in contrast, the wavelength selectivity for the reflection-type hologram is shown to be more sensitive and uniform. Moreover, it can also be shown that this type of hologram has a lower crosstalk noise [13]. Thus, it is the best choice for data storage. As a numerical

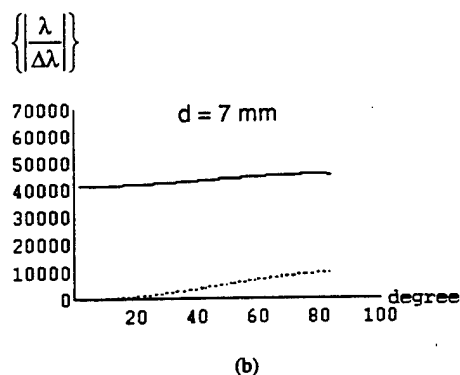
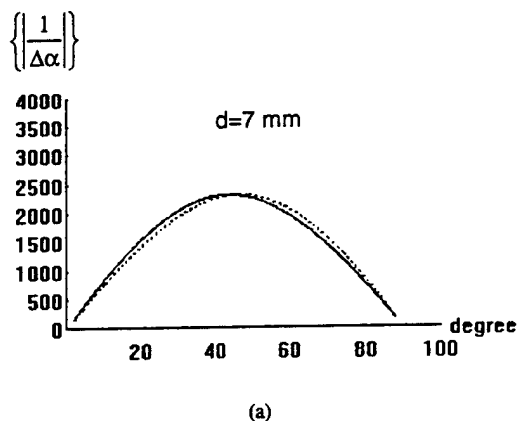


Fig. 2. (a) Normalized angular selectivity ( $\lambda/d = 10^{-4}$ ,  $n = 2.28$ ). (b) Normalized wavelength selectivity ( $\lambda/d = 10^{-4}$ ,  $n = 2.28$ ). Dashed line stands for transmission-type; solid line stands for reflection-type.

example, we let the length and the recording wavelength be  $d = 7$  mm and  $\lambda = 0.7$   $\mu$ m, the wavelength selectivity for a reflection fiber hologram is in the order of  $10^4$ .

For experimental demonstration, we have used a Ce:Fe-doped LiNbO<sub>3</sub> crystal fiber to construct a fiber hologram, as shown in Fig. 3. The crystal fiber was grown by a laser heated pedestal growth system in the Material Research Laboratory at Penn. State with a growing temperature about 1260°C. The doping levels of Ce:Fe in the PR crystal fiber were measured to be about 300 ppm and 500 ppm, respectively, and the oxidizing and reducing temperature and the time were set about 700°C and 5 h in the open air and LiCO<sub>3</sub> power environments, respectively. The size of the PR fiber is about 7 mm in length and 0.7 mm in diameter with a loss about 50%. Notice that the reason of using the Ce:Fe: doped LiNbO<sub>3</sub> PR fiber are: It has a higher photosensitivity in the red-light region, which is suitable for using a low-power visible-light tunable diode laser, and it has a high curie point of about 1200°C, which is rather robust against the ambient temperature variation.

A 5-mw tunable laser diode (New Focus Inc. model 6102,  $\lambda \approx 670$  nm, with a tuning range of 12 nm) is used as the light source. The object beam is measured to be about 2 mW/cm<sup>2</sup> with a write-in angle of  $\alpha \approx 90^\circ$ . By

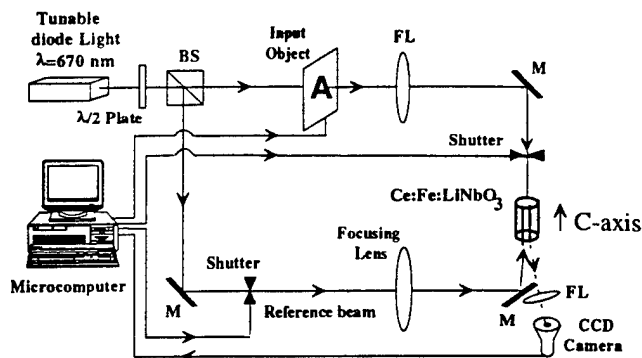


Fig. 3. Experimental setup for the construction of a wavelength-multiplexed PR crystal fiber hologram.

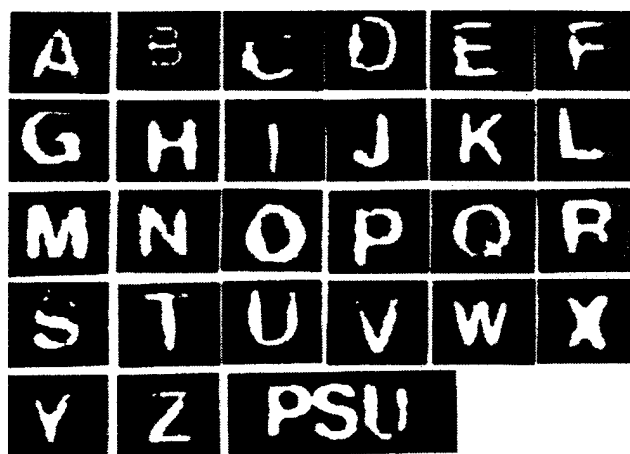


Fig. 4. Holographic images obtained from a Ce:Fe: doped LiNbO<sub>3</sub> PR fiber holograms.

using the wavelength tuning step of  $\Delta\lambda = 0.1$  nm with about 5 s exposure time, a PR-fiber hologram is constructed. The diffraction efficiency for each multiplexed hologram is about 1%. By blocking the object beam and tuning the laser diode, a sequence of holographic images are reconstructed as depicted (in part) in Fig. 4.

From this figure, one can see that the obtained experimental results are relatively good. There are no obvious crosstalks among them, which is consistent with the theoretical evaluation. Notice that there are some distortions on the reconstructed images. Based on our experimental observation, the random distortions are mainly due to the nonuniform refractive index distribution within the fiber and the scattering effects coming from both the inside and not well-polished surface. And, the straight line distortion comes from the scanning lines of the receiver monitor. We do not believe that the distortion comes from the crosstalk noise. The reason is that we can get similar distortion for just recording only one hologram. We further want to note that there is no significant difference (about 20% deviation) in diffraction efficiency for each holographic channel if the same exposure energy is used in each channel. We believe that these adverse effects can

be alleviated if the PR fiber would have a more uniform refractive index distribution and been smoothly polished. At any rate, from these results, we have shown the feasibility of potential application of PR fibers to optical memory, interconnection, and others.

## REFERENCES

- [1] S. Wu, Q. Song, A. Mayers, D. Gregory, and F. T. S. Yu, "Reconfigurable interconnections using photorefractive holograms," *Appl. Opt.*, vol. 29, p. 1118, 1990.
- [2] F. T. S. Yu and S. Jutamulia, "Optical Signal Processing," in *Computing and Neural Networks*. New York: Wiley-Interscience, ch. 7, 1992.
- [3] P. A. Yeh, A. E. T. Chiou, and J. Hong, "Optical interconnection using photorefractive dynamic holograms," *Appl. Opt.*, vol. 27, p. 2093, 1988.
- [4] L. Hesselink and S. Redfield, "Photorefractive holographic recording in strontium barium niobate fibers," *Opt. Lett.*, vol. 13, p. 877, 1988.
- [5] F. Ito and K. Kitayama, "Real-time holographic storage of a temporal bit sequence by using angular multiple recording of spectral components," *Opt. Lett.*, vol. 17, p. 1152, 1992.
- [6] Y. Qiao and D. Psaltis, "Sampled dynamic holographic memory," *Opt. Lett.*, vol. 17, p. 1376, 1992.
- [7] L. Hesselink, "Photorefractive fibers for optical data storage and processing," *Int. J. Optoelectron.*, vol. J, p. 103, 1990.
- [8] K. Kitayama and F. Ito, "Optical signal processing using photorefractive effect," *Multidimensional Systems and Signal Processing*, vol. 2, p. 401, 1991.
- [9] J. K. Yamamoto and A. S. Bhalla, "Growth of  $\text{Sr}_{1-x}\text{Ba}_x\text{Nb}_2\text{O}_6$  single crystal fibers," *Mater. Res. Bull.*, vol. 24, p. 761, 1989.
- [10] H. Yoshinaga, K. Kitayama, and H. Oguri, "Holographic image storage in iron-doped lithium niobate fibers," *Appl. Phys. Lett.*, vol. 56, p. 1728, 1990.
- [11] Y. Sugiyama, S. Yagi, I. Yokomaha, and I. Hatakeyama, "Holographic recording in cerium doped strontium barium niobate a-axis single crystal fiber," *Japan. J. Appl. Phys.*, vol. 31, p. 708, 1992.
- [12] H. Kogelnik, "Coupled wave theory for thick hologram grating," *Bell Syst. Tech. J.*, vol. 48, p. 2909, 1969.
- [13] G. A. Rakuljic, V. Leyva, and A. Yariv, "Optical data storage by using orthogonal wavelength multiplexed volume holograms," *Opt. Lett.*, vol. 17, p. 1471, 1992.

**Appendix 6.**

**"Linear Electrooptic Coefficients Measured Utilizing Modified Mach-Zehnder Interferometer Technique," *Proceedings of Thirty-Eighth Brazilian Congress of Ceramics*, Blumenau, Brazil (June 18-21, 1994).**

**J. M. Pova  
Ruyan Guo and  
A.S. Bhalla**

## UTILIZAÇÃO DO INTERFERÔMETRO DE MACH-ZEHNDER MODIFICADO PARA MEDIDAS DE COEFICIENTES ELETRO-ÓTICOS LINEARES

J. M. Póvoa\*, R. Guo\*\* e A. S. Bhal'a\*\*

\*Universidade Federal de São Carlos  
Depto. de Física - Grupo de Cerâmicas Ferroelétricas  
Rodovia Washington Luiz, Km 235 - Tel (0162) 74 82 27

\*\*Materials Research Laboratory  
The Pennsylvania State University  
Universtiy Park - PA - 16 802-4801 - USA

### RESUMO

Técnicas interferométricas tem mostrado ser de grande utilidade para se medir propriedades eletro-óticas em cristais e cerâmicas, e o interferômetro de Mach-Zehnder, que chega a ter uma sensibilidade para se detectar variações de caminho ótico chega a ser menores do que  $0,01\text{\AA}^1$ , é uma das ferramentas bastante poderosas para se medir essas propriedades.

Os coeficientes eletro-óticos lineares  $r_{13}$  e  $r_{33}$  em função da temperatura de monocristais de PBN são apresentados.

### ABSTRACT

Interferometric techniques have been shown to be powerful in measuring electrooptical effects in crystals and ceramics. Mach-Zehnder interferometer, particularly, capable to resolve an optic path length difference less than  $0.01\text{\AA}^1$ , is an effective tool to measure electrooptic properties.

This paper reports linear electrooptical coefficients  $r_{13}$  and  $r_{33}$  of tungsten bronze single crystals, measured using a modified Mach-Zehnder interferometer, as functions of temperature.

Utilizando-se um fotodetector onde a diferença de potencial gerada é linearmente proporcional à intensidade da luz teremos:

$$V_{out} \propto I_{\sim} \quad e \quad V_{pp} \propto I_{max\sim}$$

ou:

$$V_{out}/V_{pp} = I_{\sim}/I_{max\sim} = (d_o \cos \omega t) 2\pi/\lambda$$

Resultando

$$V_{out} = (2\pi/\lambda) V_{pp} (d_o \cos \omega t) \quad (14)$$

Como o sinal lido no "lock-in", sincronizado com o campo elétrico aplicado à amostra, é lido em rms e o sinal lido no osciloscópio ( $V_{pp}$ ), é lido de pico a pico, é necessário converter uma dessas medidas para que se tornem semelhantes, por exemplo  $V_{pp} \rightarrow (V_{pp}/2\sqrt{2})_{rms}$ . Após esses ajustes a equação anterior pode ser reescrita como:

$$V_{out} / (V_{pp}/2\sqrt{2}) = d_o 2\pi/\lambda$$

de onde sai:

$$d_o = \lambda V_{out} \sqrt{2} / (\pi V_{pp}) \quad (15)$$

onde:

$\lambda$  no caso é igual a 6328Å

$V_{out}$  é a voltagem lida no "lock-in"

$V_{pp}$  é a voltagem pico a pico lida no osciloscópio

#### MEDIDAS EM MONOCRISTAIS DE PBN

Utilizamos monocristais de  $Pb_{1-x}Ba_xNb_2O_6$  (PBN(1-x)%), crescidos pelo método de Czochralski, que após orientados, cortados e polidos opticamente, foram utilizados para medidas de coeficientes eletro-óticos. As amostras foram previamente polarizadas com um campo DC de 10KV/cm, mantido por 15 minutos a temperaturas entre 80 a 120°C, sendo resfriado até a temperatura ambiente com o campo aplicado em banho de óleo. Medimos  $r_{13}$  e  $r_{33}$  nos monocristais de PBN57 e PBN50 em função da temperatura. Os resultados obtidos podem ser vistos nas figuras 3 e 4

Em todas as medidas a contribuição para a mudança do caminho ótico devido ao efeito piezoelétrico, para as campos elétricos aplicados e temperaturas medidas foram menores do que 1%.

Como pode ser visto  $r_{33}$  tanto no PBN50 quanto no PBN57 é maior do que  $r_{13}$ . Pode também ser observado que valores maiores tanto de  $r_{13}$  quanto de  $r_{33}$  são obtidos no PBN57, isso se deve ao fato de estar mais próximo da fase morfofropica. Ruyan<sup>(2)</sup> já havia observado que os coeficientes efetivos  $r_c$  também é maior no PBN57 do que no PBN50. A dependência com a temperatura observada não é muito grande no intervalo de temperatura medido, intervalo esse que é bem abaixo da temperatura de transição de fase ferro / paraelétrico que em ambos os caso são superiores a 300°C. Medidas feitas também em outros cristais com estrutura tungstênio-Bronze<sup>(4)</sup>

central de interferência e que o diâmetro dessa franja seja maior do que a abertura do fotodetector. Uma lente pode ser colocada na frente do fotodetector a fim de abrir (divergir) um pouco a franja central.

## PROCEDIMENTO EXPERIMENTAL

A medida é feita da seguinte forma:

Inicialmente uma tensão dente de serra de baixa frequência ( $\sim 5\text{Hz}$ ) é aplicada ao espelho de referência de forma a produzir deslocamento neste de pelo menos um comprimento de onda, dessa forma o sinal detectado pelo fotodetector tem pelo menos uma oscilação completa da forma cosenoidal que é observado e armazenado em um canal do osciloscópio (canal A), após essa etapa o sinal dente de serra é desligado e um sinal DC ajustável é aplicado ao espelho, a fim de produzir a diferença de fase inicial, o sinal gerado pelo fotodetector agora observado no canal B do osciloscópio é composto de um sinal DC devido ao deslocamento do espelho gerado pelo sinal DC a ele aplicado, superposto a um pequeno sinal alternado gerado pela amostra, uma vez que o campo aplicado à amostra é AC. O deslocamento do espelho é ajustado para que o sinal praticamente constante atinja os pontos A ou B do sinal armazenado no canal A do osciloscópio, quando isso ocorre, o pequeno sinal alternado gerado pela amostra será mais sensível, e é medida pelo "lock-in", ajustado de forma a tomar a medida durante um tempo suficiente para reduzir o ruído.

O sinal aplicado à amostra produz uma variação do caminho ótico  $\Delta d = d_0 \cos \omega t$ , que causa uma variação na intensidade do feixe de luz. Essa variação é convertida pelo fotodetector em voltagem, e pode ser medida pelo "lock-in" (em rms). Do sinal observado no canal A do osciloscópio é medido o valor de pico a pico que corresponde a um deslocamento de  $\lambda/2$  do espelho. Após o espelho ter sido ajustado para que o sinal observado varie em torno de A ou B., teremos:

$$I = 1/2(I_{\max} + I_{\min}) + 1/2(I_{\max} - I_{\min}) \cos(\pi/2 + \theta) \quad (9)$$

como as medidas são feitas em AC (Lock-in), só é detectado o termo periódico no tempo, que é:

$$I_{\sim} = 1/2(I_{\max} - I_{\min}) \cos(\pi/2 + \theta) = 1/2(I_{\max} - I_{\min}) \sin(\theta) \quad (10)$$

como  $\theta$  geralmente é pequeno

$$I_{\sim} \approx 1/2 (I_{\max} - I_{\min}) \theta \quad (11)$$

como  $\theta$  aqui é só o causado pela variação do caminho ótico produzido pela amostra, é dado pela equação 2

$$I_{\sim} \approx 1/2 (I_{\max} - I_{\min}) \Delta d \, 2 \pi / \lambda \quad (12)$$

Onde

$$\Delta d = d_0 \cos \omega t \quad (13)$$

sendo

$d_0$  é a amplitude do deslocamento sofrida pela amostra

$\omega$  é a frequência do campo aplicado

No caso dos ferroelétricos tetragonais com estrutura Tungstênio-Bronze ( 4mm), os únicos termos diferentes de zero são  $r_{13} = r_{23}$ ,  $r_{33}$  e  $r_{42} = r_{51}$

Quando o campo é aplicado ao longo do eixo z ( [001] ), somente os comprimentos da elipsoide muda, não sofrendo nenhuma rotação, e o cristal permanece opticamente uni axial. Nessas condições sai:

$$n_x = n_y = n_o' = n_o ( 1 - (1/2) r_{13} n_o^2 E_z ) \quad (5)$$

$$n_z = n_e' = n_e ( 1 - (1/2) r_{33} n_e^2 E_z ) \quad (6)$$

de onde sai:

$$\Delta n_x = - (1/2) r_{13} n_o^3 E_z \quad (7)$$

$$\Delta n_z = - (1/2) r_{33} n_e^3 E_z \quad (8)$$

## O INTERFERÔMETRO DE MACH-ZEHNDER MODIFICADO

O interferômetro de Mach-Zehnder é uma das técnicas que utiliza a interferência de luz para estudar propriedades eletro-ópticas de materiais<sup>(1,5,6,7)</sup>. W. Y. Pan e S. J. Jang <sup>(1)</sup> utilizando-se de um interferômetro de Mach-Zehnder modificado conseguiram medir variações de caminho ótico menores do que 0,01Å. A fig. 2 mostra esquematicamente esse interferômetro. Como fonte de luz monocromática um laser He-Ne é utilizado

O feixe de luz, se torna polarizada na direção desejada ao passar pelo polarizador P. Ao atingir o "splitter" BS1 parte do sinal é transmitido e parte é refletido. A parte refletida é utilizada como feixe de referência, esse feixe é novamente refletido no espelho de referência (RM) indo recombinar com o feixe de prova no "splitter" BS2. O feixe de prova, feixe transmitido no "splitter" BS1, ao passar pela amostra sofre uma defasagem devido a diferença de caminho ótico sofrido pelo feixe ao passar pela amostra. Esse feixe é refletido pelo espelho M indo recombinar com o feixe de referência no "splitter" BS2.

Após a interferência o feixe resultante terá uma intensidade dada pela equação 1 , que é medida pelo fotodetector.

Como a intensidade do sinal medido é proporcional ao coseno da fase, pequenas variações de  $\theta$  é mais sensível quando a variação se dá em torno de  $\pi/2$  ou  $3\pi/2$ , pontos A ou B da fig. 1

Medidas em torno dos pontos A ou B pode ser conseguidas, ajustando o espelho de referência RM de forma a produzir uma diferença inicial de caminho ótico. O sistema de realimentação do amplificador diferencial corrige possíveis flutuações de baixa frequência. Para diminuir o ruído de alta frequência, a medida é feita com um "lock-in". A amostra é excitada com uma tensão alternada (AC) da ordem de 1KHz.

A posição em que é colocado o espelho de referência pode trazer alguns problemas, se esse for deslocado consideravelmente da posição inicial onde se ajustou o sistema para produzir boa figura de interferência, uma vez que o feixe tanto incidente quanto o refletido não são perpendiculares ao espelho, implicando que variações na posição do espelho além de produzir diferença no caminho ótico, também desvia o feixe paralelamente, podendo fazer com que a figura de interferência onde se encontra o fotodetector seja deturpada. Mas para pequenas variações da posição, i.e. da ordem de alguns comprimentos de onda esse deslocamento paralelo podem ser desprezado.

O ideal nesse tipo de medida é que o fotodetector esteja posicionado na posição da franja

## INTRODUÇÃO

Recentemente estudos de efeitos eletro-óticos e de ótica não linear em óxidos ferroelétricos tem aumentado consideravelmente. Interferômetros que utilizam laser como fonte de luz são muito sensíveis a mudanças de caminho ótico, por isso são ferramentas bastante efetivas para medidas das constantes eletro-óticas.

Quando dois feixes de luz monocromática linearmente polarizadas de comprimento de onda  $\lambda$  sofrem interferência, a intensidade do feixe resultante é dado por:

$$I = 1/2 (I_{\max} + I_{\min}) + 1/2 (I_{\max} - I_{\min}) \cos \theta \quad (1)$$

onde:

$I_{\max}$  e  $I_{\min}$  são as intensidades máxima e mínima do feixe de após ter sofrido interferência

Se a diferença de fase  $\theta$  for somente devido a diferença de caminho ótico, essa é dada por

$$\theta = \Delta d \cdot 2\pi/\lambda \quad (2)$$

onde:

$\Delta d$  é a diferença de caminho ótico entre os dois feixes

## DETERMINAÇÃO DAS CONSTANTES ELETRO-ÓTICAS LINEARES

Geralmente os materiais eletro-óticos são também piezoelétricos, de forma que ao se aplicar um campo para observar o efeito eletro-ótico, também ocorrerá uma variação do comprimento da amostra devido ao efeito piezoelétrico, dessa forma a variação do caminho ótico produzido pelo campo elétrico, desprezado termos de ordem superiores, é dada por:

$$\Delta d = \Delta n \cdot l + n \cdot \Delta l \quad (3)$$

onde:

$\Delta n \cdot l$  é a variação do caminho ótico devido ao efeito eletro-ótico

$n \cdot \Delta l$  é a variação do caminho ótico devido ao efeito piezoelétrico

$l$  é o comprimento da amostra na direção em que o feixe luminoso é transmitido

$\Delta n$  é a variação do índice de refração

$\Delta l$  é a variação do comprimento da amostra devido ao efeito piezoelétrico

Para medidas de  $r_{13}$  ou  $r_{33}$  o campo elétrico deve ser aplicado ao longo do eixo  $z$  ( $[001]$ ), e o feixe de luz deve percorrer os eixos  $x$  ou  $y$  ( $[100]$ , ou  $[010]$ )

Os coeficientes eletro-óticos lineares (ou efeito de Pockels), saem da definição

$$\Delta(1/n^2) = \sum r_{ik} E_k \quad (4)$$

que pode ser representado por uma elipsoide, sendo:

$E_k$  ( $k=1,2,3$ ) os componentes do campo elétrico aplicado, e

$r_{ik}$  são os componentes do tensor eletro-ótico na notação reduzida ( $i=1,2,3,4,5,6$ )

mostraram resultados bastante semelhantes aos aqui apresentados

## FIGURAS

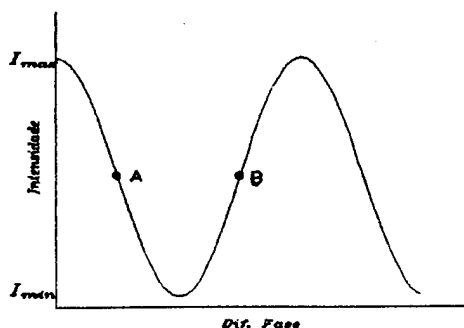


Fig. 1 - Intensidade da luz após a interferência, em função da diferença de fase

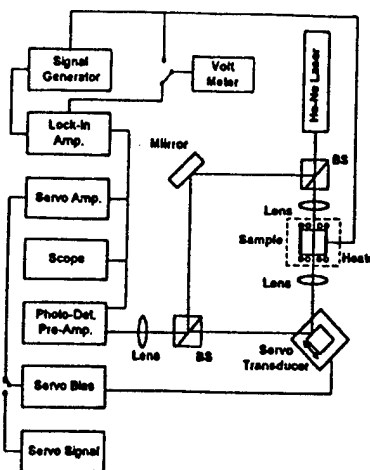


Fig. 2 - Diagrama de bloco do Interferômetro de Mach-Zehnder modificado

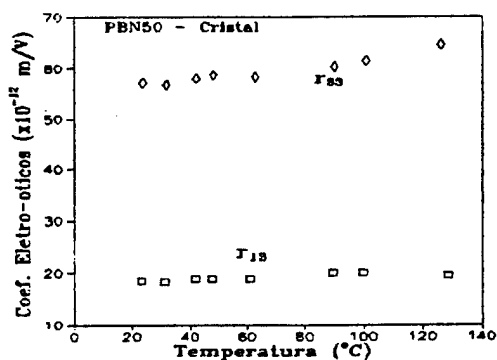


Fig. 3 - Coeficientes eletro-óticos em PBN50 como função da temperatura

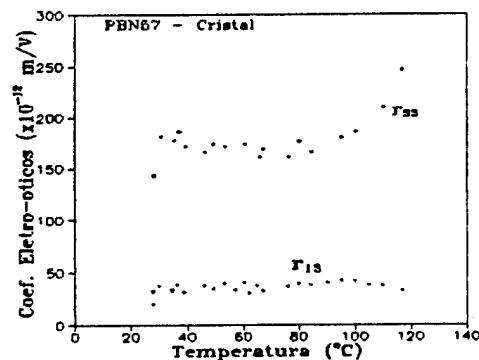


Fig. 4 - Coeficientes eletro-óticos do PBN57 como função da temperatura

## BIBLIOGRÁFIAS

- 1 - W. Y. Pan, S. J. Jang - Rev. Sci. Instrum. 61, 2109, (1990)
- 2 - R. Guo - PhD. Tesis, The Pennsylvania State University, (1990)
- 3 - Q. M. Zhang, W. Y. Pan, L. E. Cross - J. Appl. Phys. 63, 2492, (1988)
- 4 - R. Guo, J. M. Póvoa, A. S. Bhalla - Ferroelectrics ( a ser publicado)
- 5 - T. Yuhara, K. Tada, Yu-Shan Li - J. Appl. Phys, 71, 3966, (1992)
- 6 - N. Uchida et al - J. Appl. Phys. - 43, 4933, (1972)
- 7 - Y. Fujii, T. Sakudo - J. Appl. Phys. - 41, 4118, (1970)

**Appendix 7.**

**"Application of Fiber Speckle Hologram to Fiber Sensing," *Applied Optics*, 33(22) 5202-3 (1994).**

**Francis T.S. Yu  
Shizhuo Yin  
Jianzhong Zhang, and  
Ruyan Guo**

# Application of a fiber-speckle hologram to fiber sensing

Francis T. S. Yu, Shizhuo Yin, Jianzhong Zhang, and Ruyan Guo

A sensitive fiber-speckle field sensor using a Ce:Fe-doped LiNbO<sub>3</sub> photorefractive fiber hologram is introduced. We have shown that the sensitivity of this photorefractive fiber specklegram sensor can be of the order of 0.05  $\mu\text{m}$ . The proposed system would offer the widespread use of practical fiber-sensing applications.

Fiber-optic sensing has been shown to be one of the more important sensing technologies in recent years.<sup>1</sup> A new type of fiber sensor called the fiber specklegram sensor (FSS) was proposed recently.<sup>2,3</sup> In other words, by taking advantage of the sensitivity of the complex speckle field that exits from a multimode fiber, a highly sensitive FSS can be developed.

In previous papers<sup>2,3</sup> we proposed a multimode fiber-sensing system using photorefractive bulk crystal to construct a fiber-speckle hologram. However, using the bulk material for construction of the fiber-speckle hologram has some practical limitations: First, the physical size of the photorefractive (PR) crystal usually makes it awkward and inefficient for coupling with the sensing fiber. Second, the separation between the sensing fiber and the crystal hologram<sup>2,3</sup> is vulnerable to misalignment and environmental changes. Third, bulk crystal is more expensive compared with equivalent-length PR fiber.<sup>4,5</sup> Fourth, the large dimension of the bulk material makes the fiber specklegram sensing system rather large, which limits its practical application.

To alleviate these limitations, in this Note we demonstrate a FSS using a PR fiber (as the fiber specklegram recording material) as shown in Fig. 1. The sensing fiber is a step-index multimode silica

fiber with a 50- $\mu\text{m}$  core diameter, and the PR fiber is a specially doped Ce:Fe LiNbO<sub>3</sub> crystal fiber with a 7-mm length and 0.7-mm diameter. The doping levels of Ce and Fe are  $\sim 300$  and 500 ppm, respectively. Two interesting features of this specially doped material are its high photosensitivity so that the photorefractive effect can be initiated with a low-power (5-mW) laser diode and that its spectral response covers all the visible spectral lines.<sup>6</sup>

In view of Fig. 1 we see that a reflection-type fiber specklegram can be constructed.<sup>7</sup> It is trivial that the reference beam can be reconstructed if one uses the same fiber speckle field. To introduce the transversal displacement on the sensing fiber, a cylindrical rod affixed with a piezoelectric driver, as illustrated in Fig. 1, is used as the bending device. The bending radius (i.e., the distance between bending points A and B) is  $\sim 2$  mm. The normalized correlation peak intensity as a function of transversal displacement is plotted in Fig. 2. From this figure we see that it exhibits a fairly linear relationship of 0- to 1.4- $\mu\text{m}$  transversal displacement, for which it can be used for submicrometer displacement sensing. The dynamic range of this fiber specklegram sensing system is  $\sim 1.3$   $\mu\text{m}$ , in which the sensitivity of measurement can be as high as 0.05  $\mu\text{m}$ . We stress that the sensitivity can be improved if higher-mode sensing fiber is used.

In conclusion, we have demonstrated a highly sensitive FSS using a multimode sensing fiber coupled with a PR fiber. The experiment shows that the sensitivity of the PR FSS (in terms of transversal displacement) can be of the order of 0.05  $\mu\text{m}$  or even higher if a higher-mode sensing fiber is used.

The authors are with The Pennsylvania State University, University Park, Pennsylvania 16802. F. T. S. Yu, S. Yin, and J. Zhang are with the Department of Electrical Engineering, and R. Guo is with the Material Research Laboratory.

Received 19 November 1993; revised manuscript received 8 April 1994.

0003-6935/94/225202-02\$06.00/0.

© 1994 Optical Society of America.

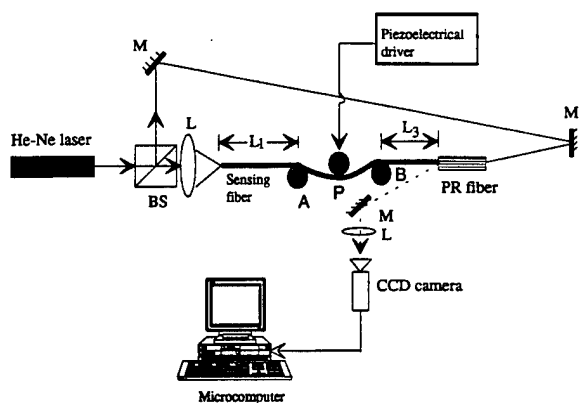


Fig. 1. Experimental setup of the PR FSS system. M, mirror; L, lens; BS, beam splitter;  $L_1$ ,  $L_3$ , fiber lengths; P, bending point.

Compared with the intensity FSS technique as reported in the previous paper,<sup>8</sup> the sensitivity of the PR FSS is  $\sim 1$  order higher. This high sensitivity is primarily due to the complex amplitude-field analysis compared with the intensity-field analysis of the system.<sup>8</sup>

In short, the proposed PR FSS offers the advantage of higher sensitivity, compact size, direct-coupling architecture, and more robustness during environmental changes. Because of the simplicity of the PR FSS system and its economical operation, we expect the proposed PR FSS to have widespread practical applications, such as in acoustic wave sensing and structure fatigue monitoring.

The authors acknowledge the support of the Advanced Research Projects Agency through the U.S. Army Research Office under contract DAAL 03-92-G-0328.

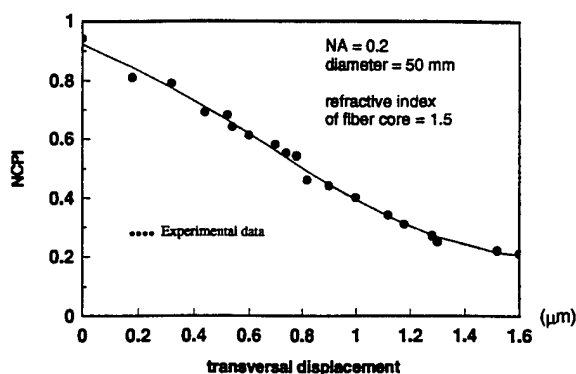


Fig. 2. Normalized correlation peak intensity (NCPI) value as a function of transversal displacement. NA, Numerical aperture.

## References

1. E. Udd, *Fiber Optic Sensors* (Wiley, New York, 1991), Chap. 1, p. 1.
2. S. Wu, S. Yin, and F. T. S. Yu, "Sensing with fiber specklegrams," *Appl. Opt.* **30**, 4468-4470 (1991).
3. S. Wu, S. Yin, S. Rajan, and F. T. S. Yu, "Multichannel sensing with fiber specklegrams," *Appl. Opt.* **31**, 5975-5983 (1992).
4. R. S. Feigelson, "Growth of fiber crystals," in *Crystal Growth of Electronic Materials*, E. Kaldis, ed. (North-Holland, Amsterdam, 1985), pp. 127-144.
5. J. K. Yamamoto and A. S. Bhalla, "Growth of  $\text{Sr}_{1-x}\text{Ba}_x\text{Nb}_2\text{O}_6$  single crystal fiber," *Mater. Res. Bull.* **24**, 761-765 (1989).
6. S. Yin and F. T. S. Yu, "Specially doped  $\text{LiNbO}_3$  crystal photon. Technol. Lett. **5**, 581-582 (1993).
7. F. T. S. Yu and S. Yin, "Holographic storage and interconnection using a Ce:Fe-doped  $\text{LiNbO}_3$  photorefractive crystal fiber with a tunable visible-light laser diode," *Opt. Memory Neural Networks* **1**, 289-301 (1992).
8. F. T. S. Yu, M. Wen, S. Yin, and C. Uang, "Submicrometer displacement sensing using inner-product multimode fiber speckle fields," *Appl. Opt.* **32**, 4685-4689 (1993).

**Appendix 8.**

**"Low Temperature Dielectric Relaxation Phenomena in Relaxor Ferroelectric Strontium Barium Niobate," *Fer2oelectrics* 158, 283-288 (1994).**

J.M. Pova  
R. Guo, and  
A.S. Bhalla

## LOW TEMPERATURE DIELECTRIC RELAXATION PHENOMENA IN RELAXOR FERROELECTRIC STRONTIUM BARIUM NIOBATE SINGLE CRYSTALS

J. M. Povoá<sup>#</sup>, R. Guo and A.S. Bhalla

*Materials Research Laboratory, The Pennsylvania State University, University  
Park, PA 16802 USA*

*(Received August 9, 1993)*

**Abstract** Low temperature (15–300K) dielectric permittivities of tungsten bronze  $\text{Sr}_{1-x}\text{Ba}_x\text{Nb}_2\text{O}_6$  (SBN(1-x)% , 1-x=0.50, 0.61, and 0.75) single crystals were studied using dielectric spectrum techniques. Two distinct dielectric relaxation features were observed in all three crystal compositions. The dielectric anomaly at temperature range  $\sim(150\text{K}-300\text{K})$  is presumably associated with the incommensurate (ICS) superlattice transformation identified by high resolution TEM (Bursill and Lin).<sup>1</sup> No experimental evidence of phase transition was found in the measurement regime for the dielectric anomaly observed at temperature below 150K. Dielectric properties of the poled crystals indicate that the ICS related dielectric anomaly is strongly dependent on the polarization-strain coupling along the c-direction, while the second low temperature relaxation is associated to the polarization fluctuation in the a-b plane related to the relaxor nature of the SBN solid solution system. The experimental results further substantiate the thermally agitated polarization perturbation model. It is suggested that the dielectric relaxation phenomenon of ferroelectric tungsten bronzes SBN at low temperatures underlines the deformed oxygen octahedral structure with the added characteristics of the freezing-in of the relaxor polarization fluctuations.

## INTRODUCTION

Temperature and frequency dependencies of dielectric permittivity of relaxor ferroelectrics near the ferroelectric-paraelectric phase transition have been studied exclusively as characteristics of relaxor ferroelectrics.<sup>2,3</sup> At any specific temperature, a relaxor may still preserve its macroscopic homogeneous chemical composition and crystalline symmetry, but local chemistry may deviate from the global and local symmetry may be lower than global symmetry, as a result of local polarization fluctuation.<sup>3</sup>

However, polarization mechanisms in ferroelectric tungsten bronze family is still comparatively lacking, particularly, the mechanisms of dielectric dispersion behavior with strong resemblance of relaxor-type phase transition at a temperature much lower than the ferroelectric phase transition region,<sup>4,5,6</sup> have not been thoroughly studied. At room temperature, SBN is uniaxial ferroelectric with the polar vectors parallel to the c-axis.

<sup>#</sup> permanent address: Department of Physics, Universidade Federal de São Carlos, São Carlos, SP Brazil.

There have been reports<sup>1</sup> on the ferroelastic distortions in SBN at temperature near 198K (in SBN50) resulting in the orthorhombic structure caused by incommensurate phases, similar as in the case of  $\text{Ba}_2\text{NaNb}_5\text{O}_{15}$  (BNN). Ferroelectric phase transition from tetragonal  $4mm$  to monoclinic  $m$  was reported<sup>6</sup> for several ferroelectric compositions of tungsten bronze structure, but lack of phase transition evidences such as pyroelectric anomaly in the polar direction (in PBN solid solution) argues against the suggested phase transition.<sup>5</sup>

This paper reports the temperature and frequency dependencies of dielectric properties of SBN single crystals in a temperature range from 15 to 300K. Understandings about the low temperature dielectric properties in tungsten bronze crystals are presented based on new experimental results in further substantiation to the relaxor fluctuation model.<sup>3,5</sup> More complete studies covering other tungsten bronze solid solution systems will be presented in publications elsewhere.<sup>7</sup>

## EXPERIMENTAL PROCEDURE

SBN50, SBN61, and SBN75 single crystal specimens used for this investigation were grown by a Czochralski pulling technique. Electrical and physical properties of those compositions have been reported both in the literature<sup>8,9</sup> and our earlier publication.<sup>10,11</sup> Single crystal specimens of optical quality were oriented in either perpendicular or in parallel to the c-axis (polarization axis) direction, cut, polished, and electroded with sputtered Au for dielectric measurements.

When poling is required, the samples were poled along the [001] direction by applying a DC electric field of 10kV/cm at  $T_c$  in oil bath for 15 minutes.

Complex dielectric constants were obtained from impedance and phase angles measured in discrete frequencies previously selected in a range from 5Hz to 13MHz and at temperatures in between 15K to 300K at approximate 5K intervals, using a RF impedance analyzer (HP4192A, Hewlett-Packard). Each of the measurement was performed at a constant temperature during cooling. The real and imaginary parts of the dielectric permittivity were calculated based on a parallel RC circuit model by using a separate computer program. A cryogenic refrigeration system (APD, Cryogenics Inc.) was utilized to obtain temperatures as low as 10K.<sup>5</sup>

## RESULTS AND DISCUSSION

Two distinct dielectric relaxation phenomena at low temperature (far below the main ferroelectric-paraelectric phase transition temperature) were observed in all three SBN compositions. A broad dielectric dispersion (with strong anomaly seen in  $\kappa_3''$ ) appeared at temperature immediately below the room temperature ( $\sim >150\text{K}$ ) and another dielectric dispersion (with strong anomaly seen in  $\kappa_1''$ ) was found at temperature lower than  $\sim 150\text{K}$ . A strong resemblance for both these dielectric relaxation behavior with the Debye-type relaxation is found, in that the maximum of dielectric  $\kappa''$  shifts to higher temperatures at higher frequencies. A typical behavior of such dielectric permittivity as function of temperature and frequencies is shown in Fig.1 for SBN61 c-axis crystal in entire

measurement temperature region. The two dispersive phenomena were named as  $\alpha$  (anomaly at  $T > 150\text{K}$ ) and  $\beta$  (anomaly at  $T < 150\text{K}$ ), respectively (that will be called in the text follows).

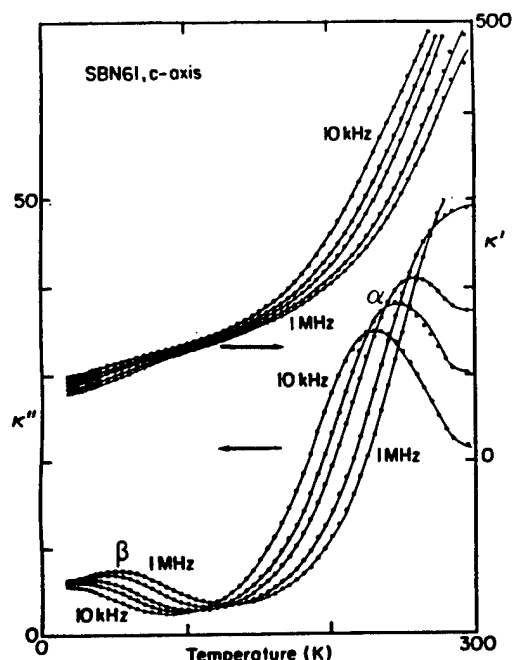


FIGURE 1.

Dielectric permittivities  $\kappa'_3$  and  $\kappa''_3$  of single crystal SBN61 as function of temperature and frequency. Two distinct dielectric anomalies are shown as  $\alpha$  and  $\beta$  respectively.

It is interesting to notice the difference in these two dielectric dispersions found in SBN. Only one broad dispersion anomaly was found in similar tungsten bronze ferroelectric crystals  $\text{Pb}_{1-x}\text{Ba}_x\text{Nb}_2\text{O}_6$  in either tetragonal or orthorhombic symmetry.<sup>5</sup> The anomaly  $\beta$  alone was reported<sup>6</sup> in SBN50 presumably because  $\alpha$  is weak in a prepoled a-axis crystals and was not noticed. Though seem to have similar Debye-type behavior, both  $\alpha$  and  $\beta$  anomalies are shown to be dependent on crystal orientations and compositions. For  $\alpha$  anomaly, the temperature at which the  $\kappa''$  is found to be maximum at a constant frequency,  $T\kappa''_{\max}$  follows the trend as:

$$\alpha\text{-anomaly: } T\kappa''_{\max}(\text{SBN75}) < T\kappa''_{\max}(\text{SBN61}) < T\kappa''_{\max}(\text{SBN50}),$$

while the  $T\kappa''_{\max}$  exhibited a reverse trend for the  $\beta$  anomaly as:

$$\beta\text{-anomaly: } T\kappa''_{\max}(\text{SBN75}) > T\kappa''_{\max}(\text{SBN61}) > T\kappa''_{\max}(\text{SBN50}).$$

The intensity of the  $\kappa''_{\max}$  displayed generally a increasing tendency as the Sr/Ba ratio increases for both the  $\alpha$  and  $\beta$  anomalies disregarding the orientation of the crystals:

$$\alpha \text{ or } \beta\text{-anomalies: } \kappa''_{\max}(\text{SBN75}) > \kappa''_{\max}(\text{SBN61}) > \kappa''_{\max}(\text{SBN50}).$$

Further experimental evidence showed clearly the dependence of the  $\alpha$  and  $\beta$  phenomena on the polarization and strain couplings. After poling at  $10\text{kV/cm}$ , the  $\alpha$  anomaly in c-directions in all three compositions became diminished, less frequency dependent, and the  $\kappa''_{\max}$  appeared at lower temperatures. At the same time, in fact, the  $\kappa''_{\max}$  in a-direction increased slightly and appeared to be more frequency dependent. However, the  $\beta$  anomaly had changes as slight increases in intensity of  $\kappa''_{\max}$  in both a-axis and the c-axis crystals, with the  $\kappa''_{\max}$  being more diffused (the peak moved to lower temperatures) in a-axis crystals and sharper in c-axis crystals (the peak moved to a higher temperature). Evident the  $\alpha$ -anomaly is eminent for the c-axis crystals while the  $\beta$ -

anomaly is prominent for the a-axis crystals. It is therefore possible to assign the  $\alpha$  and  $\beta$  anomalies to be associated with the structure elements parallel (for  $\alpha$ ) and perpendicular (for  $\beta$ ) to the uniaxial c-direction. As the intensity of the  $\kappa''_{max}$  is proportional to the increase in Sr/Ba ratio, it is also conceivable to suggest that both the phenomena are related to the A-site cation ordering in the solid solution system, or in other words, the relaxor nature of the solid solution system when the Sr/Ba ratio increases.

Some examples of the experimental results for the dielectric dispersion behavior in both a-, and c-axis directions, before and after the poling was performed, are shown in Fig. 2 (SBN61, c-axis), and Fig. 3 (SBN75, a-axis). Only the  $\beta$  anomaly is shown in these figures.

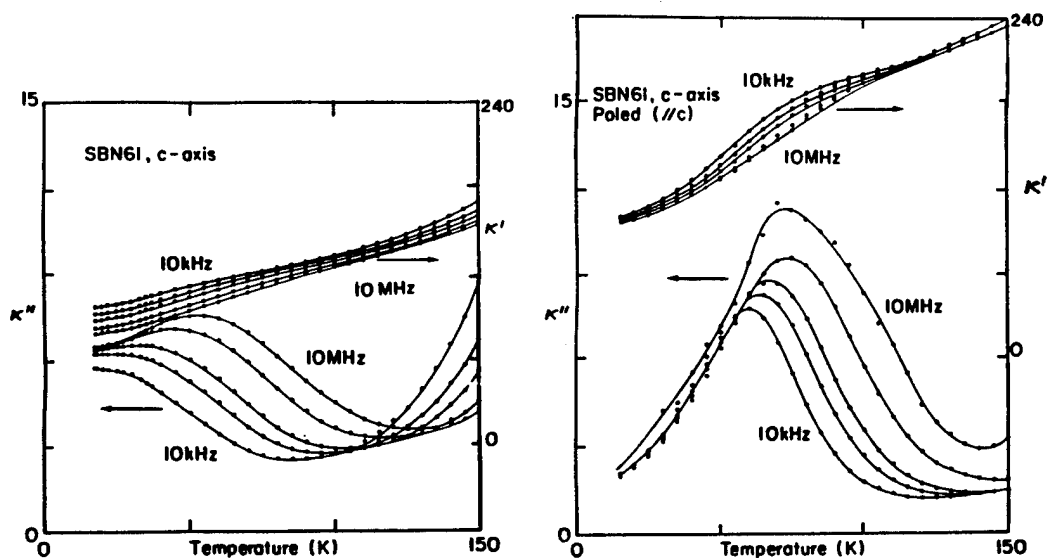


FIGURE 2. Dielectric permittivities  $\kappa'_3$  and  $\kappa''_3$  as function of temperature and frequency for SBN61: (a) before and (b) after poling.

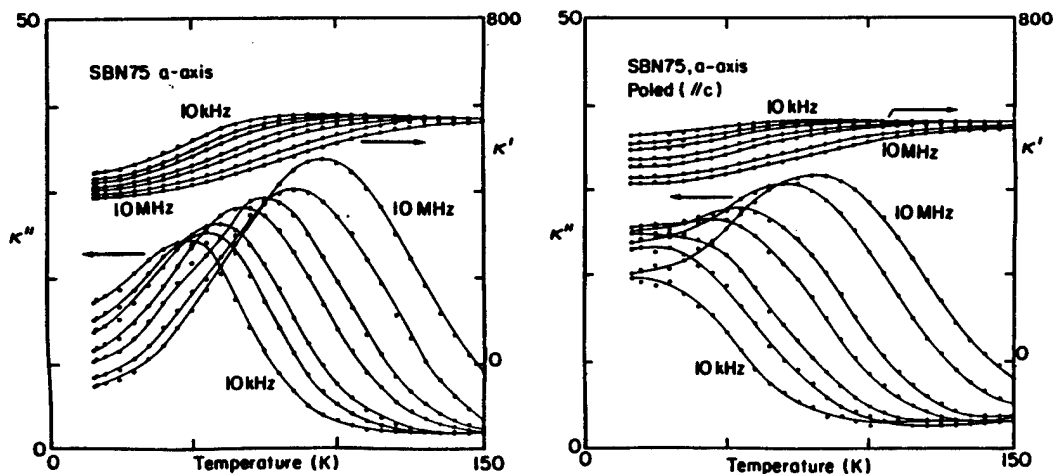


FIGURE 3. Dielectric permittivities  $\kappa'_1$  and  $\kappa''_1$  as function of temperature and frequency for SBN75: (a) before and (b) after poling.

The origin of these dielectric dispersion phenomena is discussed briefly in the followings:

**$\alpha$  anomaly:** We believe this dielectric anomaly is one of the experimental evidence corresponding to the earlier report of the incommensurate superlattice structure found in SBN50. Evidence for an incommensurate phase transition at  $\sim 198\text{K}$  in SBN50 crystal was reported by Bursill and Lin,<sup>1</sup> indicated by incommensurate superlattice (ICS) spacing along  $k_{110}$  detected by high resolution transmission electron microscopy. They also pointed out that those pseudotetragonal or orthorhombic distortion of the subcell parameters must be small due to the absence of any splitting for higher-order subcell (or supercell) reflections. Earlier report by Carruthers and Grasso's<sup>12</sup> shown that the SBN subcell is tetragonal for  $1-x \geq 0.5$  (e.g., in SBN61 and SBN75). No detailed TEM study of ICS structure on relaxor SBN61 or SBN75 is available to our knowledge. The crystallographic basis of this incommensurate superlattice comes from the modulation of the O-ions in the  $(0,0,z/2)$  plane that causes cell doubling in the c-direction and in turn giving rise to the tilting of the oxygen octahedra in the a-b plane therefore the orthorhombic superlattice. Similar incommensurate superstructure may also be possible in SBN61 and SBN75, however, the modulation would be very weak and therefore, identifying the weak symmetry elements developed in a disordered framework structure is considerably difficult. Poling along c-axis enhances the ferroelectric tetragonal phase and suppresses the orthorhombic distortion caused by the O-ion modulation. This explains the diminishing of the  $\kappa''$  dispersion in the c-axis in a poled sample. Similar dielectric dispersion ( $\alpha$  anomaly) absent in PBN family is probably due to the instability of the  $(\text{Pb,Ba})\text{Nb}_2\text{O}_6$  solutions. Orthorhombic phase is the energetically favored stable phase at the room temperature<sup>13</sup> for Pb:Ba ratio  $>0.63:0.37$  and a quasi-commensurate "lock-in" phase transition occurs within the paraelectric phase.<sup>14</sup> In SBN however, no lock-in phase transition has been reported so far.

**$\beta$  anomaly:** This dielectric dispersion behavior is presumably related to the polarization fluctuation "freezing-in" originated from the relaxor nature of SBN solid solution. A thermally agitated local polarization fluctuation model was proposed to explain the dispersion phenomena in PBN crystals<sup>5</sup> and the argument can be similarly applied in this case. The model is developed for the tungsten bronze crystallographic structure in which the deformed oxygen octahedra allow the local polarization to have components in both a-axis and c-axis. The local chemical inhomogeneity in SBN ferroelectric relaxors destroys global translational symmetry, and perturbs the direction of local polarization away from macroscopic symmetry direction on a nanoscale. Such perturbation is a thermally activated process and dynamic in nature. Thus, dielectric relaxation can be detected when thermal energy is comparable with potential barrier height of local polarization state. The origin of each relaxation phenomena is found related to a variety of A-site cations and is a function of its activation energy that could be estimated from the statistical size of the local region. Poling performed at a distant temperature than the characteristic freezing temperature will not significantly influence the relaxation behavior, however, the diminishing  $\alpha$  anomaly after poling made the  $\beta$  anomaly more distinguishable than before the poling.

The low temperature relaxation behavior is of characteristic of a dielectric spin glass in analogous to the behavior well known in magnetic spin glasses.<sup>15</sup> However, in tungsten

bronze ferroelectrics such as in SBN solid solution, the fluctuation component of the polarization can take place not only in the high temperature paraelectric phase, but also in the low temperature ferroelectric phase. It underlines that in general, tungsten bronze structure is more flexible to allow the coupling between the nano scale polar regions in either paraelectric matrix or ferroelectric matrix. It also implies that the anisotropy energy in ferroelectric tungsten bronzes are higher in comparison with that of magnetic systems as no genuine analogy of this type of spin glass behavior can be found in magnetic system.

## SUMMARY

Low temperature (15~300K) dielectric properties of the SBN ferroelectric single crystals were investigated and characterized to understand the strong "Debye-like" dielectric dispersion phenomena by using dielectric spectrum techniques.

Two significant dielectric relaxation phenomena were encountered for SBN single crystals in both a- and c-directions at low temperatures ( $15\text{K} < T < 300\text{K}$ ) and over a broad frequency range ( $10^2$ - $10^7\text{Hz}$ ). The  $\alpha$  anomaly has strong dependence to the polarization-strain coupling in the c-axis and the correlation to the incommensurate superlattice transformation is suggested. The  $\beta$  anomaly is characteristic of dielectric relaxation phenomena related to the polarization fluctuation "freezing-in" arising from the chemical inhomogeneity earlier reported in tungsten bronze PBN crystals.

More conclusive experiment evidence, such as low temperature HRTEM and quantitative pyroelectric measurement are required to support the preliminary understandings reported in this paper.

## ACKNOWLEDGMENT

J.M. Pova gratefully acknowledges the UFSCar and CNPq, Brazil, for permission and financial support to visit Materials Research Laboratory, The Pennsylvania State University. The authors express their appreciation to Dr. L.E. Cross for encouragement and stimulating discussions.

## REFERENCES

- <sup>1</sup>L.A. Bursill and Peng J. Lin, *Acta Cryst.*, **B43**, 49 (1987).
- <sup>2</sup>G.A. Smolenskii, *J. Phys. Soc. Japan*, **28**, Suppl., 26 (1970).
- <sup>3</sup>L.E. Cross, *Ferroelectrics*, **76**, 241 (1987).
- <sup>4</sup>S. G. Sankar, R. Guo, Z. P. Chang, A. S. Bhalla and L. E. Cross, 89th Annual Meeting Abstracts, p165 (American Ceramic Society, Westerville, 1987).
- <sup>5</sup>R. Guo, A.S. Bhalla, C.A. Randall, and L.E. Cross, *J. Appl. Phys.*, **67**, 6405 (1990).
- <sup>6</sup>Y. Xu, Z. Li, W. Li, and H. Wang, *Phys. Rev. B*, **40**, 11902 (1989).
- <sup>7</sup>R. Guo, J.M. Pova, and A.S. Bhalla (to be published).
- <sup>8</sup>e.g., A.M. Glass, *J. Appl. Phys.*, **40**, 4699 (1969).
- <sup>9</sup>R.R. Neurgaonkar, W.K. Cory, and J.R. Oliver, *Ferroelectrics*, **51**, 3 (1983).
- <sup>10</sup>R. Guo, A.S. Bhalla, G. Burns, and F.H. Dacol, *Ferroelectrics*, **93**, 397 (1989).
- <sup>11</sup>A.S. Bhalla, R. Guo, L.E. Cross, G. Burns, F.H. Dacol, and R.R. Neurgaonkar, *Phys. Rev. B*, **36**(4), 2030 (1987).
- <sup>12</sup>J.R. Carruthers and M. Grasso, *J. Electrochem. Soc.*, **117**(11), 1426 (1970).
- <sup>13</sup>R. Guo, A.S. Bhalla, C.A. Randall, Z.P. Zhang, and L.E. Cross, *J. Appl. Phys.*, **67**(3), 1453 (1990).
- <sup>14</sup>C.A. Randall, R. Guo, A.S. Bhalla, and L.E. Cross, *J. Mat. Res.*, **6**(8), 1720 (1991).
- <sup>15</sup>D. Viehland, S.J. Jang, L.E. Cross, and M. Wuttig, *J. Appl. Phys.*, **68**(6), 2916 (1990).